Project No. 10-963

Development of Barrier Layers for the Protection of Candidate Alloys in the VHTR

Reactor Concepts

Dr. Carlos G. Levi
University of California, Santa Barbara

In collaboration with:
University of Michigan

William Corwin, Federal POC
Dave Swank, Technical POC

NEUP Nuclear Energy University Programs
U.S. Department of Energy

NEUP FINAL REPORT PROJECT 10-963

Project Title: Development of Barrier Layers for the Protection of Candidate Alloys in the VHTR

Covering Period: October 1, 2010 through September 30, 2014 (One year NCE).

Date of Report: November 30, 2014

Recipient: Materials Department, College of Engineering
University of California, Santa Barbara, CA 93106-5050

Principal Investigator: Carlos G. Levi, 805-893-2381, levic@engineering.ucsb.edu

Collaborators: J. Wayne Jones, 734-764-7503, jonesjwa@umich.edu
Tresa M. Pollock, 805-893-3810, pollock@engineering.ucsb.edu
Gary S. Was, 734-763-4675, gsw@umich.edu

UCSB Personnel Dr. Elizabeth A. Clark (Graduate Student, Materials, now Ph.D.)
Connie Phung (Undergraduate Summer Intern, ME at Columbia)
James Yang (Project Specialist) – part time

UMich Personnel Alfred Okello (Graduate Student - MSE)
Gokce Gulsoy (Graduate Student – NERS) – Part time.

Project Objective.

The objective of this project was to develop concepts for barrier layers that enable leading candidate Ni alloys to meet the longer term operating temperature and durability requirements of the VHTR. The concepts were based on alpha alumina as a primary surface barrier, underlay by one or more chemically distinct alloy layers that would promote and sustain the formation of the protective scale. The surface layers must possess stable microstructures that provide resistance to oxidation, de-carburization and/or carburization, as well as durability against relevant forms of thermo-mechanical cycling. The system must also have a self-healing ability to allow endurance for long exposure times at temperatures up to 1000°C.

Barrier Layer Concepts.

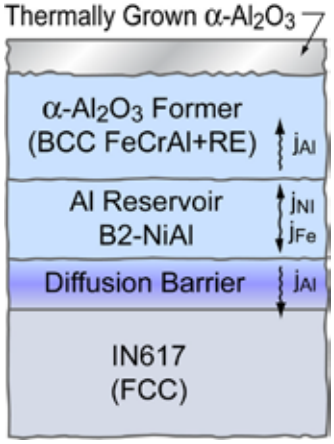

Two barrier layer concepts were explored. One relied on aluminizing as a path to form an Al reservoir on the alloy surface that can enable and sustain the formation of thermally grown alpha alumina. This approach had been claimed to increase resistance to carburization in alloy 617, but did not appear to have been extensively documented in the open literature. The second concept involved cladding the aluminized surface with a thin layer of FeCrAl(Y/RE), an alloy well known to form alpha alumina at lower temperatures much more readily than diffusion aluminide or MCrAlY coatings typically used for oxidation protection in Ni-base superalloys. (Cladding was used as a proof of concept approach. Similar architectures with tailored chemistries could be implemented by other techniques, e.g. ion plasma deposition.) Both concepts were implemented and studied during this project. A summary of accomplishments with details organized according to the tasks outlined in the original proposal, is given below.

Summary of Salient Findings

- This project demonstrated the viability of two barrier layer concepts for protection of alloy 617 at temperatures from 800°C to 1000°C in impure He. The key element of the protective barrier is a thin, dense alpha alumina scale that is stable in carburizing and decarburizing environments, superseding the natural chromia scale on 617.
- A desirably thin, dense and continuous alpha alumina layer was shown to form with minimal evolution of transient phases upon oxidation at 1000°C in flowing gettered Ar with $X_O<10^{-13}$. This initial condition was then used for all samples prepared for interdiffusion studies as well as for exposure to impure He, with or without load.
- Both barrier layer concepts rely on an aluminum reservoir based on NiAl, generated by aluminizing the 617 surface through a high activity process at temperatures in the range of 700-850°C. In one concept the NiAl layer is subsequently clad by diffusion bonding with a 100μm layer of FeCrAlY, which is a more favorable alpha alumina former than the B2-NiAl.
- The NiAl layer is kinetically stabilized against interdiffusion with the substrate owing to the *in-situ* formation of a double layer of $M_{23}C_6$ carbide and sigma phase between the aluminized layer and the substrate. These layers are interpenetrated by metal, which allows limited interdiffusion but toughens the brittle phases hindering propagation of delamination cracks.
- The $M_{23}C_6$+sigma layers evolve over time to a less continuous mixture of $M_{23}C_6$+M_6C carbides, arguably less effective against interdiffusion. The evolution over 500 h is negligible at 800°C but substantial at 1000°C, especially for layers aluminized at 700°C which concurrently transform to a mixture of B2-NiAl + $L1_2$-Ni_3Al. Layers formed at 850°C were much more stable, retaining the sigma phase and showing no evolution of $L1_2$.
- Cladding promotes de-stabilization, presumably by the inward flux of Fe which replaces Mo in the sigma phase. Concomitantly, the outward flow of Ni into the FeCrAlY layer first induces formation of nanoscale coherent B2 precipitates into the A2 matrix, and eventually its transformation to A1, but also reduces the tendency to form $L1_2$ in the aluminized layer.
- The conversion of A2/B2 into A1 over time was detrimental to the performance in impure He in aluminized+clad samples. The A1 regions showed preference for chromia formation instead of alumina, which is less desirable for resisting carburization and decarburization. The problem, however, was not evident in the specimens subjected to creep in impure He.
- The coupling of stress and environment during creep of uncoated 617 showed that, in general, mechanical loading increases the extent of surface degradation. The effect of stress, however, will depend on the parameters of the test: strain rate, loading type (static or cyclic), helium composition, and duration of the test.
- The barrier layer concepts investigated aid in protecting the underlying 617 by providing a more efficient environmental barrier (alumina) in helium environments. While NiAl does not form alumina as readily compared with FeCrAlY, the former is more mechanically robust at extremely high strains (16%) and seems to be able to resists the initiation and propagation of cracking in the event of an accidental breach. However, the presence of cladding in aluminized 617 affects the mechanical behavior of NiAl layer. Further research to understand the effect of interdiffusion between FeCrAlY and 617, and the role played by α-Cr precipitates in the mechanical behavior of the coating systems is underway.

Task 1. Synthesis of Barrier Layers.

The objective of this task was to develop and optimize the processing routes to generate the desired barrier layer configurations on alloy 617. Three generations of coatings were produced, based primarily on different aluminizing procedures as described later. Two types of specimens were produced for each generation. One type consisted of small (~11x5x1 mm) coupons for basic microstructural studies after oxidation and interdiffusion (Task 2) as well as exposure to impure He (Task 3). The second type comprised specimens for creep testing (Task 4), with the geometry illustrated in Figure 1.1. Both aluminized alone as well as aluminized + clad specimens were produced for Gens I and II. Based on the ensuing creep studies and other factors, to be discussed later, the Gen III specimens for creep were produced only in the aluminized form, with no cladding.

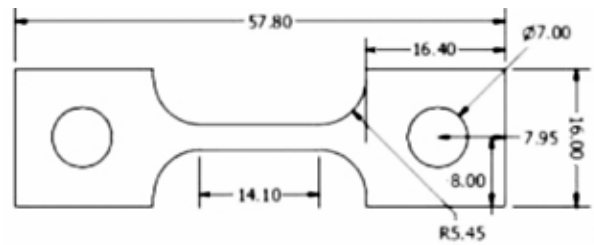

Figure 1.1. Geometry of the specimens used for creep testing. Dimensions in millimeters. The specimens were produced at UCSB and provided to University of Michigan for creep testing in flowing impure He.

1.1 Materials

The alloy 617 base material was kindly provided by INL from a well-characterized lot of rolled slab (Heat #314626, Lot #103374422, ThyssenKrupp VDM) with the composition given in Table 1.1. Alloy coupons were polished to 3μm diamond finish and ultrasonically cleaned prior to processing. Targets for electron beam physical vapor deposition (EB-PVD) used in the Gen III specimens were arc melted from pellets: Mo (Lot #B26B16, 99.7% purity, Johnson Matthey Electronics, Ward Hill, MA), Ta (Lot #X10189, 99.9% purity, Cerac, Inc., Milwaukee, WI), and Ni (Lot # F01H, 99.9% purity, Johnson Matthey, Danvers, MA). Materials for aluminizing included aluminum powder (<44 μm, 99.5%, Alfa Aesar, Ward Hill, MA) as the source, alumina powder (500 grit, Norton Co, Worcester, MA) as the filler, and $CrCl_3 \bullet 6H_2O$ (reagent grade, Alfa Aesar, Ward Hill, MA) as the activator. The FeCrAlY for cladding, with typical composition given in Table 1.1, was procured in the form of 50 and 100 μm foil (Goodfellow, Oakland, PA).

Table 1.1 Nominal composition of the Alloy 617 and FeCrAlY foil (at.%).

	Ni	Co	Cr	Mo	Fe	Al	C	Mn	Si	Ti	Cu	Other
617	Bal.	11.4	24.5	5.2	1.7	2.4	0.24	0.11	0.21	0.48	0.04	<0.004S, <0.005B
FeCrAl	-	-	22.0	-	Fe	9.7	0.09	0.19	0.56	-	-	0.06Y, 0.06Zr

1.2 Aluminizing

Aluminizing was performed by pack cementation in a high-activity/low temperature mode using a powder mixture of $4Al/4(CrCl_3 \cdot 6H_2O)/ 92Al_2O_3$ (in weight percent). The coupons and creep bars were wrapped in alumina paper and embedded in the pack, which was subsequently sealed in an alumina crucible and placed in a tube furnace under flowing high purity Ar ($X_O \leq 10^{-5}$). The pack was heated for a prescribed temperature (700-850°C) and time (4-10 h), depending on the desired aluminizing thickness (see below). After aluminizing the specimens were annealed at 1000°C in flowing, gettered Ar (with a measured oxygen content of $X_O \leq 10^{-13}$) to fully develop the structure of the surface layers. Any scale evolving during this process was removed and the

surface was polished down to an 800-grit finish to eliminate residual oxide. Three generations of materials with different aluminized layers were prepared, namely:

- Gen I: Aluminizing was performed at 700°C for approximately 9.6h and subsequently heat treated for 16 h to develop the NiAl layer by interdiffusion with the substrate. The process led to an interlayer of carbide + sigma phase that appeared to stabilize the coating against long-term interdiffusion. The process yielded a relatively thin modified surface layer that was less than optimal because (i) the carbide+sigma putative diffusion barrier seemed to evolve over time to a less desirable configuration, and (ii) it was susceptible to significant removal during the subsequent cleaning and polishing steps.
- Gen II: The primary goal was to increase the thickness of the surface modified layer, which was accomplished by increasing the aluminizing temperature to 850°C and reducing the time to 4h, as well as the shortening the subsequent treatment to develop the NiAl layer to 1 h. The changes had the advantage of minimizing the scale that had to be removed after heat treatment, preserving a thicker aluminized layer, and also were found to develop a more stable sigma phase. This became the preferred aluminizing process.
- Gen III: The concept behind Gen III was to improve on the stability of the sigma diffusion barrier as needed to further extend the durability of the system. The approach involved coating with a thin layer of a sigma stabilizer (Cr, Fe, W, Mo, Ta) prior to aluminizing. The substrates were heated to 800°C during EB-PVD. Because it is intended to minimize the withdrawal of Ni from the substrate a layer of EBPVD Ni was deposited on top of the sigma stabilizer to feed the formation of NiAl during the post-aluminizing heat treatment. The substrate temperature during Ni deposition was 650°C. Details on the specific dimensions of the EB-PVD layers were provided in the last quarterly report. After these coating steps the aluminizing was performed using the protocol develop for the Gen II specimens.

1.3 Cladding

A subset of aluminized specimens was clad with 100 µm FeCrAlY foil by diffusion bonding using a high vacuum hot press at 1000°C for 1 h under a pressure of 20 MPa. (Samples aluminized at 850°C were not heat treated prior to cladding because the structure of the surface layers was closer to the desired configuration owing to the higher processing temperature.) Both aluminized alloy and FeCrAlY foil surfaces were polished and cleaned prior to bonding.

Creep specimens were clad only on the wider surfaces of the gauge length. Because of the experimental setup the cladding had to extend beyond the limits of the test bar, and the excess had to be removed. Earlier experiences with coupons revealed that the cladding could be susceptible to damage if removed by mechanical trimming, so this operation was performed using a femtosecond laser developed by PI Pollock at UCSB.

1.4 Preoxidation

All coupons and creep specimens to be used for subsequent environmental exposures, with or without load, were pre-oxidized at 1000°C for 2 h in gettered Ar ($X_O \leq 10^{-13}$) to form a thin, continuous alpha alumina scale prior to testing. The surfaces were first polished to 800 grit finish. The presence of alpha alumina was confirmed using photostimulated luminescence spectroscopy (PSLS).

Task 2. Baseline Oxidation/Interdiffusion.

This task focuses on evaluating the microstructure evolution of the synthesized barrier layers in benign environments without applied load to establish a baseline for subsequent assessment of their behavior under stress in impure He. The surface of alloy 617 is modified to provide an Al reservoir that can create and maintain an adherent alpha alumina scale sufficiently robust to protect the alloy from attack by oxidizing, decarburizing or carburizing He environments. Conceptually the scale can be generated on the modified surface before exposure to the deleterious environments, and this is the approach taken in this investigation. The long term effectiveness of the barrier layer concepts is thus dependent on (i) the stability of the Al reservoir against depletion by subsequent oxidation and interdiffusion with the 617 substrate, as well as (ii) the ability of the system to regenerate the protective scale in case of cracking or spallation.

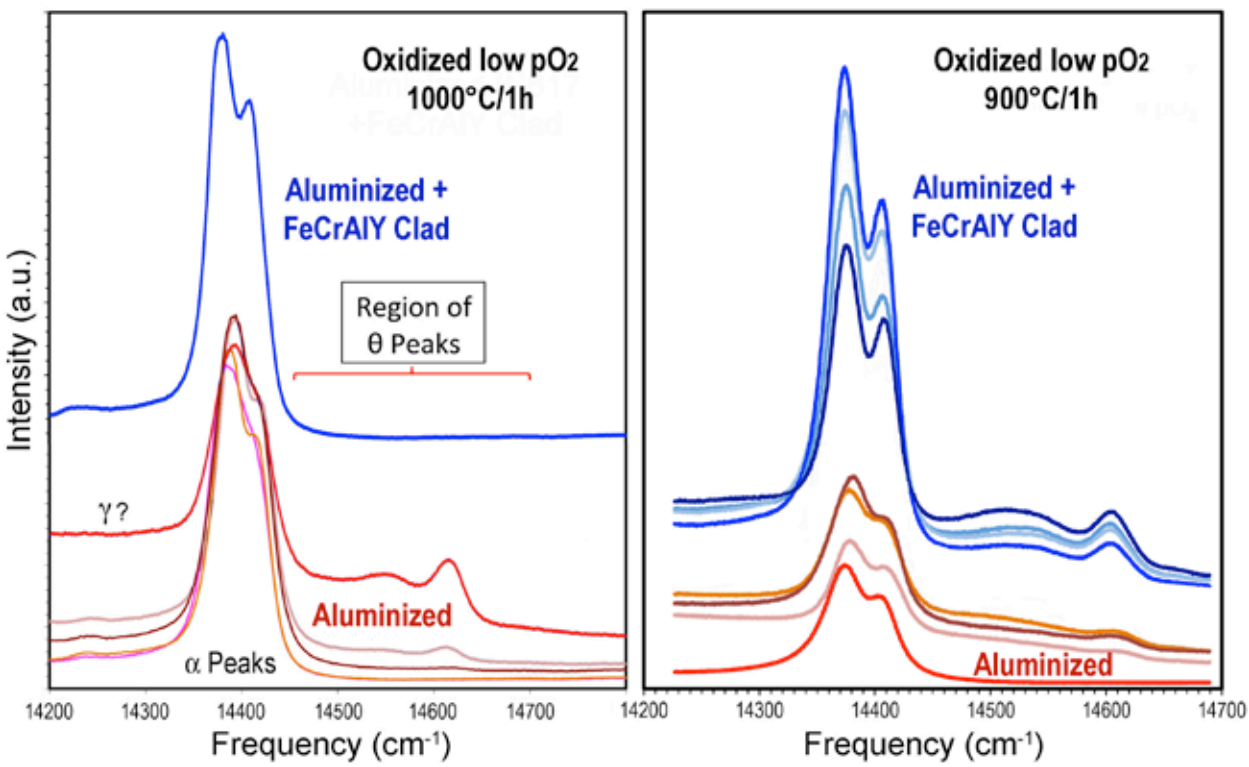

Figure 2.1 - Photostimulated luminescence peaks for alumina formed on the surfaces of aluminized 617 with and without FeCrAlY cladding, after 1h oxidation in low pO_2 at 1000°C and 900°C.

2.1 <u>Oxidation</u>

It was shown in earlier work that 1000°C pre-oxidation of both barrier layer architectures in low pO_2 (gettered Ar, $X_O \approx 10^{-13}$), led to the formation of a thin, dense and adherent α-alumina scale with no evidence of other oxides or significant growth of metastable alumina phases typical of pre-oxidation in air. The outcome is a much smoother scale because of the suppression of the plate-like or whisker-like morphologies associated with the transient alumina growth, less prone to disruption by the high velocity gas stream. It was also shown, however, that the transient alumina phases persisted for longer times in the aluminized surfaces than on those clad with FeCrAlY, and that difference is accentuated at lower temperatures, as shown in Figure 2.1. The corresponding surface scales are depicted in Figure 2.2.

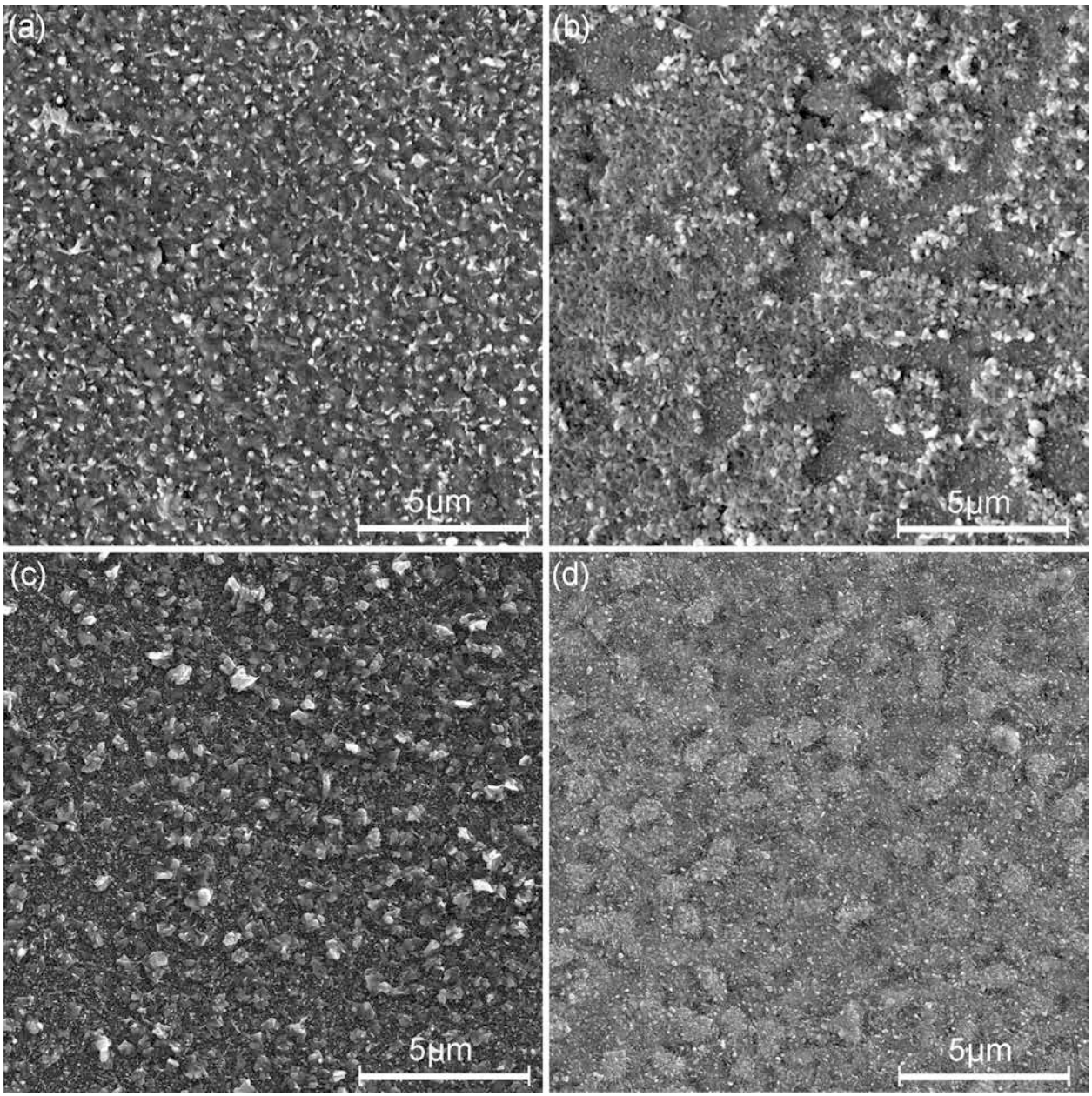

Figure 2.2 – Microstructures of surface scales for (a,c) FeCrAlY and (b,d) Aluminized 617, after 1h oxidation in low pO_2 at (a,b) 1000°C and (c,d) 900°C. All scales contain alpha alumina but there are transient alumina phases in (b-d), as shown in Figure 2.1.

The key outcomes of this exercise were (i) the identification of the necessary pre-oxidation conditions to minimize any transient alumina phases or other oxides, namely 2h at 1000°C in gettered Ar, and (ii) the demonstration that the alumina formed on both barrier layer concepts was sufficiently adherent and durable to avoid any disruptions that might influence the results of the subsequent tests in impure He. A remaining issue was whether a protective alumina scale could be regenerated if local damaged, e.g. cracking or spallation, ensued in impure He. That issue is addressed in Task 3.

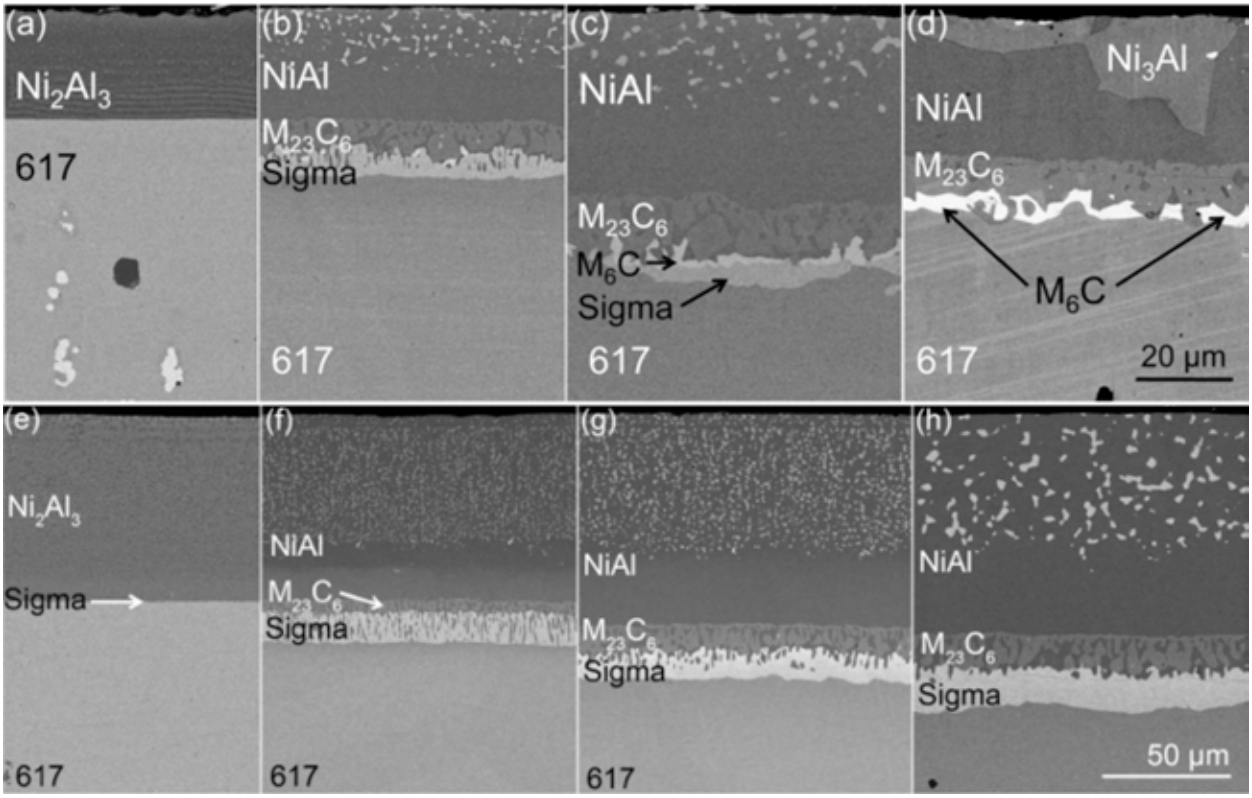

Figure 2.3 - Microstructures of the Gen-I and Gen-II modified surface layers on 617, produced by aluminizing at 700°C (a) and 850°C (e), respectively. In both cases the bulk of the aluminized layer is Ni_2Al_3; an incipient sigma layer is found to form during the higher temperature process but not at the lower temperature. The evolution of the microstructure upon subsequent heat treatment at 1000°C and (b,f) 16h, (c,g) 100h and (d,h) 500h, is shown on the corresponding row of images for each variant of the process. The continuous sigma layer that develops initially after aluminizing at 700°C in (a) evolves to a discontinuous M_6C layer after 500h (d), but is retained at 500h when the original coating is deposited at 850°C. The NiAl layer in the latter is also richer in Al (graded from the surface to the interface) as shown by the presence of Ni_3Al after 500h in (d) but not in (h).

2.2. Interdiffusion – Aluminized Systems

Considering the life requirements of the components protected by the barrier layers a crucial issue is the long-term diffusional stability of the barrier layers in contact with the substrate. In all cases the low-temperature, high-activity aluminizing yields a top layer comprising primarily Ni_2Al_3 (confirmed by XRD) with discrete second phases darker in BSE contrast, Figure 2.3(a,e). Figure 2.4(a) shows an Al:Ni ratio higher than 3:2, presumably because of substitution of other elements, e.g. Co, in the Ni_2Al_3. The darker low-Z phases in Figures 2.3(a,e) and 2.4(a) are likely carbides of the elements with lower solubility in Ni_2Al_3 that precipitate in situ as the aluminizing front advances rapidly into the 617 substrate. (Because these phases are transient and evolve into Cr-rich precipitates after short heat treatments, e.g. Figure 2.4(b), they were not analyzed further.) No layers of intermediate phases are distinguishable at the interface with the substrate after the lower temperature aluminizing (Gen I), Figure 2.3(a) but an incipient layer of sigma phase, corresponding to the spike in the Mo and Cr concentrations in Figure 2.4(a), is found at the similar interface after the higher temperature process (Gen II). This layer is interpenetrated by metal that eventually allows outward Ni diffusion to convert the Ni_2Al_3 layer into NiAl.

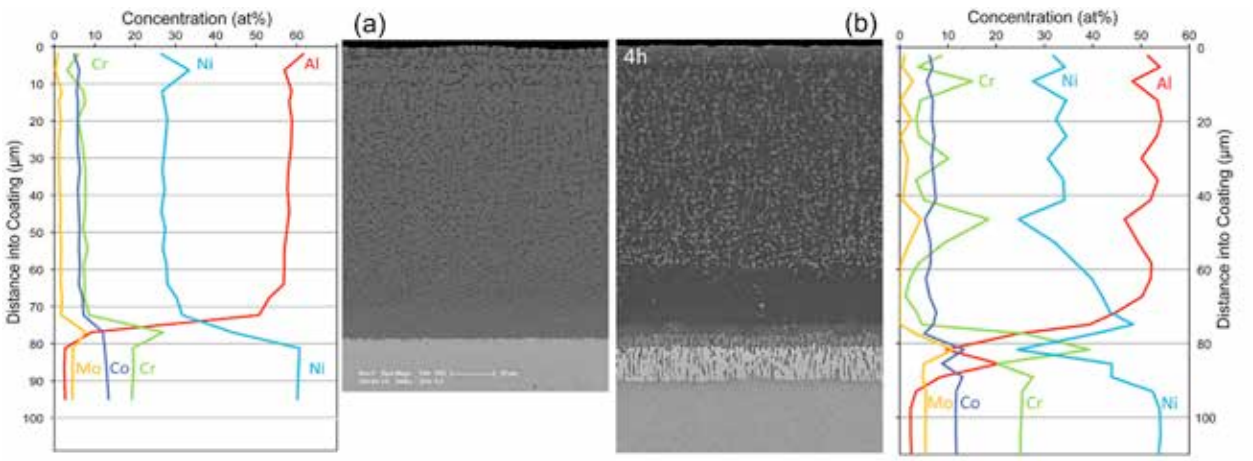

Figure 2.4 - EDX line scans and microstructures of the surface modified layer taken on Gen II samples (a) as-aluminized and (b) after 4h/1000°C heat treatment. Ni upward diffusion transforms the original Ni_2Al_3 layer to NiAl, but it slows down as the carbide+sigma phase diffusion barrier develops *in-situ*.

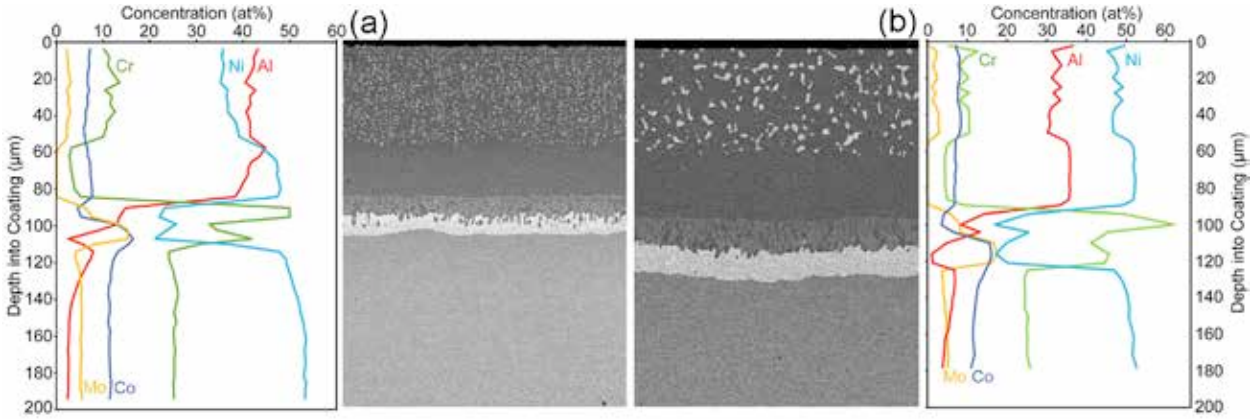

Figure 2.5 - EDX line scans and microstructures of the near surface layers from Gen II samples heat-treated at 1000°C for (a) 100h and (b) 500h. The carbide, sigma phase and the precipitate-free NiAl increase over time. The bulk of the NiAl layer is still B2 even after 500h.

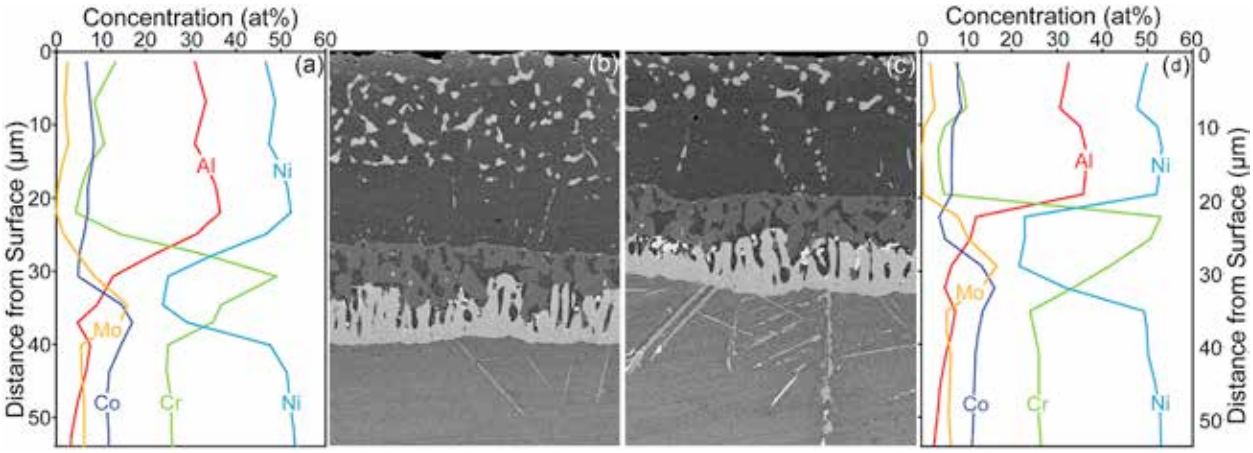

Figure 2.6 - EDS line scans (a,d) microstructural regions (b,c) from which they were acquired after (a,b) 100h and (c,d) 500h at 800°C. Note that the concentration profiles are not significantly changed over time, although minor changes are observed in the microstructures, especially the increase in precipitation within the substrate next to the modified layer at the longer times. The differences in thickness of the aluminized layer are associated with the surface polishing process after aluminizing.

As the aluminized surfaces are heat treated to transform the Ni_2Al_3 layer into a more desirable NiAl, two distinct layers develop at the interface with the substrate. These layers consist primarily of $M_{23}C_6$ carbide, closer to the NiAl, and sigma phase, closer to the substrate. They act as effective barriers to slow down interdiffusion with the substrate at longer times, in spite of their being interpenetrated by a small fraction of metallic phases. The metal inclusions have also been shown to inhibit crack propagation upon indentation of the brittle carbide and sigma layers and creep tests in Task 4 show no evidence of damage initiated within them, suggesting that their role as diffusion barriers may not be significantly detrimental to the mechanical integrity of the system. It is also noted that a layer of Ni-rich NiAl, devoid of second phases, evolves between the original aluminized thickness marked by Cr-rich precipitates, and the *in-situ* diffusion barriers, as shown in Figure 2.4(b). This layer has a noticeably lower Cr content than the outer NiAl layer, as shown in Figure 2.5. Note in Figure 2.7(a) that the addition of Al to the original 617 composition, denoted by a blue circle in the field A1+M_6C, moves the system into regions where A1 (FCC) and B2-NiAl can be in equilibrium with the $M_{23}C_6$ and sigma phases.

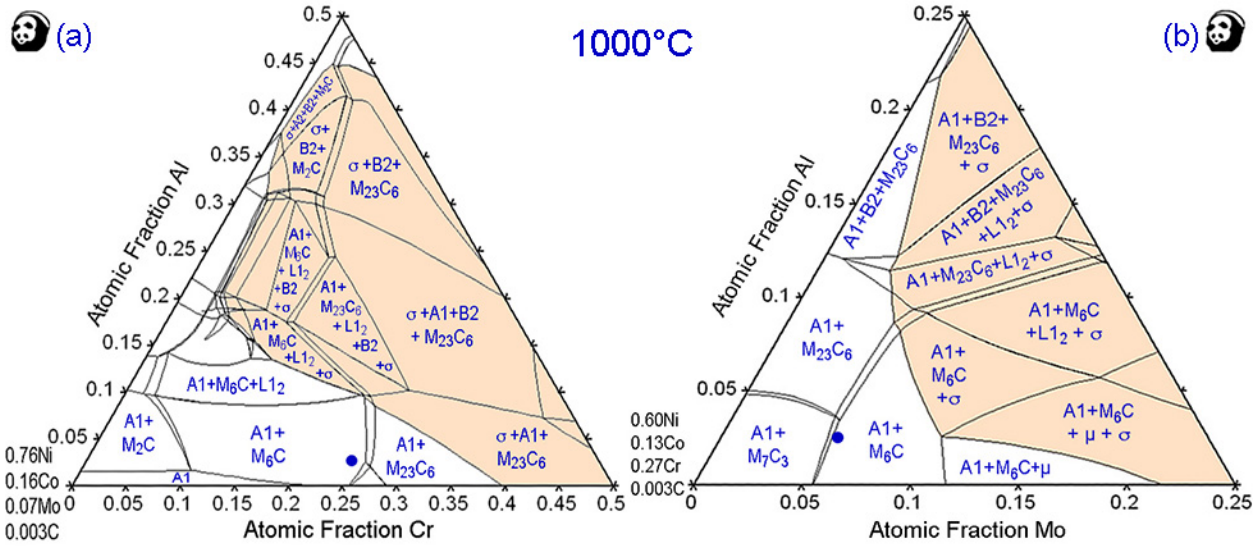

Figure 2.7 – Phase equilibria for a simplified version of Alloy 617 with (a) Ni, Co, Mo and C in the right proportions, and varying Al and Cr, or (b) Ni, Co, Cr and C as a base and varying Al and Mo. The circles represent the composition of 617 in each diagram, and the shaded area the fields containing the sigma phase, usually in combination with carbides and other metallic phases. Note that the scale on (b) is enlarged by a factor of two relative to that in (a). (Calculations using the CompuTherm PanNi8 database.)

Upon additional heat treatment at 1000°C the carbide and sigma interphases grow, albeit slowly, as shown in Figures 2.3 and 2.5. For the low temperature aluminizing in Figure 2.3(a-d), which led to a thinner NiAl layer (Gen I), the sigma layer becomes de-stabilized after ~100h and is replaced by a less continuous layer of M_6C that would be arguably less effective as a diffusion barrier. Concurrently, small amounts of the $L1_2$ phase are found in the region of the substrate close to the carbide layers, as suggested by Figure 2.7(a). In contrast, the Gen II specimens aluminized at the higher temperature show a much more stable sigma layer over time, retained even after 500h at 1000°C as shown in Figures 2.3(e-h) and 2.5(a,b).

The evolution of the modified surface layers in 617 is substantially slower at 800°C, as shown by comparisons of Figures 2.5 and 2.6. This is apparently the current temperature of interest for the IHX in the VHTR and that at which most of the creep tests (Task 4) were performed.

While the interdiffusion behavior for Gen II aluminized specimens has not been characterized beyond 500h, this investigation has shown that aluminizing at the temperature-time combinations that may produce a stable diffusion barrier is a viable and effective approach. An effort was then undertaken to explore avenues of further optimize this approach by alloying that could contribute to stabilize and increase the efficiency of the diffusion barrier layers, notably that based on the sigma phase. Modifying the composition of the bulk alloy was not considered an option because of the already extensive property database on 617 for the VHTR. Therefore, a surface modification approach was proposed wherein the substrate surface would be locally alloyed with a sigma stabilizer prior to aluminizing. Because the development of the aluminized layer requires drawing Ni from the substrate and the enhanced diffusion barrier would hinder that process, it is necessary to provide a Ni source above the surface enriched with the sigma stabilizer. The kinetics of aluminizing need to be reassessed in this new scenario. The baseline case is shown in Figure 2.8(a-c), where (a) corresponds to the aluminized condition at 850°C and (b,c) to the evolution of the aluminized layer after heat treatment at 1000°C for 1h and 16h, respectively. The role of Ni diffusion from the substrate is clearly evident by comparing this series with that in Figure 2.3(e,f). Because Ni upward diffusion from the substrate is largely suppressed in Figure 2.8(c) there is no significant interlayer formation at the interface with the substrate, in contrast with the more typical interdiffusion situation in Figure 2.3(f).

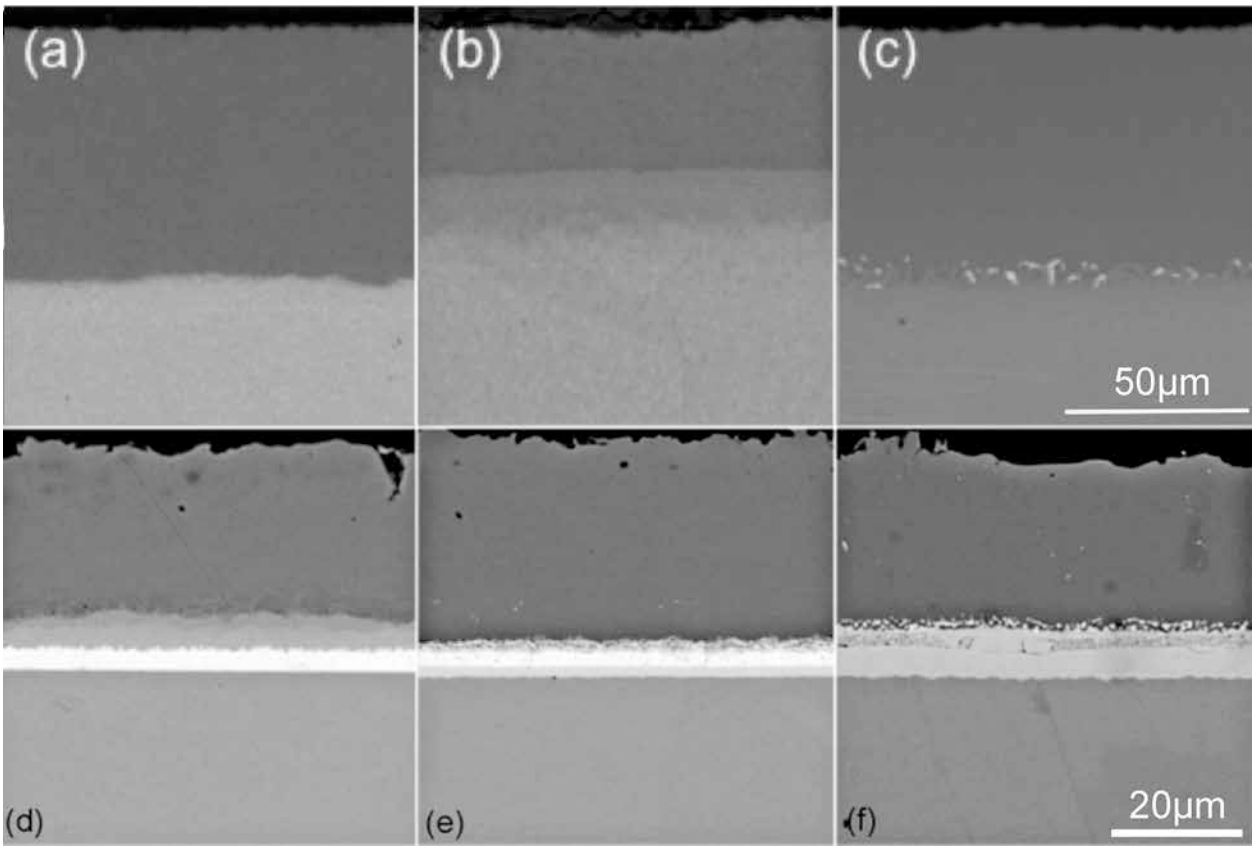

Figure 2.8 - SEM images of (a-c) 617 coated with Ni prior to aluminizing and (d-f) 617 coated with Mo and Ni prior to aluminizing. (a,d) Correspond to the as-aluminized condition, while the rest were heat treated at 1000°C for (b,e) 1 h and (c,f) 16 h. Note the evolution of the sigma phase in the second case, but not in the first.

A number of sigma stabilizers were identified and explored in this task, including some already included in the alloy (Cr, Mo, Fe) and others predicted to have a similar effect based on understanding of phase equilibria. Initial attempts with Cr and Cr+Fe were unsuccessful because the additions dissolved into the substrate and the Ni overlayer rather than remain localized at the interface. Experiments with Mo, W and Ta were more successful in avoiding excessive diffusion of the sigma stabilizer, but only Mo was deemed adequate within the limited number of experiments performed. An example of the Mo doped surface after aluminizing and heat treatment is shown in Figure 2.8(d-f). Note the substantially different appearance of the sigma layer, which appears much denser relative to those in Figures 2.3-2.6. A possible implication is that the absence of significant incorporated metal, which enabled the upward diffusion of Ni, may end up compromising the adherence of the environmental barrier layers.

The thermodynamic foundation for the difference in behavior between the Cr and Mo layers is illustrated in the calculated 1000°C isothermal sections of Figure 2.7. Alloy 617 is modeled as consisting of only Ni+Cr+Co+Mo+Al+C. The composition on the bottom left corner is that of alloy 617 after subtracting the elements plotted along the axes and normalizing the rest to 100 atomic percent. The blue circle represents the overall composition of alloy 617 (simplified) on the isothermal section, which is predicted to contain only the f.c.c. matrix (A1) and carbides. The shaded fields are those containing the sigma phase as part of the equilibrium. It is evident that smaller additions of Mo are required to move the system into the region of sigma stability than those of Cr. (Note the scale of the diagram for Mo is enlarged by a factor of two.) The predominant carbide in Figure 2.7(a) is $M_{23}C_6$ whereas that in Figure 2.7(b) is M_6C. The inference is that locally increasing the Mo content of the alloy 617 surface may be a more effective approach to stabilize the desired sigma + carbide *in-situ* diffusion barrier. Further work, however, is needed to optimize the conditions leading to the desirable architecture.

2.2. Interdiffusion – Aluminized +Clad Systems

Cladding of the aluminized surface generates an interesting combination of an Al-lean outer layer more favorable to the rapid formation of alpha alumina, with an Al-rich reservoir under it. The latter is expected to replenish the Al in the FeCrAlY layer as it is slowly consumed by oxidation. It also serves as a nominal diffusion barrier between FeCrAlY and 617, which was found earlier to occur rapidly at the temperatures of interest. A primary issue is the diffusional interactions of the cladding/reservoir system and their implications for its long-term durability.

Figure 2.9 shows microstructures of Gen I and Gen II aluminized systems with FeCrAlY cladding applied by diffusion bonding. The cladding was successfully performed in both cases, although the Gen II specimens showed residual porosity at the interface between the FeCrAlY and the $NiAl_X$, Figure 2.9(e). It is not clear whether this porosity is a result of asymmetric interdiffusion or insufficient creep deformation during bonding. It is worth noting, however, that the Gen I specimens were heat treated for 16h at 1000°C to develop the aluminized layer structure prior to cladding, whereas the Gen II specimens were clad in the as-aluminized condition because the sigma layer was already present. The outer surface is Ni-rich NiAl in Gen I and Ni_2Al_3 evolving into Al-rich NiAl during the process, as suggested by the presence of Cr-rich precipitates in Figure 2.9(e). One may hypothesize that the chemical differences may result in variations in the interdiffusion and creep behavior occurring during the diffusion bonding process, leading to porosity in Gen II but not in Gen I. The pores are eliminated by subsequent diffusion at 1000°C (Figure 2.9f-h) and much more slowly at 800°C (Fig. 2.10).

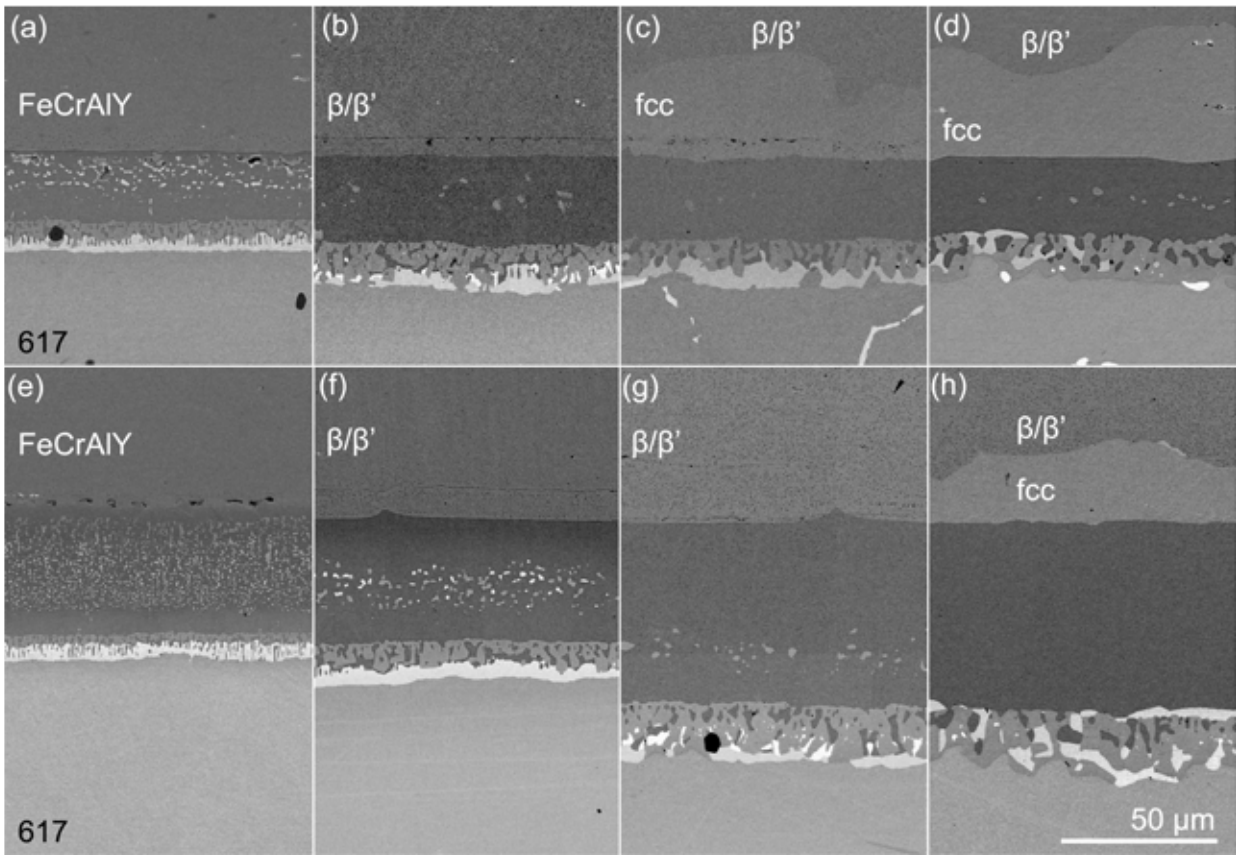

Figure 2.9 - SEM images of clad + aluminized 617 Gen I (a-d) and Gen II (e-h) samples in the as-clad (a,e) and after 1000°C heat treatment for 24 h (b,f), 168 h (c,g), and 500 h (d,h).

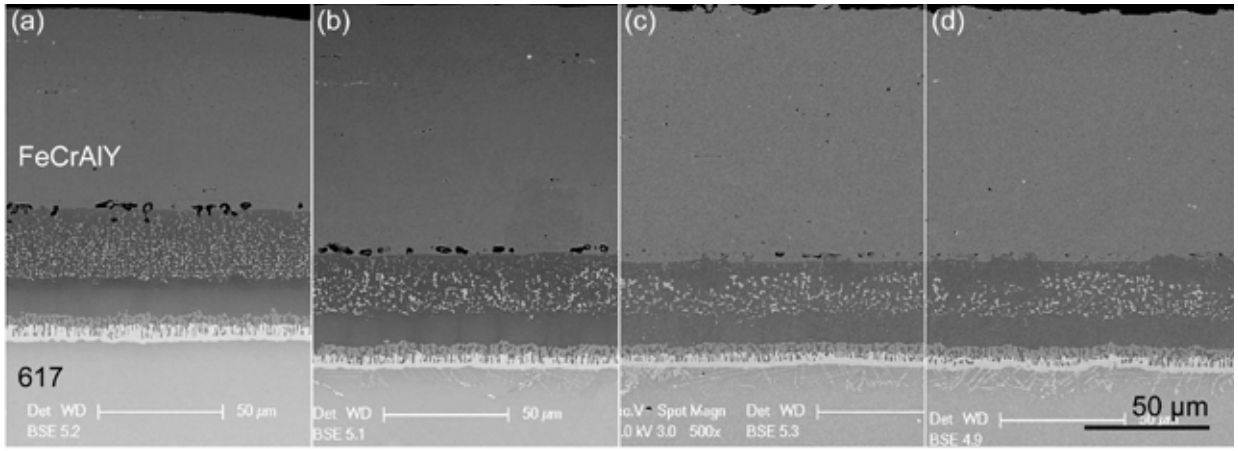

Figure 2.10 - SEM images of Gen II clad + aluminized 617 (a) after 1000°C/2h pre-oxidation treatment and after 800°C exposure for (b) 100h, (c) 225h, and (d) 375h.

Comparison of Figures 2.3 and 2.9 reveals that the carbide+sigma diffusion barrier layers are generally less stable in the presence of the cladding than for the un-clad aluminized layers. In general, the sigma layer is disrupted and largely eliminated when the cladding is present although it is slightly more durable in the Gen II specimens. Note in Figure 2.9(b,f) that the sigma layer is still continuous after 24h at 1000°C in the Gen II specimen, but is discontinuous for the Gen I materials. Figure 2.11 compares the evolution of the sigma layer composition in Gen I

aluminized+clad specimens at 1000°C after 16h and 168h. The inward diffusion of Fe from the cladding modifies the composition of the sigma layer reducing the content of Mo, Ni and Co, presumably reducing the stability of the sigma layer since Mo is a stronger stabilizer for sigma than Fe. The released Mo would then favor the formation of M_6C, not seen in this particular micrograph but evident after 24h, as shown in Figure 2.9(b).

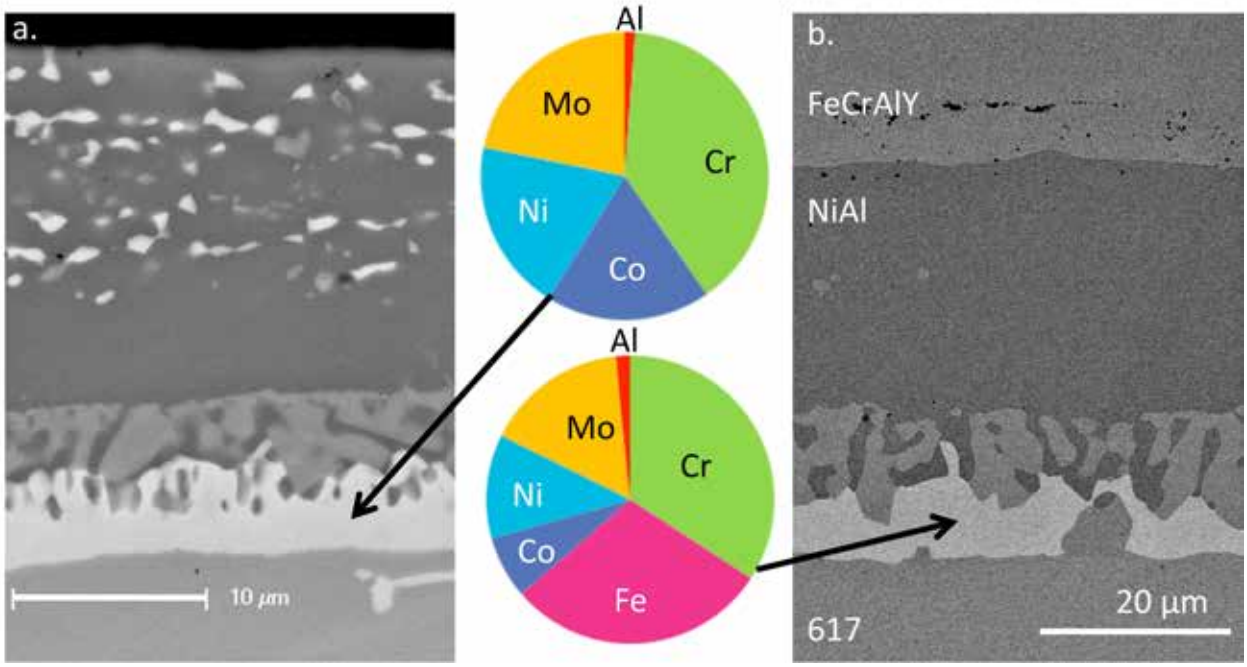

Fig. 2.11. Average composition of sigma layer at NiAl/617 interface in a, aluminized 617 after 16h/1000°C heat treatment and b, clad+aluminized 617 after 168h/1000°C heat treatment. The sigma layer increases in Fe content at the expense of Ni and Co in the clad sample relative to the original layer formed after aluminizing.

The diffusion barrier layers, however, are retained upon heat treatment at 800°C, Figure 2.10, with concomitant evolution of carbides within the matrix, cf. Figure 2.6. The Cr precipitates within the NiAl layer persist after the treatment at 800°C, but are largely eliminated after 500h at 1000°C, especially for the Gen II specimens. Conversely, no $L1_2$ phases develop within the B2 layer in the Gen I or II specimens, in contrast with the behavior observed for Gen I without cladding, Figure 2.3(d).

Two important and related changes in the microstructure of the clad layer develop as interdiffusion proceeds. First, a fine dispersion of precipitates evolves near the interface with the aluminized layer, which recedes gradually as illustrated in Figure 2.12(a,b). TEM analysis in Figure 2.12(c) reveals these precipitates to be B2-(Fe,Ni)Al, 100-200 nm in size, coherent with the matrix. Atom probe tomography (ATP) identified at least two additional distinct populations of Ni-bearing second phases, one in the 10-20nm range and the other comprising nanoclusters under 10 nm in diameter, Figure 2.12(d). These precipitates have been shown to enhance the strength/hardness of the FeCrAlY cladding, which is potentially relevant to the initiation of creep-fatigue damage. However, they tend to coarsen and re-dissolve as the matrix transforms from the b.c.c. (A2) structure, characteristic of FeCrAlY to f.c.c. (A1), with continued Ni diffusion. At the longer times the cladding consists of a A2/B2 outer layer, denoted by β/β' in Figure

2.9, and a region of f.c.c. (A1) solid solution next to the remaining NiAl layer. The evolution is delayed in Gen II specimens relative to Gen I, with no A1 layer present after 168h at 1000°C in the former, Figure 2.9(g), while about half of the clad layer transformed to A1 in the latter, Figure 2.9(c).

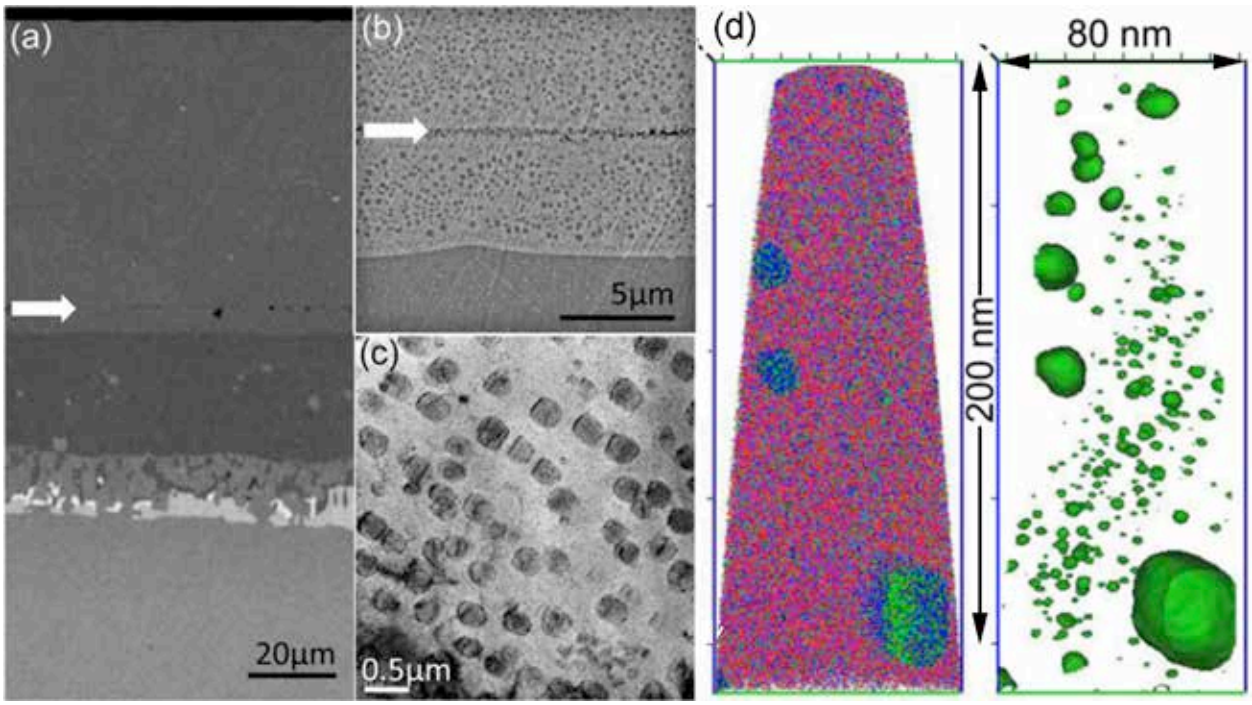

Figure 2.12 - SEM (a,b) and TEM (c) of B2 precipitates that form in clad + aluminized 617 after 24h/1000°C. The arrow in (a,b) denotes the position of the original interface. (d) Atom probe tomography reveals a bimodal distribution of precipitates. The 3-D reconstruction shows all the atoms wherein the color code is: Fe-pink, Cr-orange, Ni-green, Al-blue. The precipitates are highlighted by the isoconcentration profiles at Ni=10at% where the larger precipitates correspond to those visible in (c) and (d), with smaller nanoclusters dispersed in the matrix.

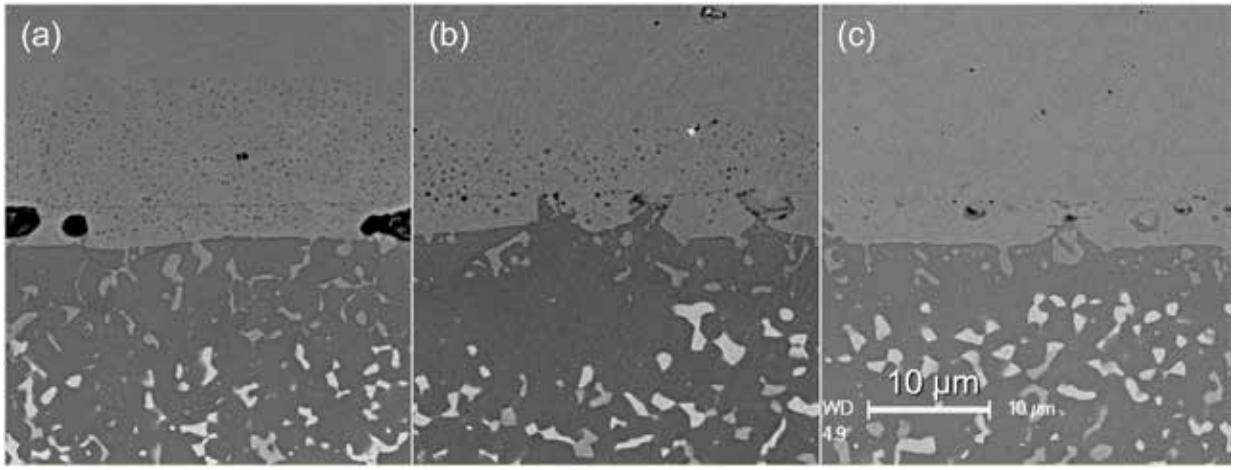

Figure 2.13. SEM images of Gen II clad + aluminized 617 after 800°C heat treatment for (a) 100h, (b) 225h and (c) 375h. The β/β' precipitates that form in the FeCrAlY as Ni diffuses into this layer dissolve with time and are no longer present by 375h.

No evolution of an f.c.c. layer was observed upon heat treatment at 800°C, even after 375 h, Figure 2.10(d). B2 precipitates do evolve, albeit in a finer scale than at 1000°C, but they do redissolve near the interface with the aluminide layer, as shown in Figure 2.13.

To gain additional insight into the interdiffusion phenomena in the absence of the secondary alloying elements diffusion couples were prepared between FeCrAlY foils and two NiAl alloy plates with compositions $Ni_{50}Al_{50}$ and $Ni_{60}Al_{40}$. The results in Figure 2.14 show the critical role of the Ni:Al ratio on the evolution of the FeCrAlY microstructure. Interdiffusion with the stoichiometric NiAl, Figure 2.14(a), results in a relatively thin (20µm) layer depleted in Ni and Al and enriched in Fe and, to a lesser extent, in Cr. The FeCrAlY, however, appears remarkably uniform in composition, with a microstructure consisting of fine B2 precipitates in the A2 matrix (β/β'). In contrast, the FeCrAlY/$Ni_{60}Al_{40}$ couple shows a much larger diffusion-affected region in the B2 region (>100µm), and a large fraction of the FeCrAlY transformed to f.c.c., Figure 2.14(b). Note the abrupt change in the composition profiles within the FeCrAlY layer, with the f.c.c. region containing a much larger Ni:Al ratio than the β/β', which is enriched in Cr. The conversion of the FeCrAlY clad layer from its conventional A2 structure into A1 has important implications to its oxidation behavior, as discussed under Task 3 below.

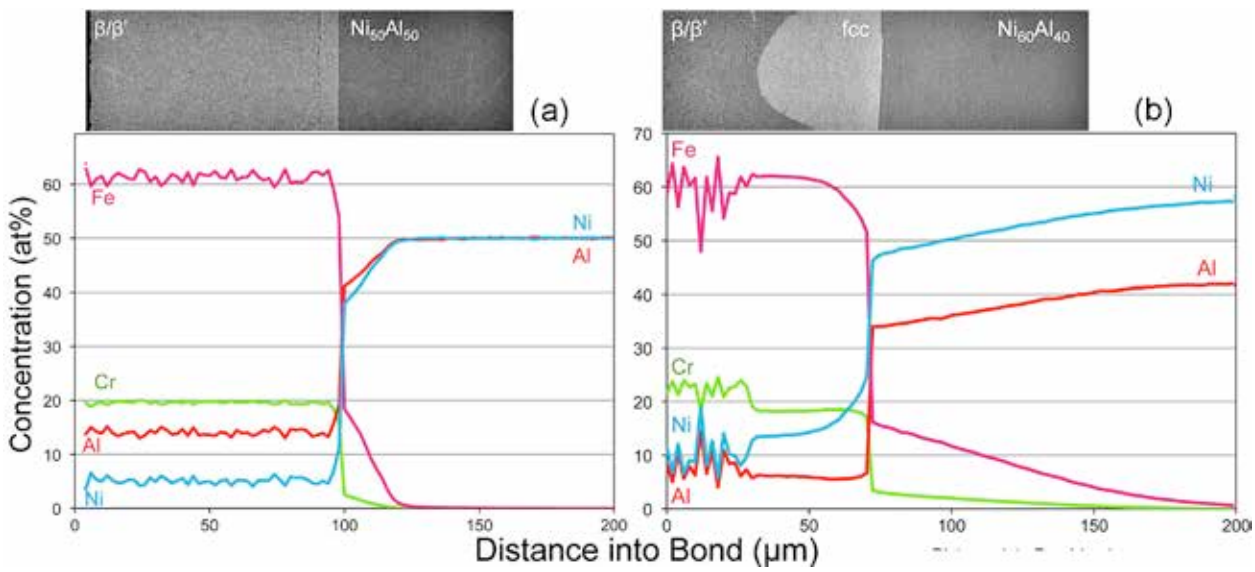

Figure 2.14 - EPMA composition profiles for diffusion couples of 100 µm FeCrAlY layers with 1mm (a) $Ni_{50}Al_{50}$ and (b) $Ni_{60}Al_{40}$ after heat treatments at1000°C/168h in gettered Ar.

Task 3. Exposure to Impure He.

The goal of this task was to evaluate the effectiveness of the alpha alumina barrier relative to the chromia scale typical of uncoated 617 in simulated exposures to impure He without applied load. The findings would also serve as a baseline to understand the effects of mechanical stress when interacting with the environment (Task 4). Because of the constrained dimensions of the environmental exposure chamber[1] the samples were limited to small rectangular coupons, 11 x 5 x 1 mm. The specimens were all pre-oxidized prior to exposure, as described earlier.

For simplicity, carburizing and decarburizing environments were created by adjusting the $CO:CO_2$ ratio (see Section 4.1), and consequently the pO_2, in the flowing He, rather than using the more complex combination of $H_2O/CH_4/CO$ impurities characteristic of the real application. Exposures were performed at temperatures of 800-1000°C for times up to 500 h. The decarburizing environment involved $CO:CO_2$ ~9 and $CO+CO_2$ ~15 ppm, with $X_O \approx 10^{-21}$ while carburizing was produced using $CO:CO_2$ ~1272 and $CO+CO_2$ ~1910 ppm, with $X_O \approx 10^{-24}$.

The weight changes per unit area during exposure to impure He are plotted in Figure 3.1 for uncoated, aluminized, and aluminized+clad 617. In general, the aluminized samples exhibit superior environmental resistance at comparable temperatures in both carburizing and decarburizing environments relative to uncoated 617. The scale in the aluminized specimens, shown in Figure 3.2(a,b), had grown over time but remained similar to that produced during the pre-oxidation treatment, i.e. dense, continuous alpha alumina, whereas the scale in the uncoated 617 (not shown) was chromia, which is less stable in similar environments as reported elsewhere.[2,3]

The aluminized+clad samples were found to behave generally worse than the uncoated 617 in the both carburizing and decarburizing environments. This was originally ascribed to damage associated with trimming of the excess cladding. In essence, all samples were clad leaving excess FeCrAlY foil on the sides to ensure complete coverage of the aluminized surfaces, except for the thin edges, which could not be properly diffusion bonded in the same operation. The excess cladding was then trimmed, largely to ensure the specimens fitted in the narrow tube furnace used for the impure He exposures. To avoid damaging the aluminized edges the trimming left a 1 mm "overhang" on each side. The first trimming approach used mechanical shearing, which was found to result in significant edge damage with increased environmental interaction, as described below. The external appearance of the specimen suggested substantial reaction of the overhang cladding surface and neighboring region, as shown by the darkened region in Figure 3.3(a). The center of the specimen, however, appeared much less affected by the exposure, retaining the alumina scale and a similar evolution of A2 into A1 and A2/B2 observed in the oxidation in gettered Ar – see Figure 3.4.

---

1 D. Kumar, C. J. Torbet, and G. S. Was, "A facility for conducting high-temperature oxidation experiments of alloys in helium environments containing part per million levels of impurities," *Measurement Science and Technology,* **20** 095708 (095701-095711), (2009).

2 D. Kumar and G. S. Was, "Mechanism of Decarburization of Alloy 617 at 1000°C in Helium Containing CO and CO_2," in *Materials for Future Fusion and Fission Technologies,* Edited by C. C. Fu, A. Kimura, M. Samaras, M. Serrano de Caro, and R. E. Stoller., **MRS Symposium Proceedings vol. 1125**, Materials Research Society, Pittsburgh, PA, (2009).

3 D. Kumar, R. Adharapurapu, T. M. Pollock, and G. S. Was, "High-Temperature Oxidation of Alloy 617 in Helium Containing Part-Per-Million Levels of CO and CO_2 as Impurities," *Metallurgical and Materials Transactions,* **42A** [5] 1245-1265, (2011).

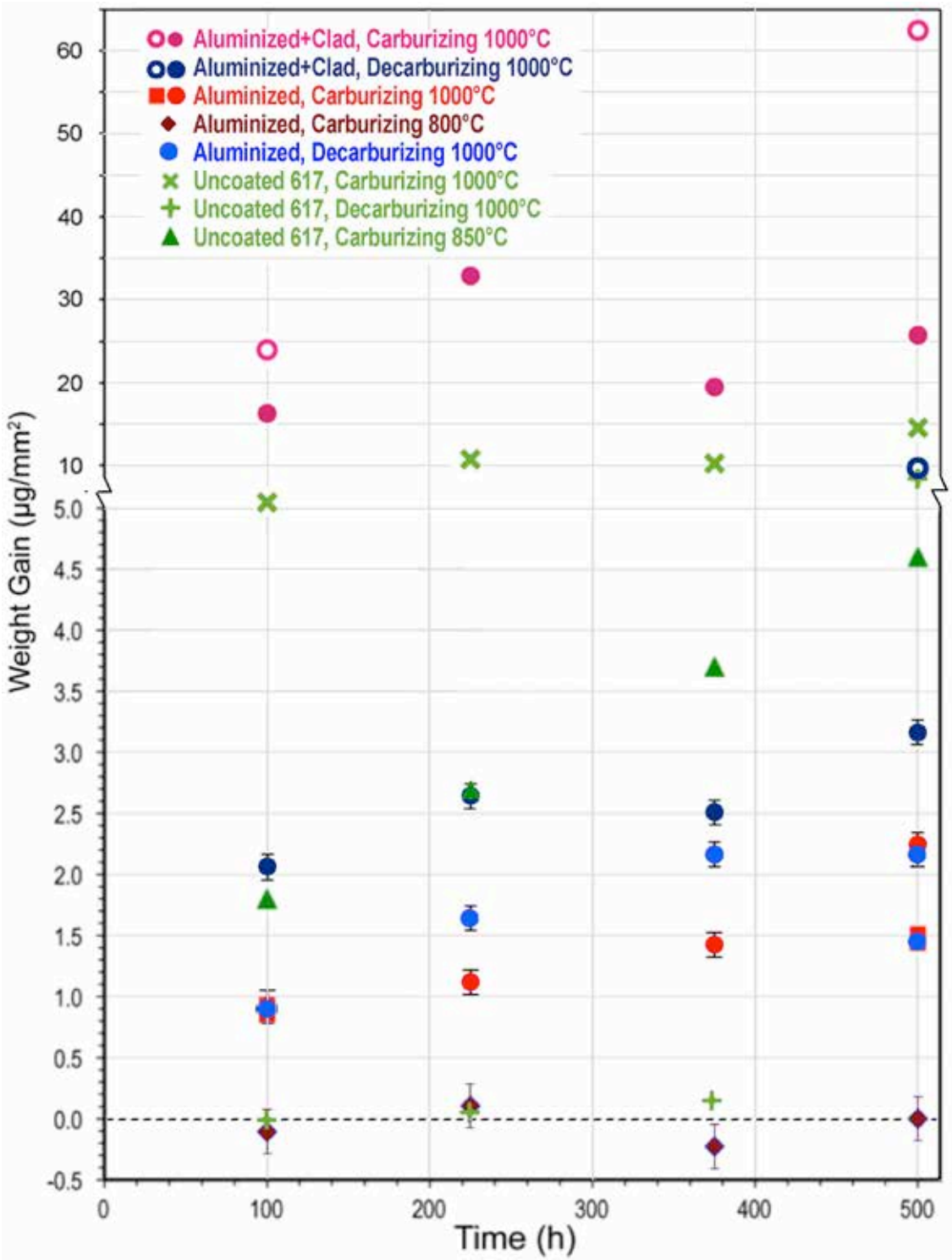

Figure 3.1 - Normalized weight gains for uncoated, aluminized and aluminized+FeCrAlY clad specimens of 617, exposed to impure He environments at different temperatures and for different times. Note the change in scale between 5 and 10 mg/mm^2. All the coated samples were pre-oxidized prior to exposure. The environments impure He with $CO:CO_2 \approx 1272$ (carburizing) or $CO:CO_2 \approx 9$ (decarburizing). The FeCrAlY in the aluminized+clad specimens covered only the broad sides of the aluminized specimen. Empty circles in the clad specimens correspond to those in which the cladding was trimmed mechanically, whereas solid circles are for laser-trimmed specimens.

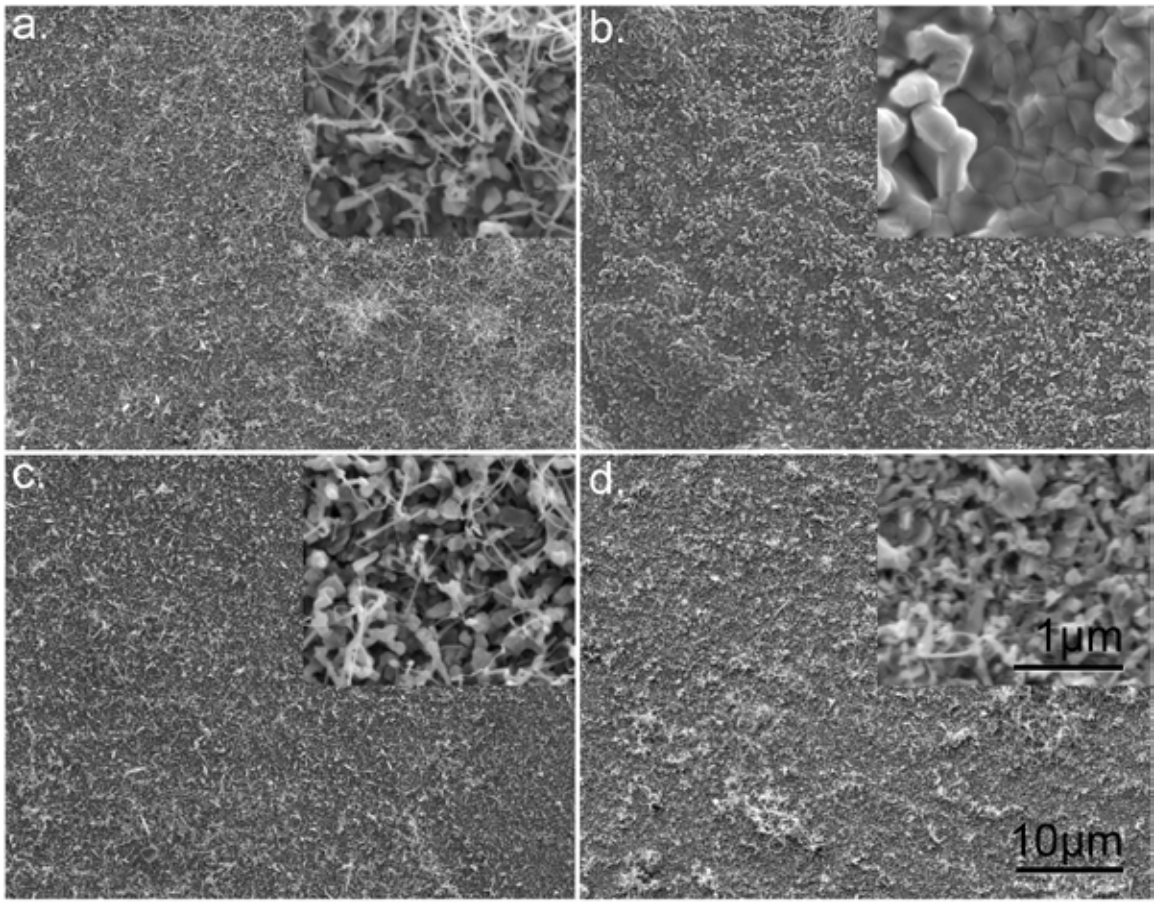

Figure 3.2 - SEM images of the oxide morphology after 1000°C/500h exposure to impure He of aluminized 617 in (a), carburizing and (b), decarburizing conditions and clad + aluminized 617 in (c), carburizing and (d), decarburizing conditions.

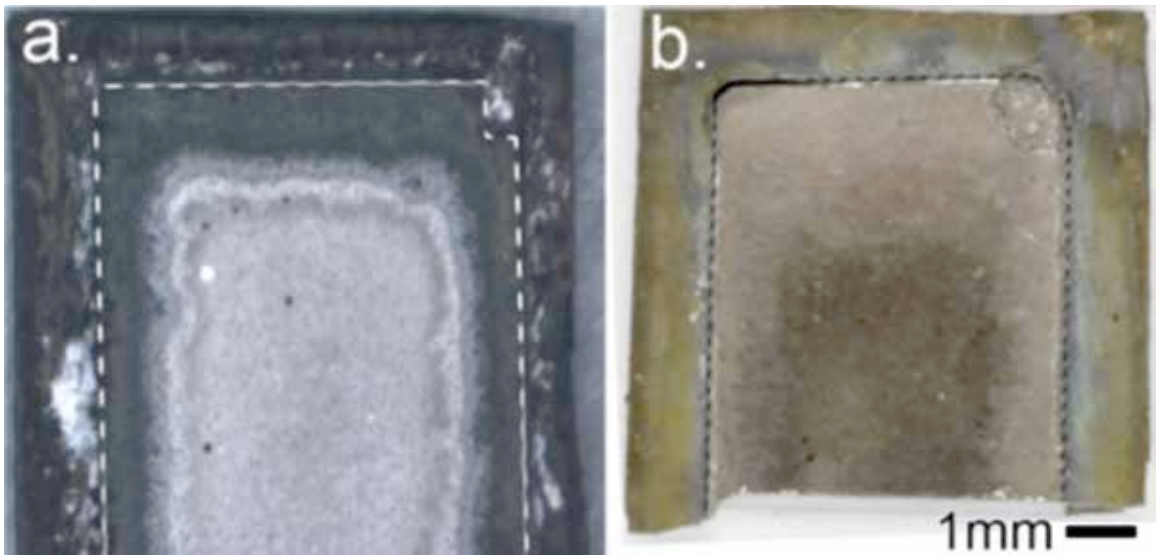

Figure 3.3. Optical images of clad + aluminized 617 specimen surfaces after exposure to 500h/1000°C/ carburizing He. The dashed line denotes the profile of the aluminized 617 substrate underneath, with the cladding overhang around it. The specimen in (a) had the excess cladding mechanically trimmed whereas (b) was laser-trimmed.

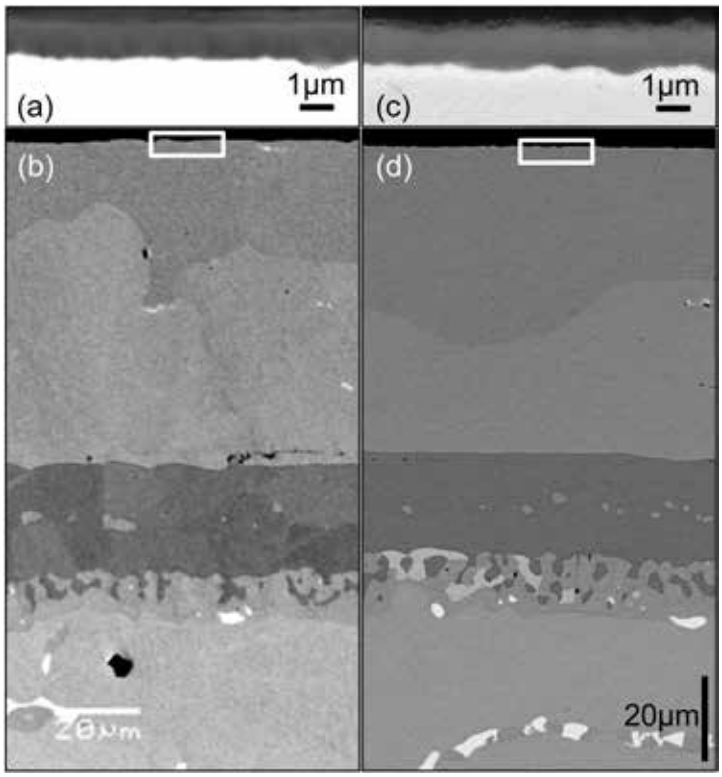

Figure 3.4 - SEM images of clad + aluminized 617 after 500h exposures in (a,b) decarburizing and (c,d) carburizing environments. Though the edges suffered some damage, the central area of the exposed surface maintained a protective alpha alumina scale.

In a second approach the excess cladding was trimmed using a pulsed femtosecond laser known to yield minimal collateral damage or thermal distortions that could initiate delamination from the substrate. The performance under carburization was much improved, as shown by comparison of Figures 3.3(a) and (b). The structure of the scale was similar to that evolving on the aluminized-only specimens after 500h (cf. Figure 3.2c,d), and the cross section was similar to that in Figure 3.4.

It was not immediately evident what might have caused the difference in behavior of the overhang portion of the cladding, unless there was damage to the cladding material during the mechanical shearing process. To explore that possibility two different tests were undertaken. In one case preoxidized FeCrAlY coupons of similar dimensions were exposed to both carburizing and de-carburizing environments to evaluate the intrinsic resistance of the cladding to these environments. These tests yielded maximum weight gains $\leq$1.6 mg/mm^2, comparable to those of the aluminized 617 specimens in Figure 3.1. A second test explored the possibility that the excessive weight gain was associated with damage to the original scale. The surface of the preoxidized specimens was indented to crack the scale, and the specimen was then exposed to the carburizing environment. The results, shown in Figure 3.5, revealed that the FeCrAlY was sufficiently robust to regenerate the alumina scale in the damaged areas before any significant carburization could take place. The morphology of the oxide in Figures 3.5(c,d) suggests some transient alumina formation prior to the conversion to alpha. Since the diffusion of C through alpha alumina is very slow, it was then deemed unlikely that the excess weight gain was due to poor resistance of FeCrAlY against carburization.

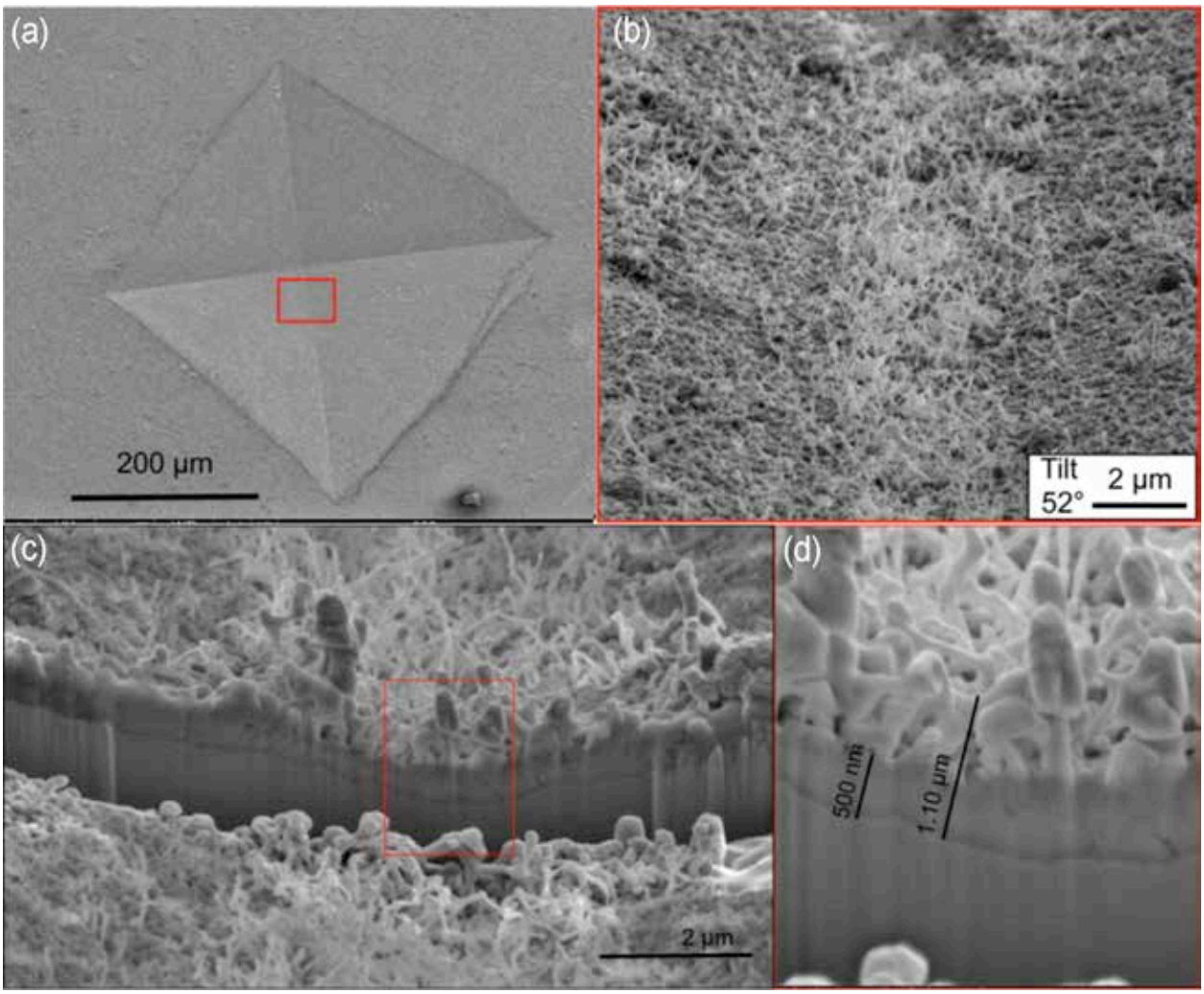

Figure 3.5 - Images of indented FeCrAlY after exposure to a carburizing enviroment for 100h at 1000°C. (a) overview of the indent after exposure. (b) close-up of the oxide scale that reformed along the diagonal of the indent during exposure. The area of the detail is marked in the left image by the red rectangle in (a). (c) SEM image of a FIB cross section made through diagonal of indented region in (b) wherein the damaged oxide exposed the underlying alloy to a carburizing environment. (d) detail of the regenerated alumina scale, wherein the alloy and interface show no evidence of carbide formation upon exposure.

Cross sections of the corners of specimens corresponding to the two different trimming approaches are shown in Figure 3.6. The damage is quite severe in the mechanically trimmed samples, Figure 3.6(a,b), and proceeds from the corner along the boundary between the cladding and the NiAl layer. The penetration in Figure 3.6(b) is consistent with the damage observed in Figure 3.3(a). Figure 3.7 shows that both the cladding and the neighboring aluminized layer have been substantially affected, with extensive oxidation and carburization. The cladding seems to have been incorporated a major fraction of Ni and reduced the Cr so it is likely to have transformed completely into f.c.c. (A1) and the aluminized layer has also been depleted in Al presumably due to the severe oxidation (darker areas in Figure 3.7). A surprising observation is that the edges of the 617 substrate, which were aluminized but not clad, showed little change after 100h but severe degradation after 500h, Figures 3.6(a,b), even though the surfaces of the aluminized-only specimens experienced no significant damage.

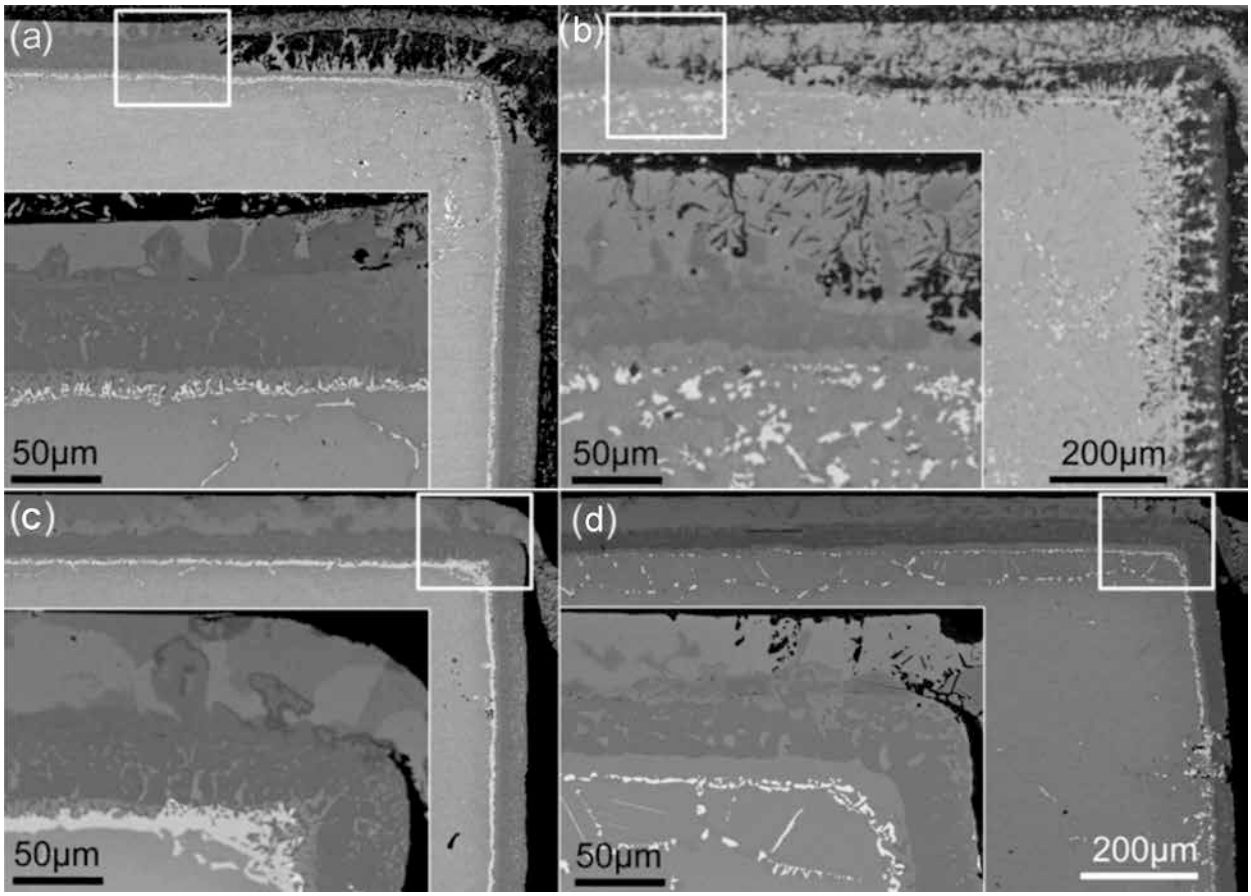

Figure 3.6 - SEM images of clad + aluminized samples exposed to a carburizing He environment at 1000°C for (a,c) 100h and (b,d) 500h. Samples that were laser trimmed (c,d) showed less attack than samples that suffered more evident damage during mechanical trimming (a,b) prior to exposure.

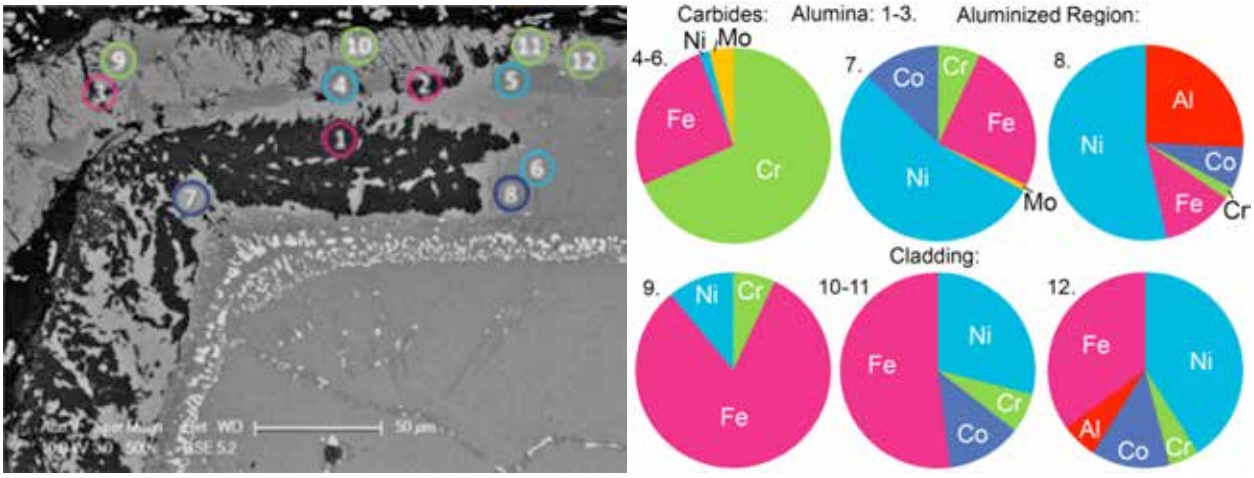

Figure 3.7 - Cross section of a corner of a mechanically trimmed clad + aluminized 617 sample after exposure to a carburizing He/1000°C/100h. The spots in the micrograph correspond to EDX compositions shown on below the image. Damage to the sample prior to exposure resulted in severe oxidation (1-3) and carburization (4-6). The aluminized (7-8) and clad (9-12) regions were depleted in aluminum and also chromium in the case of the cladding.

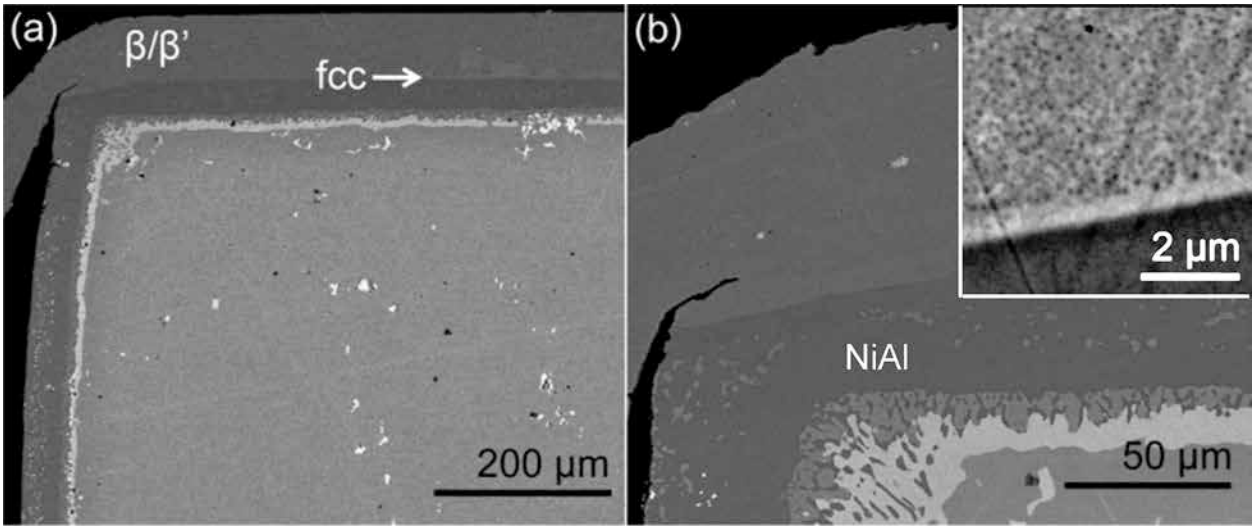

Figure 3.8 - SEM images of a clad + aluminized sample that was laser-trimmed prior to exposure to a carburizing He environment at 1000°C/100h. Away from the edge, the FeCrAlY cladding has begun to transform to fcc (a), but the edge, which is free from carbides (b) still retains the β/β' microstructure seen at higher magnifications in the inset.

The cross sections in Figure 3.6(c,d) show the remarkable reduction in damage when the specimens were laser-trimmed. There is interdiffusion between the cladding and the aluminized layer, as well a some oxidation and possibly some carburization, but only a small crack at the corner that does not seem to advance significantly between 100 and 500h. Details from the 100h exposure are given in Figure 3.8. In this region the FeCrAlY still retains largely the ferritic structure with B2 precipitates (β/β'). Some initial transformation to f.c.c is observed at the interface away from the corner in Figure 3.8(a). Note also the absence of any degradation at the un-clad edges after 100h, which preserve the aluminized structure, although the 500h specimen in Figure 3.6(d) does show some blemishes in the equivalent region.

Additional insight into the effects of interdiffusion on the degradation behavior of the clad specimens when the environment has access to the interface is provided by the micrographs in Figure 3.11. A sample initially exposed for 100h/1000°C to the decarburizing He environment, experiencing some formation of A1 solid solution at the interface between the NiAl and FeCrAlY, was sectioned and subsequently exposed to a short oxidation treatment for 1h at 1000°C in gettered Ar. A remarkable difference in oxidation behavior ensued, with the f.c.c. forming a chromia scale and the β/β' structure in the upper part of the FeCrAlY forming alumina, which also evolved on the sectioned NiAl surface. The implication is that when a carburizing environment access a region of the interface that has transformed to f.c.c., through an edge crack, the subsequent oxidation may not be protective as it is on the NiAl or even the ferritic FeCrAlY. Further work is needed to clarify these details. It should be noted, however, that there was no significant evidence that severe degradation at edges occurred in the creep tests, even in the carburizing environment, as discussed in Task 4.

One final observation of interest was the slightly lower weight gain in the carburizing environment for the aluminized-only 617 in Figure 3.1, in spite of the absence of any incorporation of contaminants other than the growth of the scale. This observation is consistent with the lower pO_2 in the oxidation environment, which would be conducive, in principle, to slower oxide growth. This effect remains to be properly quantified by additional research.

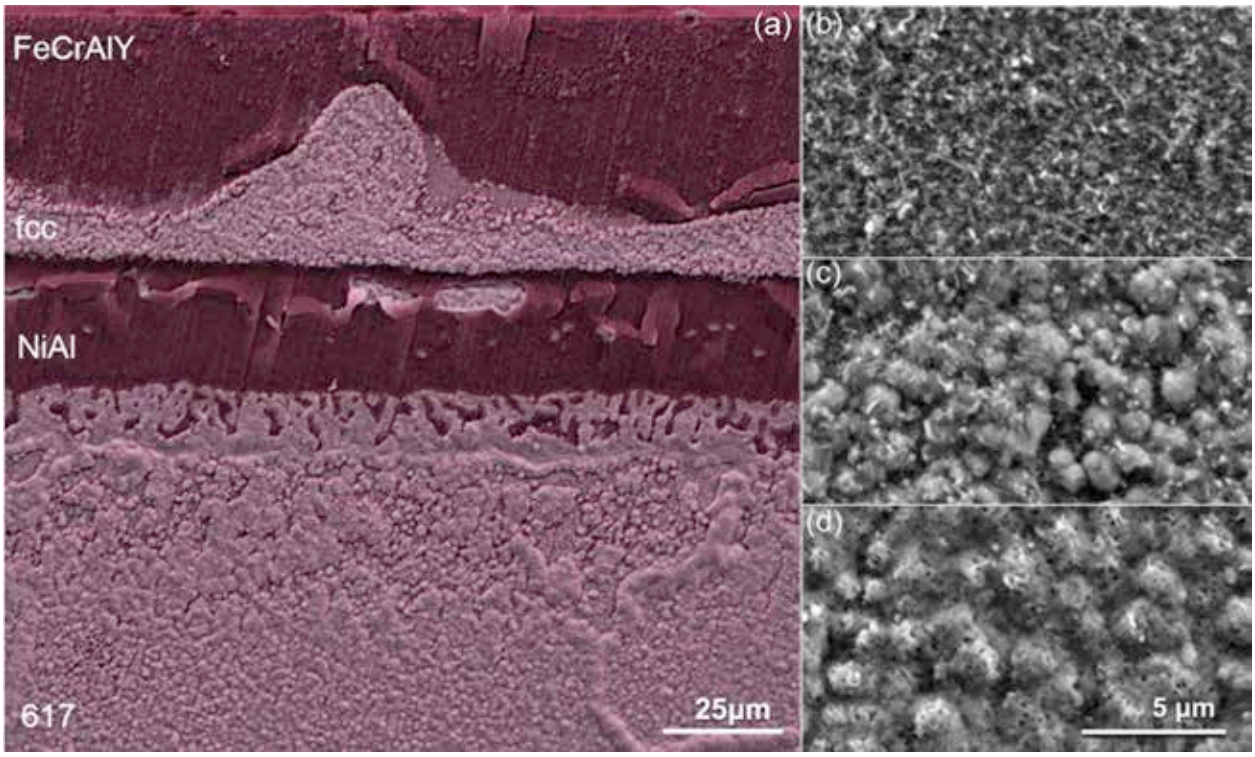

Figure 3.9 - SEM images of the cross section of a Gen I clad + aluminized 617 sample that had undergone 100h/1000°C/decarburizing He prior to cross-sectioning and oxidation for 1h/1000°C/gettered Ar. The β/β' microstructure and NiAl layer formed alumina, shown at higher magnification in (b). The region where the original FeCrAlY layer had been replaced by γ (A1) formed chromia, and its morphology (c) was similar to the chromia formed by alloy 617 (d).

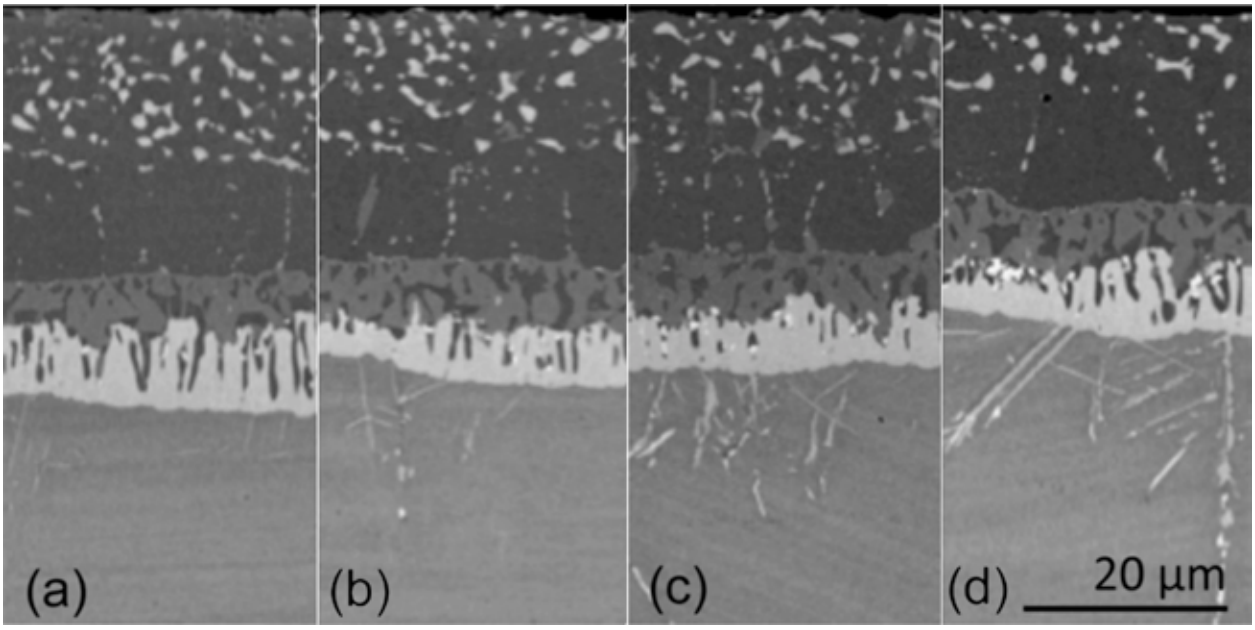

Figure 3.10 - SEM images of the coating cross-section after 800°C exposure to impure He ($CO:CO_2$ ≈ 1272) for (a) 100h, (b) 225h, (c) 375h, and (d) 500h.

Experiments on aluminized-only specimens were also performed at 800°C, primarily in the carburization environment that proved to be the more aggressive for these systems. Figure 3.10 shows the evolution of the microstructure as a function of time. The Cr-rich precipitates within the NiAl are still retained, although there is some indication of carbide evolution (the regions intermediate in brightness between the NiAl matrix and the Cr precipitates). It is not clear if this is a result of some C ingress from the environment, which was not observed at higher temperatures and would be hindered by the presence of the original alumina barrier. There is also evolution of carbides under the sigma layer, shown in greater detail in Figure 3.11. TEM analysis revealed the presence of both $M_{23}C_6$ and M_6C carbides, as well as discrete sigma precipitates and incipient formation of $L1_2$, the latter also found in greater proportions at higher temperatures. Additional insight on the robustness of the aluminized layer against carburization was provided by creep experiments on FIB-notched specimens described in Section 4.4.

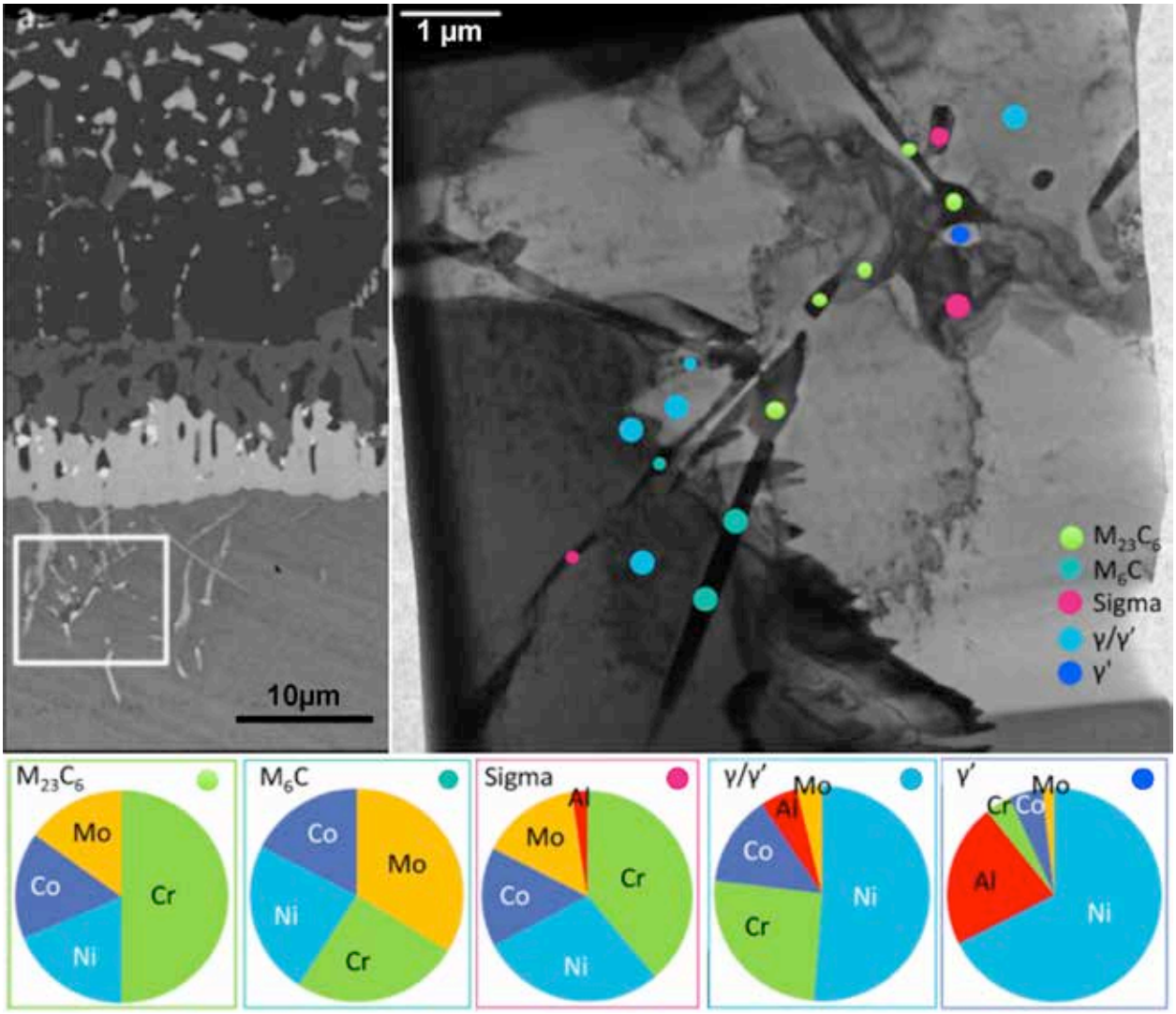

Figure 3.11 - TEM image of the DAZ of aluminized 617 after 800°C/375h/carburizing He exposure showing EDS measurements and expected phase based on composition, cf. Figure 3.9(c).

Task 4. Performance of Barrier Layers under Creep in Impure He

The objective of this task was to develop an understanding of the mechanical performance of Al-forming barrier layers, NiAl and FeCrAlY, during static and cyclic creep of 617 in impure helium environments. Following are the lessons learned and the main findings:

- A creep system with the capability of performing static and cyclic loading experiments of uncoated and coated 617 in controlled impure helium environments.
- Creep deformation of uncoated 617 at 800°C in impure He increased damage accumulation (crack formation and growth), compared to exposures in the absence of mechanical load.
- Damage observed in uncoated 617 specimens during creep was largely suppressed by the proposed coating concepts, comprising NiAl or NiAl + FeCrAlY barrier layers.
- While no cracking of the NiAl layer was observed in either cyclic or static creep when cladding was absence, the addition of the thin FeCrAlY layer led to cracks in the NiAl layer, which did not grow to the surface and exhibited only limited propagation into the substrate.
- Cyclic creep of NiAl/617 produced no crack growth from FIB micronotches placed on the NiAl coating surface, confirming the strong resistance of the NiAl to creep damage in impure He environments.
- The possible causes for NiAl cracking during creep when FeCrAlY cladding is added will continue to be investigated, albeit in a limited way because of the lack of funding.

4.1. Development of Experimental Facilities

As part of this project, instrumentation was constructed to conduct both static and cyclic creep experiments in helium with controlled levels of impurities such as CO and CO_2. Design of the system was based on the success of an exposure-only system described elsewhere.[4] As shown in Figure 4.1 and Figure 4.2, the system consists of three major sections: a gas mixing section, an environmental exposure section fitted for mechanical testing, and a gas analysis section. The gas mixing section provides the capability of generating the desired concentration of O_2, CO and CO_2 in the creep retort using premixed bottles of helium, each with a given level of one type of impurity, and a series of mass flow controllers. Most of the experiments were done in a carburizing environment, $CO/CO_2 >> 1$, which was found to be the most deleterious. The helium with controlled levels of CO and CO_2 is passed through the exposure-mechanical testing section in which the sides of the pin-loaded specimen are exposed to the flowing gas. A needle valve at the entrance of the furnace is used to control the flow rate of the gas mixture through this section. The CO and CO_2 levels in the helium are analyzed continuously both before and after the entry into the furnace using the discharge ionization detector gas chromatograph in the analysis section. Experimental variables such as flow rates of gases and concentration levels of impurities are continuously monitored by a data acquisition system. The sections hereafter describe the different experiments in detail.

[4] D. Kumar, C. J. Torbet, and G. S. Was, "A facility for conducting high-temperature oxidation experiments of alloys in helium environments containing part per million levels of impurities," *Meas. Sci. Technol.*, vol. 20, no. 9, p. 095708, Sep. 2009.

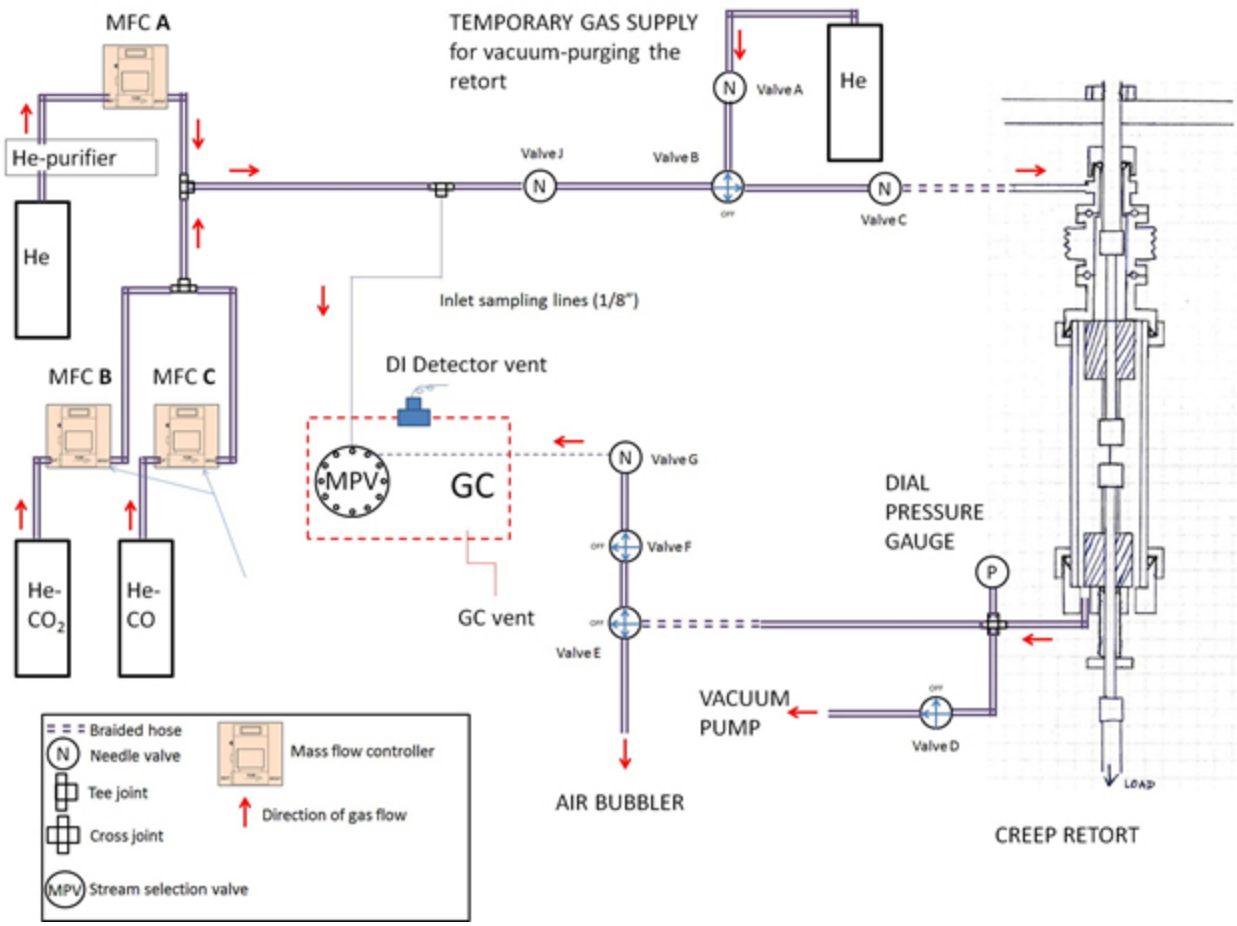

Figure 4.1 - Schematic of the controlled-impurity-flow creep system showing the major sections: gas mixing (MFCs), exposure-mechanical testing (creep retort), and the gas analysis section (GC).

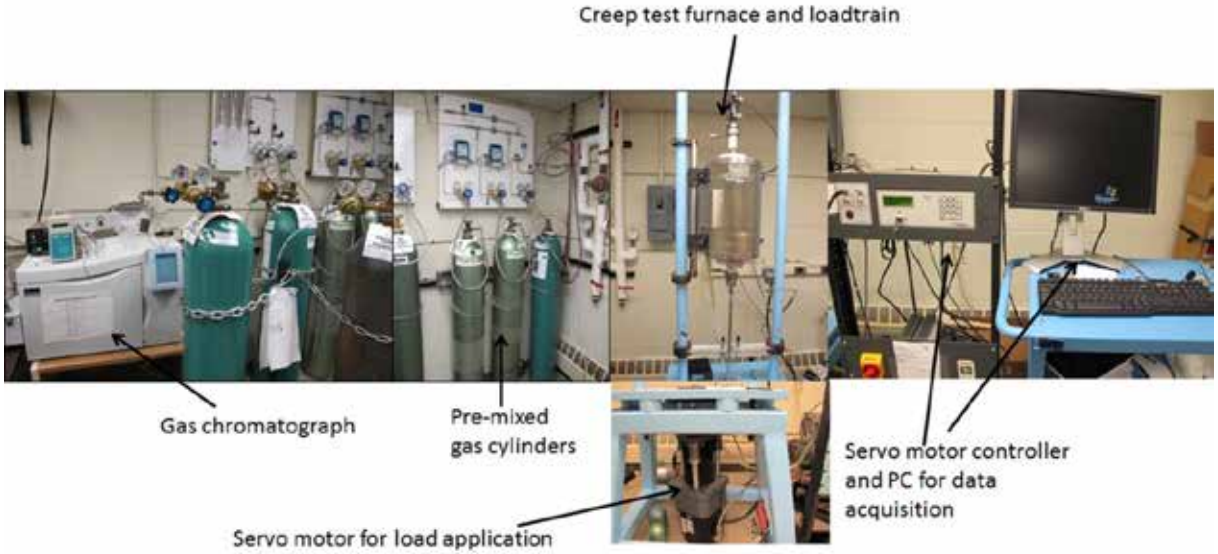

Figure 4.2 - Photograph of the assembled controlled-impurity-flow creep system.

The gas mixing section consists of 3 pre-mixed gas bottles and 3 mass flow controllers. To obtain the gas mixture with the target concentration of each impurity, a pre-mixed gas cylinder of helium with a certified level of one impurity, and a controlled amount of another impurity from a different certified pre-mixed bottle were combined using electronic mass flow controllers. The resulting gas mixture was then diluted, if required, by mixing it with research grade helium of 99.9999% purity. The electronic mass flow controller used for gas mixing had an accuracy of ±1 ml/min with a full scale operation range of 0 to 200 ml/min, and was capable of withstanding pressure up to 500 PSIG. All the components involved in transporting and mixing the gases were made from stainless steel 316. Whenever possible, welded fittings were used for connecting lines from different gas bottles to avoid the in-leakage of air.

In the creep retort, a pin-loaded specimen is subjected to static or cyclic load applied via the load train. Before and during creep tests a flow of He containing the desired impurity levels is established and maintained. The main components of the system are the creep frame, the specimen chamber, the servomotor and the servo-controller unit (Figs. 4.1-4.3). The creep frame was made of stainless steel columns and a base for assembling the load train, the furnace and the servomotor unit. The specimen chamber has the minimum dimensions (38 mm internal diameter, 42 mm external diameter) necessary to house the specimen, the thermocouple wires, the load train, and a porous alumina barrier within the hot zone. Porous alumina was used as a heat shield for the O-rings in the water-cooled, 304 stainless steel chamber end seals. Three thermocouples were used to monitor temperatures at the middle and both ends of the gauge section of the specimen. The load train components in the high temperature zone of the furnace were carefully designed to withstand both high loads (strength and creep resistance) as well as to resist corrosion. The load train components were machined from high-temperature TZM alloy and the specimen grips were made from Mar-M-247 alloy. In order to protect these components from corrosion in impure helium, the TZM cylindrical load train components were coated with high temperature boron nitride lubricant and encased in 99.99% pure alumina tubes with minimal clearance. Since the thermal expansion coefficient of TZM is very low, the components did not exhibit any significant thermal expansion that would crack the alumina casings.

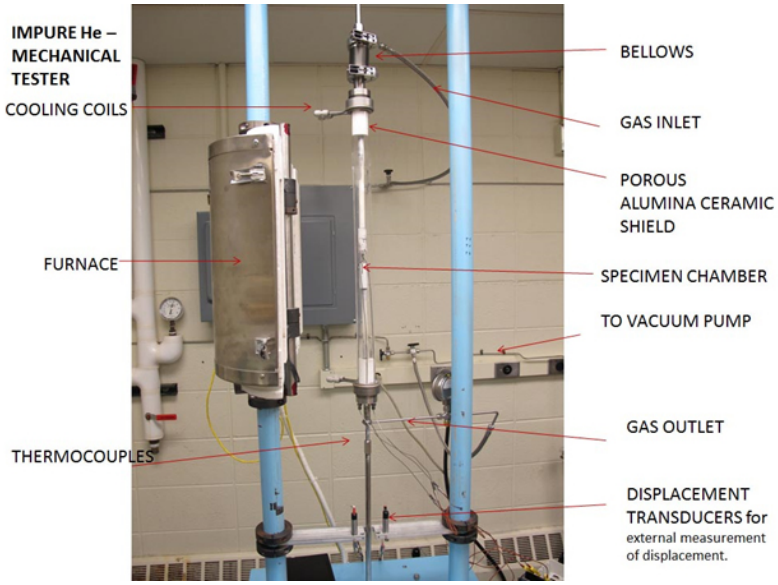

Figure 4.3 - The custom-built creep frame for exposure-mechanical tests in impure helium environments.

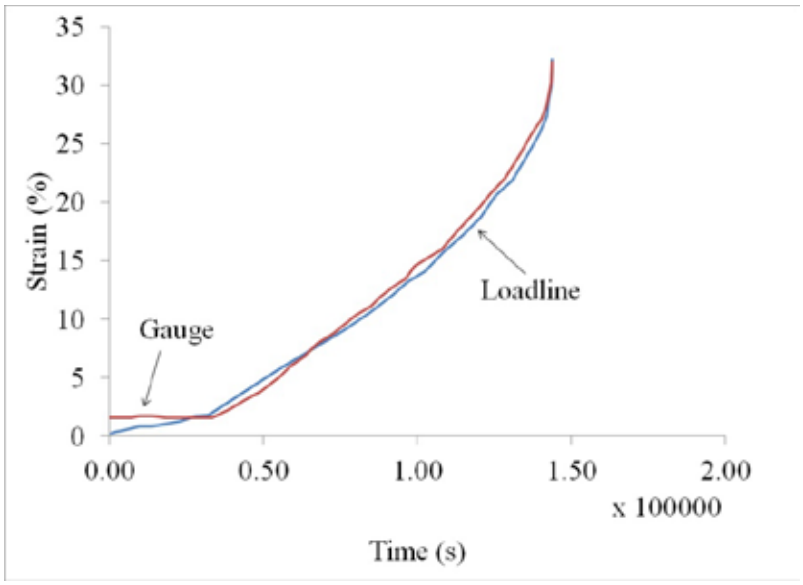

Figure 4.4 - Strain versus time data for Alloy 617 showing the reproducibility of strain measurements taken at two different locations: loadline and gauge.

Strain measurements were performed near the load line (bottom) as shown in Figure 4.3. It was demonstrated that the measurement of strain could be determined from two different locations with similar results (Figure 4.4). Usually, the strains are measured directly from the gauge section in the hot zone. However, if the strains are determined via the load line displacement instead of the gauge length deformation, the creep system is simplified since extra components near the specimen, which are exposed to the gaseous environment, are reduced. This minimizes the error in estimating the gas consumption during the creep testing.

A closed loop, digitally controlled servomotor enabled the application of both static and cyclic stresses during testing. The motor is controlled via the control panel from where one can manually or remotely configure the control of the load and displacement in real-time. A built-in waveform generator can be programmed to cycle or ramp the control point for the duration of the creep tests. Since the servomotor contains a closed loop digital PID controller, the control point was accurately manipulated in real time. The control panel has an RS-232 serial port enabling a computer to have full control of the servomotor for improved functionality. Load control and data collection were customized using LabView.

The gas-analysis section consists of a discharge ionization detector gas chromatograph (DIDGC) and computer (PC), Figs. 4.1 and 4.2. The DIDGC was used to continuously analyze the gas mixture at both the entrance to and exit from the retort, and the PC was used to control the system. The details of the functioning of the gas chromatograph have been described elsewhere[4].

4.2. Surface degradation of uncoated 617 subjected to stress and impure He

Static and cyclic creep tests were conducted in three different environments (nominally pure helium, He-0.1ppm O_2, slightly oxidizing, He-8ppm O_2; and slightly carburizing/oxidizing, He-CO/CO_2 =1320) at 800°C. Creep tests were carried out to the same nominal strains to allow comparison of damage as a function of strain level. The objective of these tests was to study the role of environment on the type of degradation of Alloy 617 under both static and cyclic loading.

The experimental procedures have been provided in detail elsewhere.[5,6] The influence of creep deformation on damage accumulation in Alloy 617 during exposure to the carburizing/oxidizing environment was studied by comparing the results of the creep test with the results of an exposure test of a similar alloy at 850°C with no applied mechanical load.

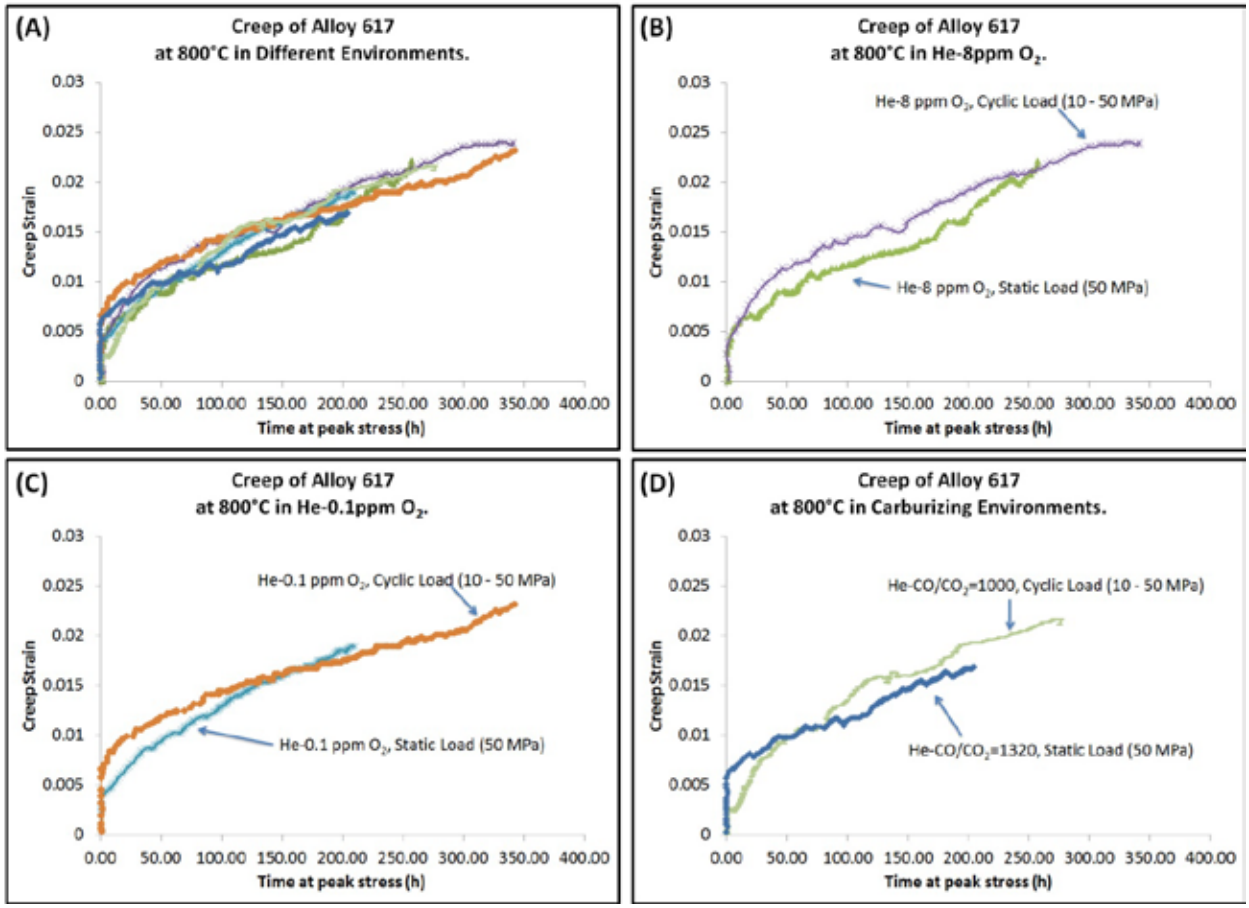

Figure 4.5 - Creep curves of Alloy 617 tested at 800°C in different environments. Six creep curves in three different environments are plotted in A, and the curves for each environment and load are shown in B, C and D keeping the same color coding. Two tests (static and cyclic load) were conducted for each of the He-8ppm O_2, He-0.1ppm O_2, and He-CO/CO_2=1320 environments.

The creep curves of the three tests are shown in Figure 4.5 and details are provided in Table 4.1. The creep curves follow similar trends and the steady state creep rates are similar. Cyclic loading does not seem to have an observable effect on the creep behavior, as the steady state creep rates are similar for both cyclic and static loading. The overall creep rate is also not influenced by differences in the test environment. The effect of the environment on the nature of the creep deformation is still unresolved for Alloy 617. Mino et al [7] concluded that there is no significant influence of the atmosphere on the steady-state regime of the creep of Alloy 617 under a stress of 90

[5] G. S. Was, J. W. Jones, G. Gulsoy, and A. O. Okello, "NEUP 09-678 Quarterly Progress Report Y4Q2," 2013.
[6] G. S. Was, J. W. Jones, G. Gulsoy, and A. O. Okello, "NEUP 09-678 Quarterly Progress Report Y3Q4," 2012.
[7] K. Mino, "Effect of Simulated HTR Helium Atmosphere on Creep Rupture Properties of Nickel-Base Wrought Alloys," *Tokyo 135-91. Trans. Iron Steel Inst. Japan*, vol. 23, no. 10, pp. 815–823, 1983.

MPa. This conclusion contradicts that one of Shankar,[8] who reports that the secondary creep rates of the curves for carburizing and oxidizing environments were significantly different. In fact, Shankar observed that the carburizing environment had the effect of lengthening the creep life while he identified shorter lives with the oxidizing environment. It should be noted, however, that the test environments used by Mino and Shankar are different from the carburizing environment used for the tests described in this report. While the tests they report are in carburizing environments, the environments used in the present work have a slight oxidation potential compared to the reducing environment in the tests by Mino and Shankar. The other reason for the different results observed in this report could reside in the nature of the tests. Mino and Shankar conducted longer creep tests up to failure. However, in the present work, tests were interrupted long before failure to examine the influence of creep deformation on the surface degradation prior to the onset of general bulk creep damage. Longer creep tests under the carefully controlled environments developed here would be of interest in a potential extension of this project.

Table 4.1 - Interrupted creep results on uncoated 617 at 800°C in different impure He environments.

Environment	Load	Strain (%)	Minimum Creep Rate (10^{-8}/s)	Test Time (h)
He - <0.1ppm O_2	Static (50 MPa)	1.9	1.7	211
	Cyclic (10-50 MPa)	2.3	0.94	690
He - 8ppm O_2	Static (50 MPa)	2.2	1.1	258
	Cyclic (10-50 MPa)	2.4	1.3	685
He–CO/ CO_2=1320	Static (50 MPa)	1.7	1.3	206
He–CO/ CO_2=1000	Cyclic (10-50 MPa)	2.1	1.4	553

Observation of the specimen surfaces before sectioning revealed the presence of intergranular cracks (Figures 4.6 - 4.8) but no transgranular cracking. Microstructural cross-sections of the crept alloy in the different environments are shown in Figures 4.9 – 4.11 and the details of the internal damage are indicated in Table 4.2.

The composition of the impure He environment has an effect on the surface degradation of Alloy 617. As indicated in Table 4.2 the number of cracks, the crack depth and the thickness of the surface oxide increase as the purity of the helium gas decreases (from He-0.1ppm O_2 to He-CO/CO_2=1320). In particular the damage accumulation is significantly greater in the CO/CO_2 carburizing environment. Cracks that formed in the pure and slightly oxidizing helium environments, Figs. 4.9 and 4.10, respectively, were shorter and there was no substantive presence of chromia within the cracks aside from the surface scale, compared to the damage seen in the CO/CO_2 environment (Figure 4.11). The damage in the carburizing environment was more severe in two aspects. First, the lengths of the cracks were greater (Figure 4.11) and, second, the subsurface part of the alloy saw an increase in the presence of internal carbides (Figure 4.12).

[8] P. Shankar and K. Natesan, "Effect of trace impurities in helium on the creep behavior of Alloy 617 for very high temperature reactor applications," *J. Nucl. Mater.*, vol. 366, no. 1–2, pp. 28–36, Jun. 2007.

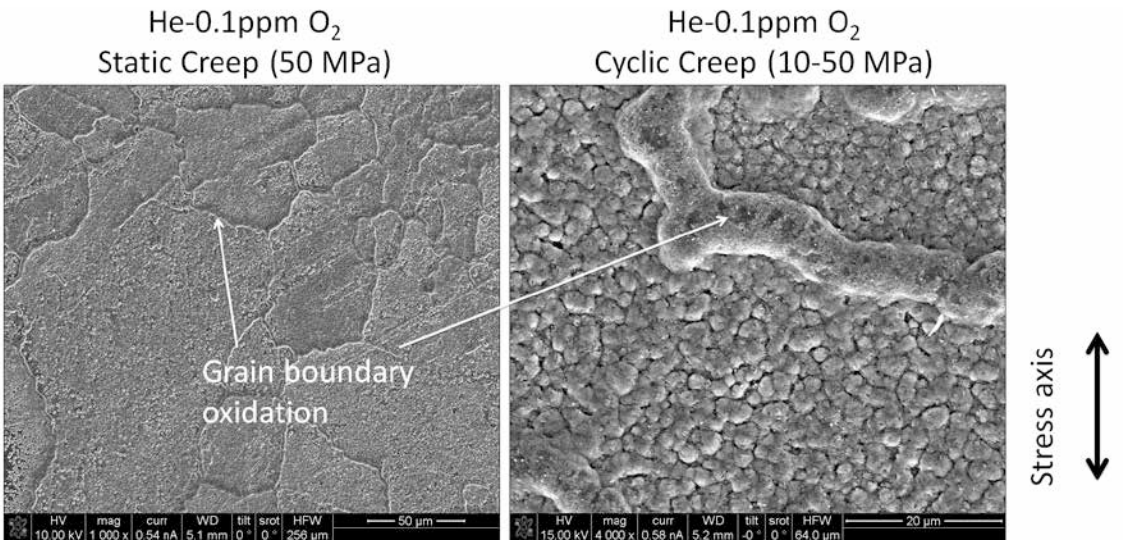

Figure 4.6 - SEM images showing surface damage of Alloy 617 crept at 800°C in He-<0.1ppm O_2.

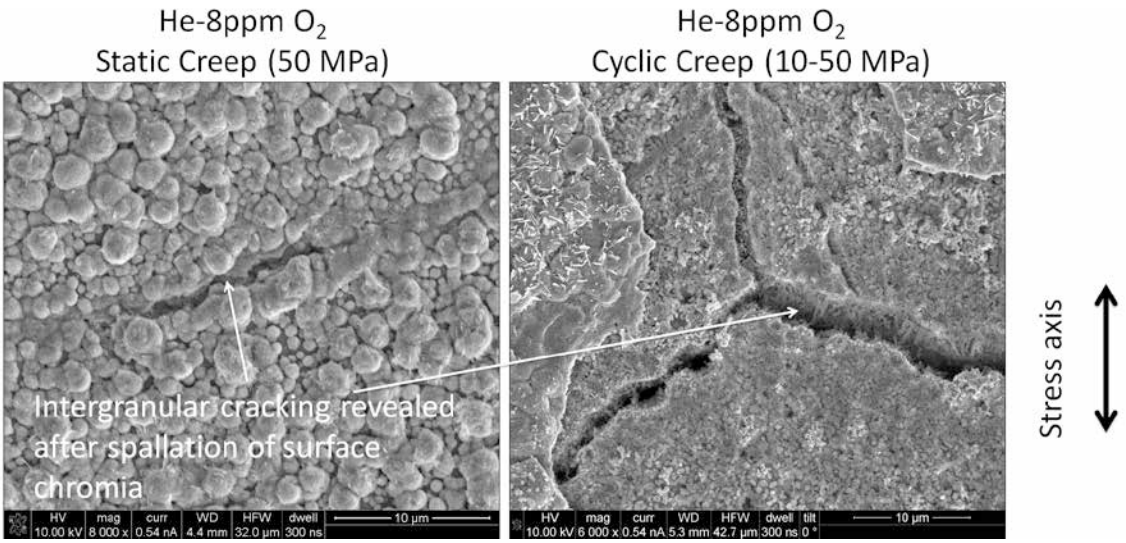

Figure 4.7 - SEM images showing surface damage of Alloy 617 crept at 800°C in He-8ppm O_2.

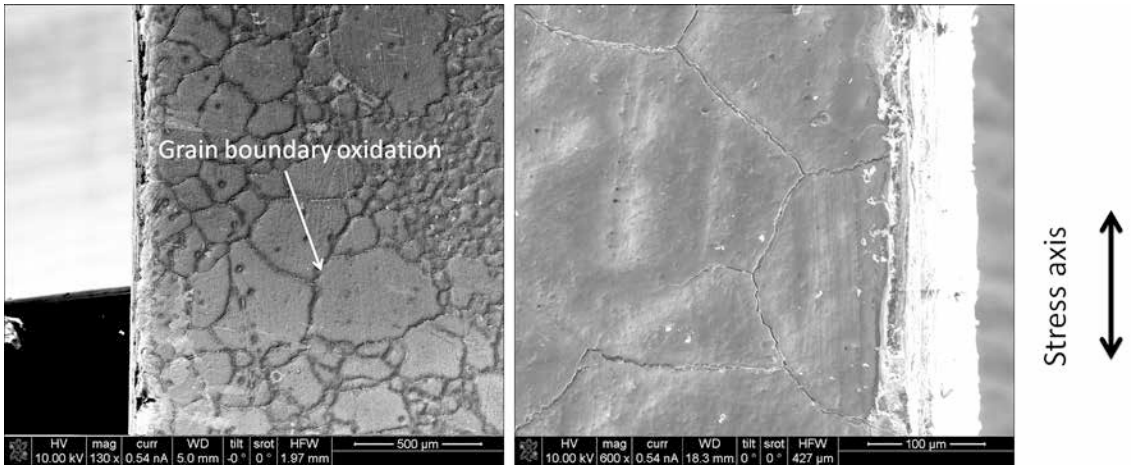

Figure 4.8 - SEM images showing surface damage of Alloy 617 crept at 800°C in He-CO/CO_2=1320.

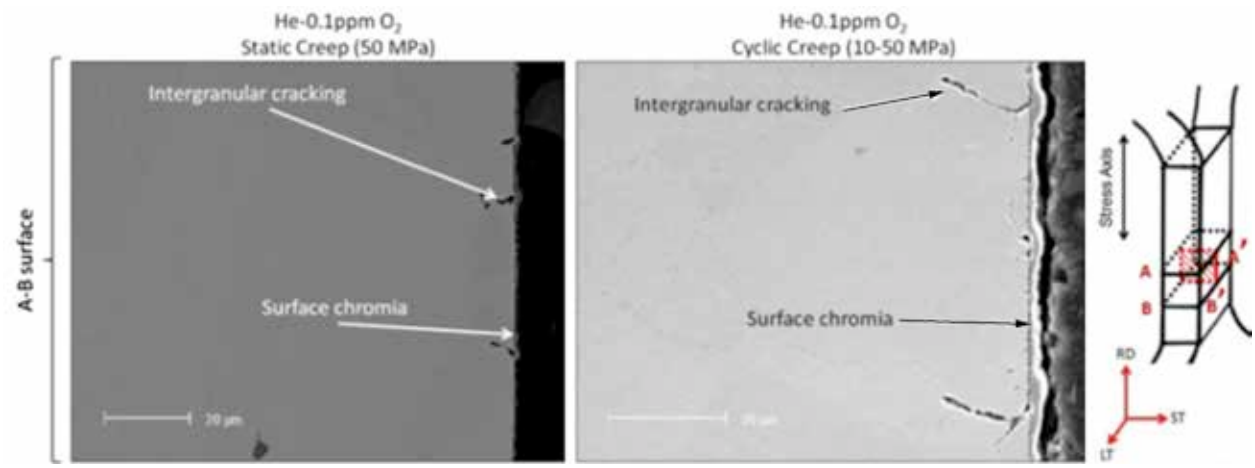

Figure 4.9 - SEM images showing characterization of internal damage of Alloy 617 crept at 800°C in He--<0.1ppm O_2.

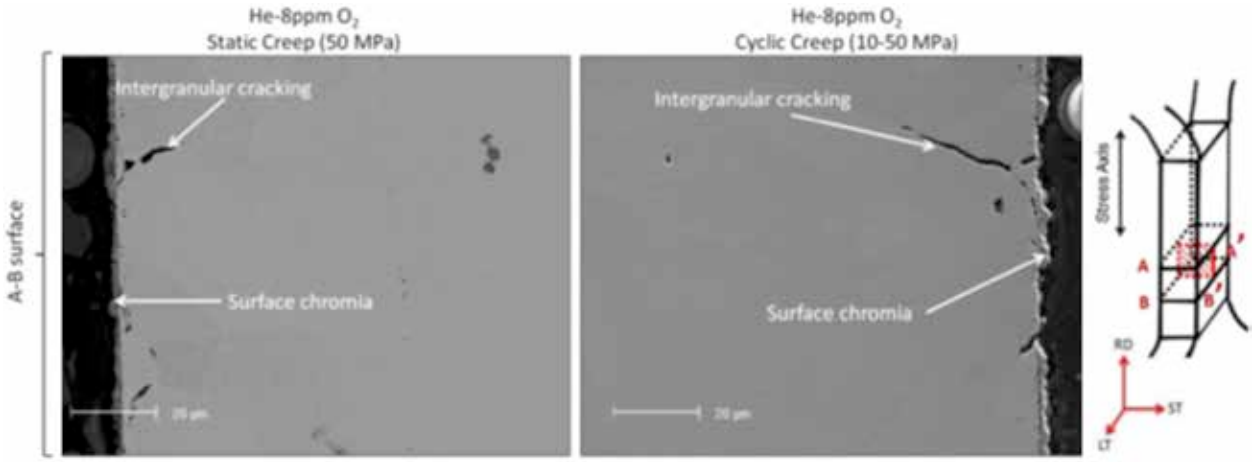

Figure 4.10 - SEM images showing characterization of internal damage of Alloy 617 crept at 800°C in He 8ppm O_2.

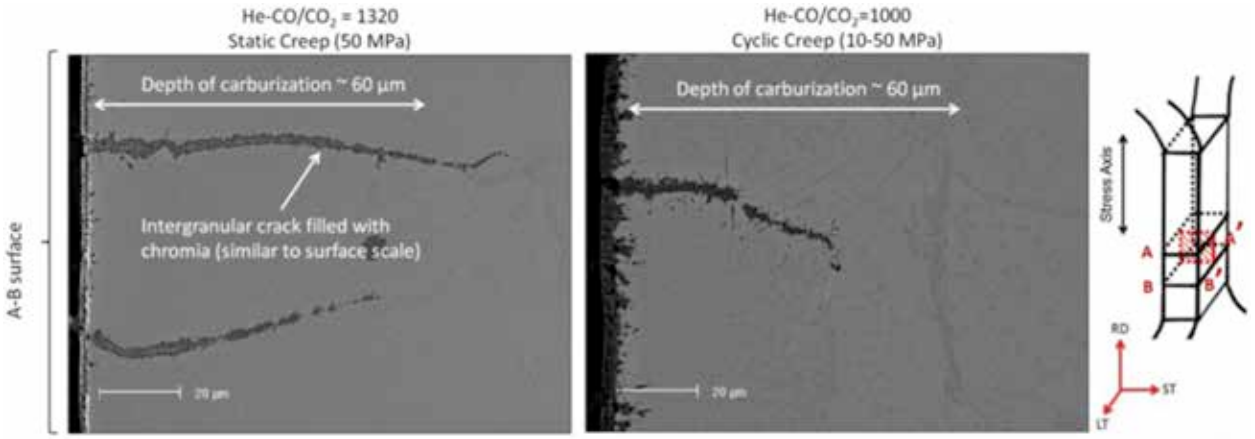

Figure 4.11 - SEM images showing characterization of internal damage of Alloy 617 crept at 800°C in He-CO/CO_2=1320.

Table 4.2 - Characterization of surface cracks in uncoated 617 crept at 800°C in different impure helium environments.

Environment	Load	Strain (%)	Number of cracks	Average crack depth (µm)	Average oxide thickness (µm)
He - <0.1ppm O_2	Static (50 MPa)	1.9	6	7.5 ± 2.4	1.0 ± 0.3
	Cyclic (10-50 MPa)	2.3	34	13.8 ± 6.4	1.3 ± 0.3
He - 8ppm O_2	Static (50 MPa)	2.2	22	13.4 ± 5.3	1.1 ± 0.4
	Cyclic (10-50 MPa)	2.4	41	13.6 ± 6.2	1.5 ± 0.4
He–CO/ CO_2=1320	Static (50 MPa)	1.7	31	34.3 ± 21.9	2.0 ± 0.4
He–CO/ CO_2=1000	Cyclic (10-50 MPa)	2.1	45	48.9 ± 14.1	3.5 ± 0.4

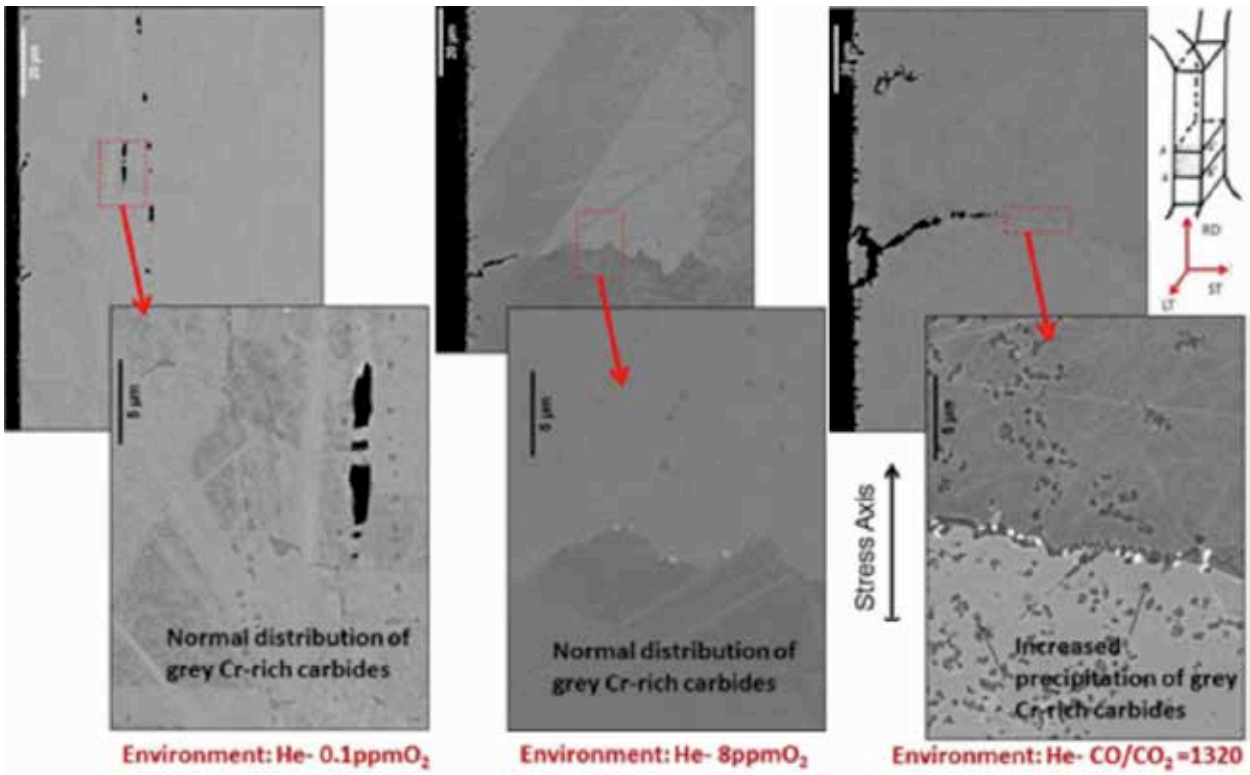

Figure 4.12 - High magnification of SEM images of Alloy 617 statically crept at 50 MPa/800°C in three different environments. Note the precipitation of internal carbides in the He-CO/CO_2=1320 environment.

The presence of chromia in the cracks is not fully understood but has been reported previously in the literature. According to Schnaas and Grabke[9], the microstructure evolution of Ni-Cr-Fe alloys in a carburizing and oxidizing environment depends on the strain rate. In the case of low strain rate (4 x 10^{-9}/s), carburization occurred along the grain boundaries, followed by oxidation and then the opening of cracks. They argued that, in the case of high strain rates (1.3 x 10^{-7}/s), carburization was not localized at the grain boundaries but carbide formation occurred throughout the bulk. In the present experiments, creep tests were terminated well before failure, making it difficult to compare directly with Grabke's work. However, it is worth noting that the strain

[9] A. Schnaas and H. J. Grabke, "High-temperature corrosion and creep of Ni-Cr-Fe alloys in carburizing and oxidizing environments," *Oxid. Met.*, vol. 12, no. 5, pp. 387–404, Oct. 1978.

rates in this study (10^{-8}/s) are between the low and high values given in the literature but carburization of the bulk was observed only up to a depth of 60μm. The grain boundaries, on the other hand, seemed to have been oxidized following an initial carburization. Given the rapid damage on the grain boundaries observed in these tests at these low strains, it is possible that in a longer test, the intergranular cracks would penetrate deeper into the specimen. In this way, further bulk carburization could be enhanced by way of grain boundary diffusion into the bulk than by bulk carburization occurring from the surface of the specimen. Also, with a longer test, the effect of the different environments in terms of the nature of the creep curves could start to become clearer than it is in the case of the interrupted tests.

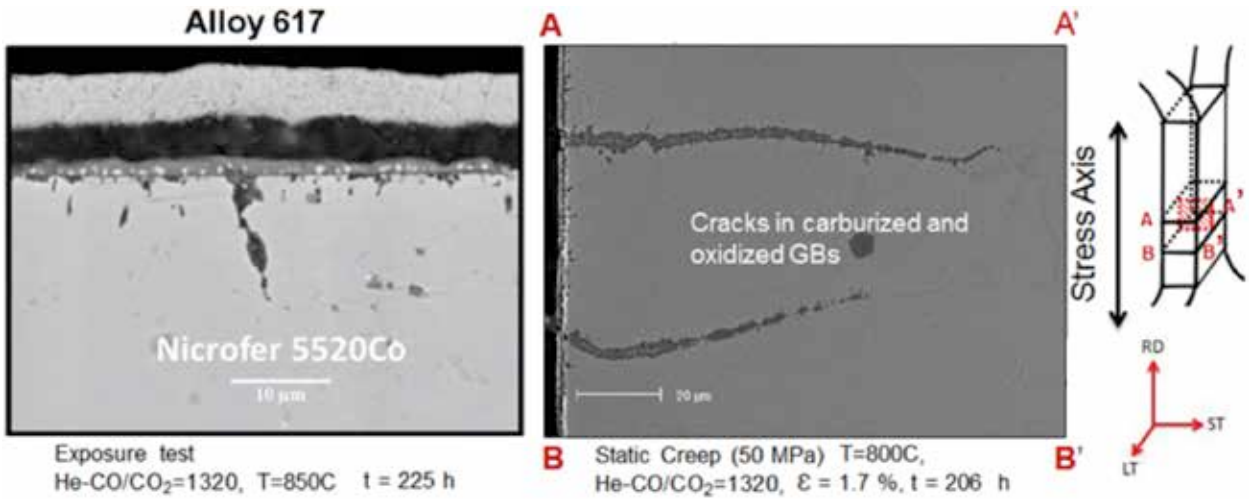

Figure 4.13 - Effect of stress/strain during exposure of Alloy 617 only exposed (left) and both crept and exposed to He-CO/CO_2=1320.

The role of stress can be seen in the comparison made between the thermally exposed and crept alloys. The experimental details of the exposed alloy were described earlier.[5] Figure 4.13 shows the difference in the nature of surface degradation in the two cases. In the exposed-only alloy (test conducted at 850°C), the usual presence of the surface chromia and intergranular and/or transgranular oxidation can be noted. The addition of stress, however, enhances the development of intergranular cracks as seen in the crept alloy (800°C test). This comparison, even though made for tests at different temperatures, still shows that the effect of creep load on Alloy 617 was much more damaging even at a relatively lower temperature. Mino[10] has described the role of stress on the intergranular oxidation of Alloy 617. He observed that the applied stress significantly enhanced the intergranular oxidation and also that the penetration depth increased with creep strain and oxidation time. It is surmised that the enhanced intergranular oxidation (and consequently intergranular cracking) was attributed to the localized fracture of external oxide layers and internal oxides of aluminum due to grain boundary sliding.

While the role of stress was evident when comparing loaded versus unloaded specimens, the type of loading (cyclic or static) also seemed to play a role in the extent of surface degradation of Alloy 617. A general conclusion from Table 4.2 on the effect of the type of loading is that cyclic loading caused more severe damage (higher number of cracks, increased cracks depths and in-

[10] K. Mino, A. Oktomo, and Y. Saiga, "The effect of stressing on the intergranular oxidation of Inconel 617," *J. Japan Inst. Met.*, vol. 44, no. 12, pp. 1397–1403, 1980.

creased scale thickness) than static loading possibly as a result of oxide fracture during the cyclic opening and closing of cracks. However, it should also be noted that the cyclic loading was such that during each cycle, the alloy was subjected to the maximum stress half of the time compared to the case of static stress. So, it took twice as long to reach the target strains as it did for static tests. Since creep and oxidation are both time dependent mechanisms, it is not clear if the longer time of exposure or the nature of the loading could have been responsible for the relatively severe damage. Future tests could be proposed where the loading and unloading transients of the loading cycle are reduced so that the total test time tends towards the total time at maximum stress. In this way, a more meaningful comparison between static and cyclic creep tests could be made.

4.3. Coating concepts exhibit mechanically robust protective layers in impure He.

The investigation creep behaviors of the coating concepts proposed in this project re compared with that of uncoated 617 in Figure 4.14 and Table 4.3. The goal was to understand the effect of creep deformation on the microstructural and mechanical integrity of the three different coating architectures, namely NiAl/617, FeCrAlY/617, and NiAl/FeCrAlY/617.

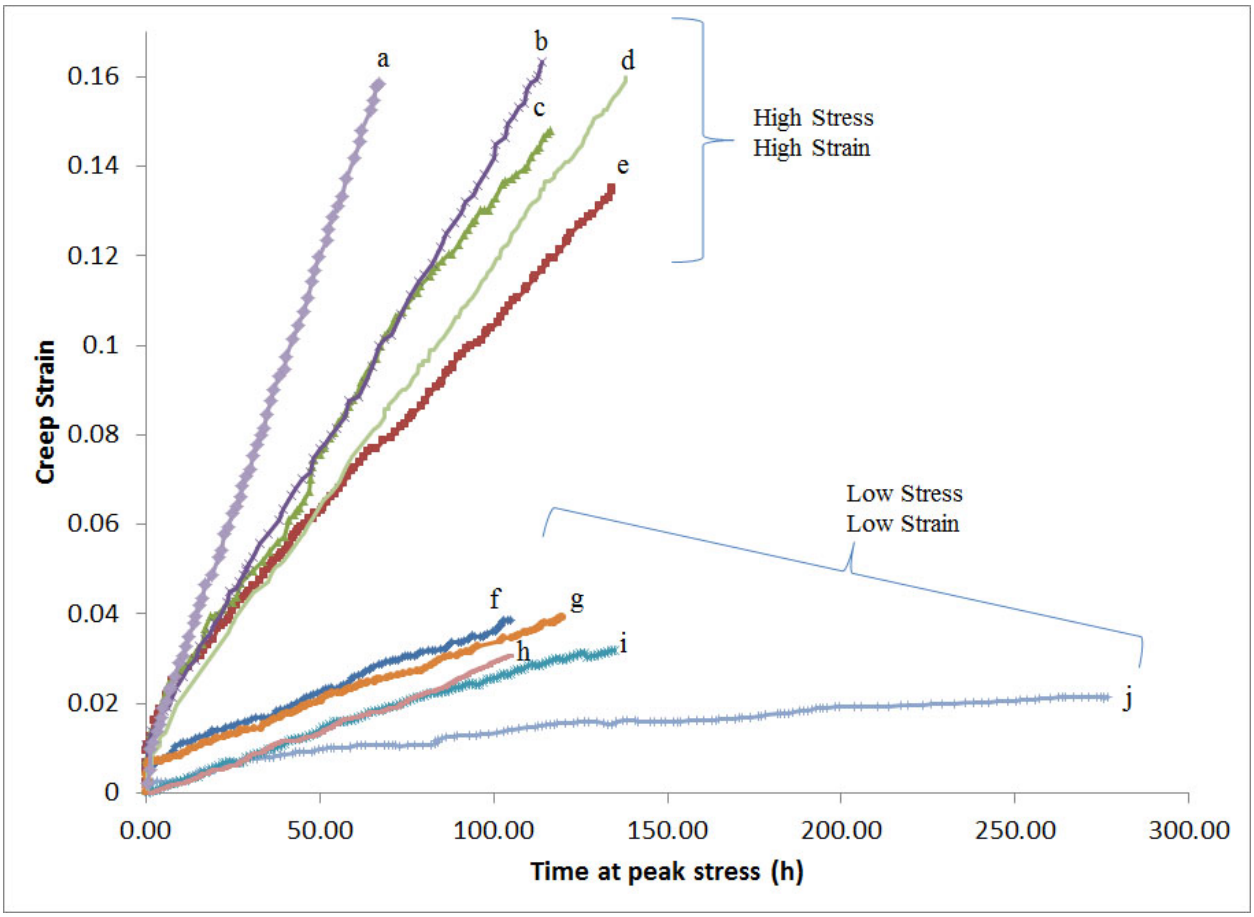

Figure 4.14 - Interrupted creep of uncoated 617, aluminized 617, clad-only 617 and clad-aluminized 617 tested at 800°C in different He environments.

Table 4.3 - Interrupted creep of different 617 based specimens tested at 800°C in impure He.

Curve	Specimen	Creep Test (S=static, C=cyclic)	Impure He Environment	Strain (%)	SS Creep Rate (10^{-8}/s)	Total time (h)	Cycles
a	Alum+Clad	S (75 MPa)	<0.1ppm O_2	16	62	109	N/A
b	Alum+Clad	C (15-75 MPa)	CO/CO_2=1320	16	36	140	3358
c	Aluminized	C (15-75 MPa)	CO/CO_2=1320	16	35	120	2871
d	Aluminized	S (75 MPa)	CO/CO_2=1320	15	30	139	N/A
e	Clad	C (15-75 MPa)	CO/CO_2=1320	14	24	167	3992
f	Alum+Clad	C (10-50 MPa)	CO/CO_2=1320	4	8	213	3191
g	Alum+Clad	S (50 MPa)	CO/CO_2=1320	4	8	120	N/A
h	Aluminized	S (50 MPa)	8ppm O_2	3	4	215	N/A
i	Aluminized	C (10-50 MPa)	8ppm O_2	3	3	513	7691
j	Uncoated	C (10-50 MPa)	CO/CO_2=1320	2	1	553	8294

One desirable property of an effective coating layer is that its composition remains sufficiently stable during service to remain adherent and enable the regeneration of the alumina scale if it is disrupted by cracking or spallation. Interdiffusion studies in this project,[11] described in various quarterly reports under Task 2, provide a baseline for the behavior in the absence of stress. An appropriate comparison is provided by the Gen I aluminized-only specimens in Figure 4.15 and 4.16. In the absence of applied load, The multilayer structure developed by the 8 h heat treatment at 1000°C after aluminizing does not appear to evolve significantly upon subsequent exposure at 800°C for 500 h (Figure 4.15). No evidence was observed that the interdiffusion behavior was affected by the application of cyclic or static loads at the same temperature, Figure 4.16. Similar behavior was observed in aluminized as well as aluminized+clad specimens crept in different environments under static and cyclic stresses (Figures 4.17 and 4.18). It was therefore concluded that stress does not compromise the compositional integrity of the NiAl and FeCrAlY coating layers at 800°C. This observation confirms what had been reported earlier concerning the coating layers playing an excellent role in acting as effective diffusion barriers during creep at 800°C. The imposed strains do not appear to induce any noticeable damage in these diffusion barrier layers, which are expected to be brittle based on their carbide and sigma phase constituents. It is hypothesized that this is due, at least in part, to the interpenetration of these brittle layers by the metallic component.

It has been reported elsewhere that properly designed coatings do not affect the creep behavior of the underlying substrates and that their load-bearing capability can be ignored.[12] It can, therefore, be inferred that the higher creep rates observed in this project for the coated specimens relative to their uncoated counterparts may be ascribed in part to the higher loads applied during the experiments, and perhaps to microstructural changes in the substrate introduced during the coating application.

[11] E.A. Clark, "Surface Engineering of Nickel Alloys to Form a Stable Alpha Alumina Barrier Layer at T≤1000°C," Doctoral Dissertation in Materials, University of California, Santa Barbara (2013).

[12] Y. Itoh, M. Saitoh, and Y. Ishiwata, "Influence of high-temperature protective coatings on the mechanical properties of nickel-based superalloys," *J. Mater. Sci.*, vol. 34, no. 16, pp. 3957–3966, 1999.

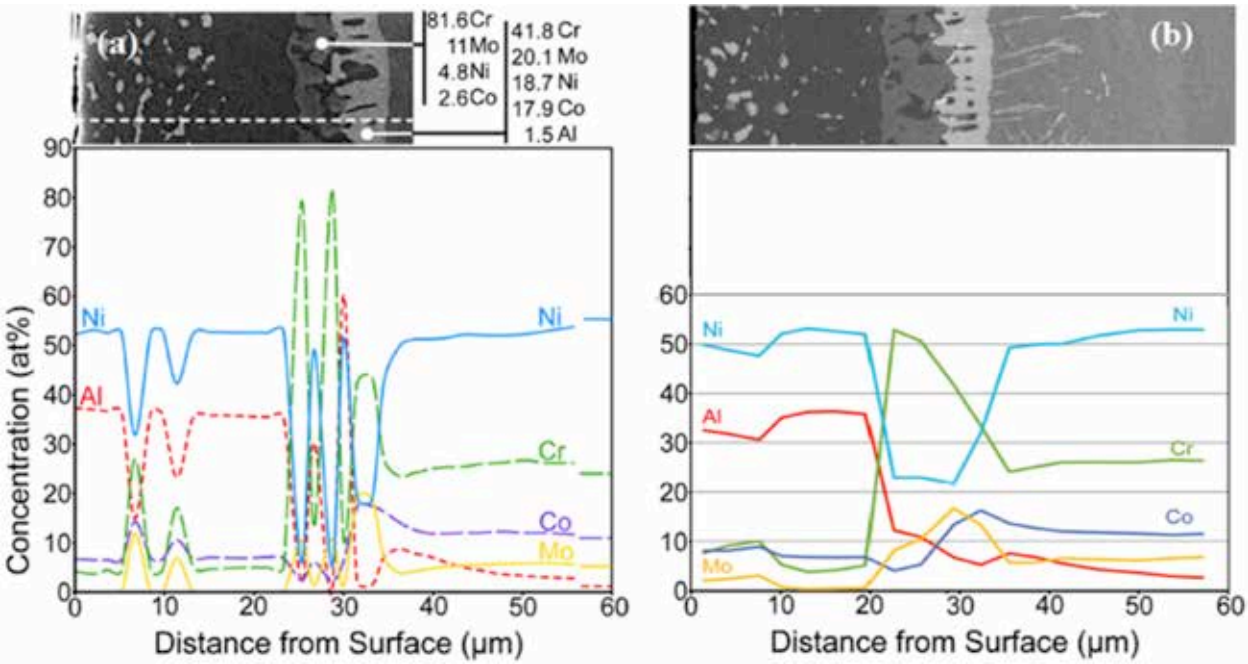

Figure 4.15 - EDS concentration profiles of Gen I aluminized 617 showing the effect of ageing on compositional evolution. (a) shows the as-received 617 aluminized at 700°C/9.6h and heat treated at 1000°/18h, and (b) shows aluminized 617 exposed to a decarburizing environment at 800°C/500h.

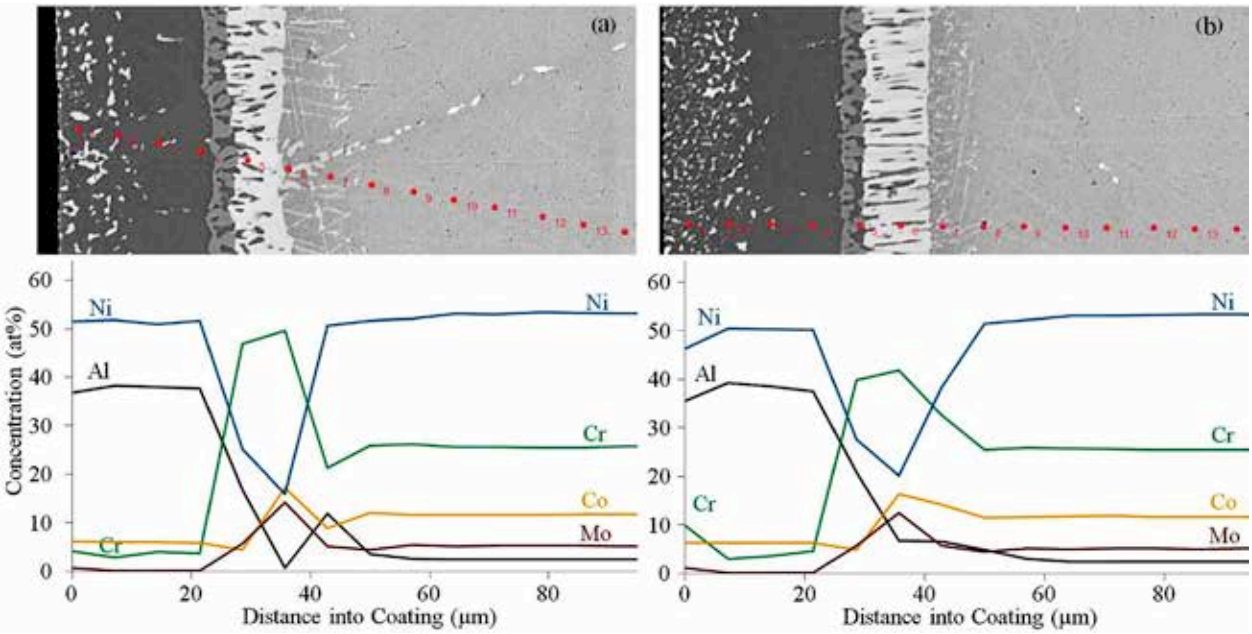

Figure 4.16 - EMPA concentration profiles of Gen I aluminized 617 after (a) cyclic creep (10-50 MPa) and (b) static creep (50 MPa). Comparison with the effects of aging in Figure 4.15 reveals that deformation does not influence the diffusion measurably.

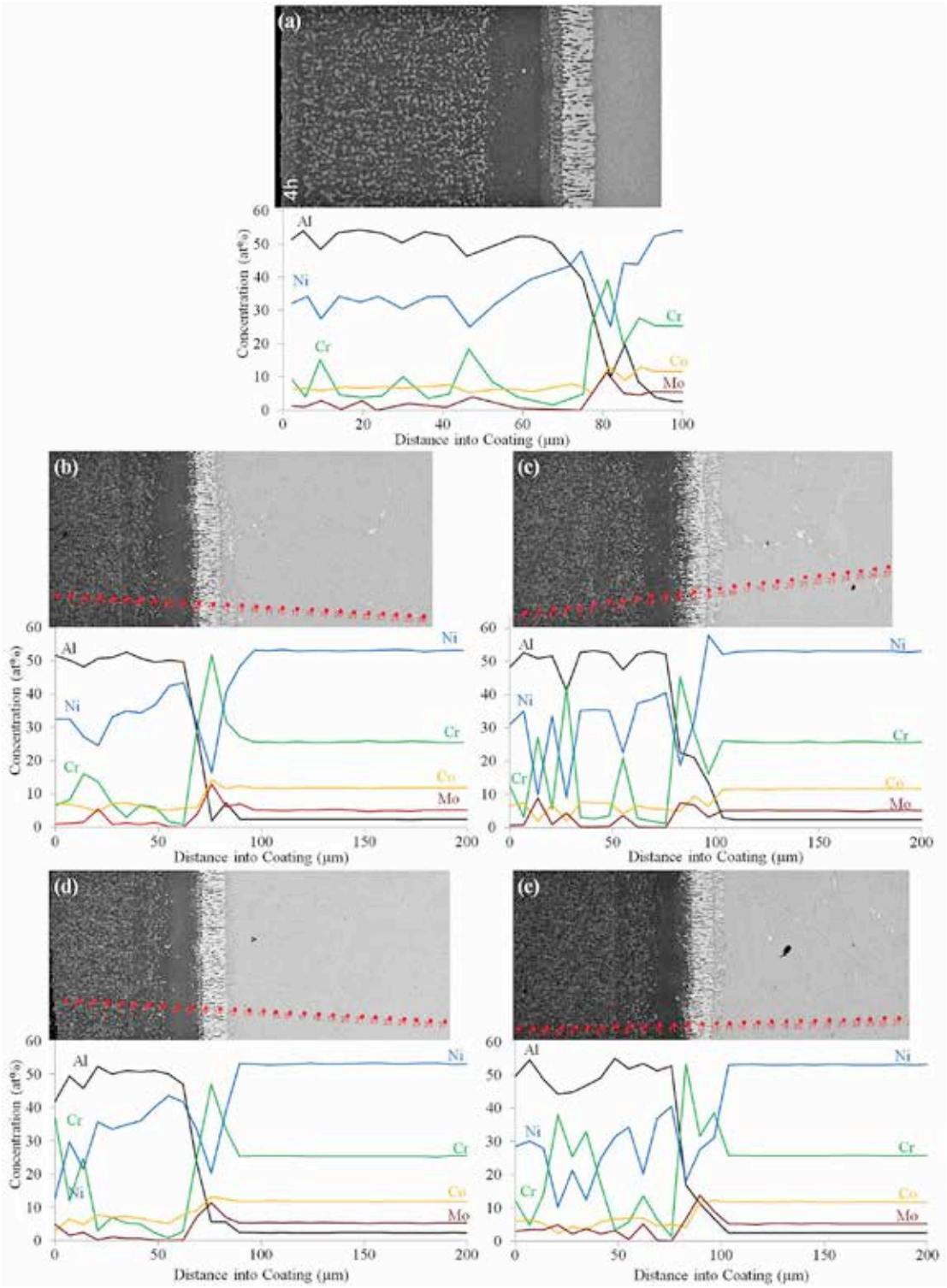

Figure 4.17 - EMPA concentration profiles of Gen II aluminized 617 specimens evaluating the effect of creep deformation at 800°C on compositional evolution. The profiles shown are for: (a) as-received material after a heat treatment of 1000°C/4h; (b) static creep 50 MPa/212 h/ε=4%; (c) static creep 60 MPa/286 h/ε=10%; (d) static creep 75 MPa/139h/ε=15%; and (e) cyclic creep at 15-75 MPa/120h/ ε=16%. Neither static nor cyclic creep appear to influence the diffusion behavior measurably. The fluctuations in the Cr levels are attributed to the presence of precipitates along the profile scan line.

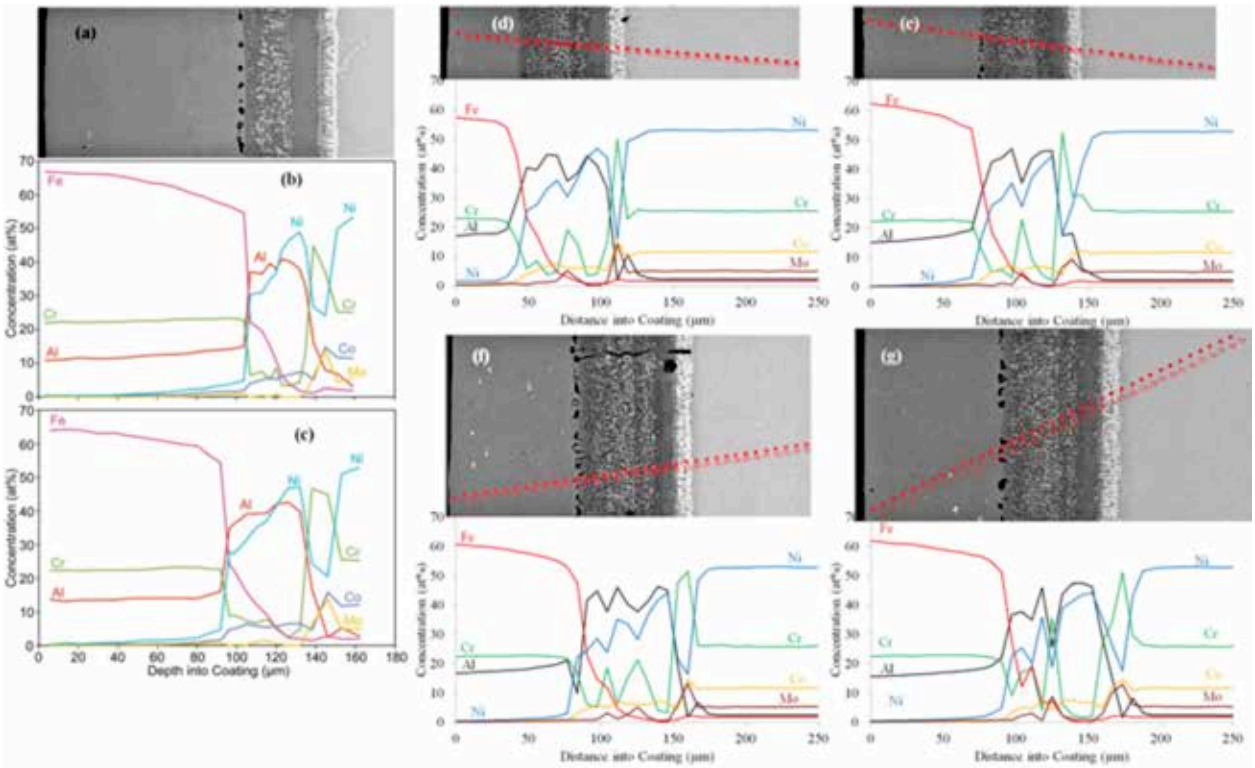

Figure 4.18 - EMPA concentration profiles Gen II FeCrAlY/NiAl/617 exploring the potential effect of creep deformation at 800°C on compositional evolution. The profiles shown are for: (b) as-received specimen subjected to a heat treatment of 1000°C/4 h and clad at 1000°C/2 h; (a, c) after 800°C/100 h exposure without load; (d) cyclic creep at 15-75 MPa/117 h/ε=17%; (e) static creep at 75 MPa/109 h/ ε=16%; (f) static creep at 50 MPa/120 h/ε=4%; and (g) cyclic creep at 10-50 MPa/213 h/ε=4%. Again, there is no detectable evidence of an effect of the applied stress on the interdiffusion behavior.

Even though creep deformation does not have an effect on the compositional evolution of the coating/substrate systems, the mechanical integrity of the coatings is dependent on the coating system. First, both Gen I and II NiAl/617 specimens revealed no cracks through the coating layer but only on the very thin alumina scale at the NiAl surface (Figure 4.19). Second, the cladding layer in the FeCrAlY/617 did not crack, but was characterized by grain boundary sliding and grain uplifts (Figure 4.20). Interestingly, when the cladding layer is introduced over the NiAl layer cracks were found to evolve in the NiAl layer during cyclic creep, but did not propagate into either the substrate or into the cladding at low stress (Figure 4.21). This behavior requires further investigation to identify the possible mechanisms involved.

An explanation for the cracking behavior in the NiAl layer when clad with FeCrAlY has proven elusive, especially regarding the non-clad sides of the creep specimens, which also crack. One might hypothesize that the observed behavior results from the cladding process altering the mechanical behavior of the NiAl. However, the composition and microstructure of the NiAl layer do not seem to be substantially affected by the cladding (cf. Figures 4.17 and 4.18). The absence of cracks in the interdiffusion zone and in the coating layer in NiAl/617 implies the two materials are reasonably compatible mechanically. Thermal stresses arising from the difference in thermal expansion coefficients (Figure 4.22) below the ductile-brittle transition for NiAl may be present but do not appear to be sufficient to trigger cladding.

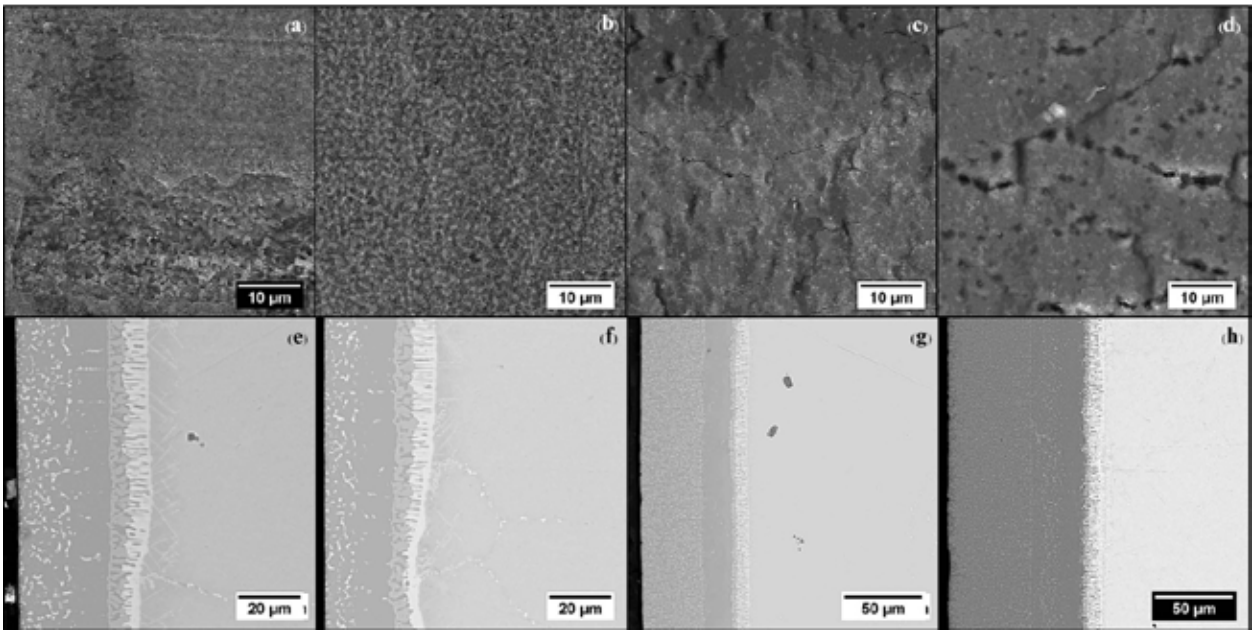

Figure 4.19 - SEM images showing damage on the surface (a-d), and cross-sectional views (e-h) of NiAl/617 specimens after crrep in impure He. The stress/strain conditions were (a,e) 10-50 MPa/3%, (b,f) 50 MPa/3%, (c,g) 75 MPa/15%, and (d,h) 15-75 MPa/16%. Note that irrespective of stress/strain the NiAl layer maintains its mechanical integrity under low and high stress/strains conditions.

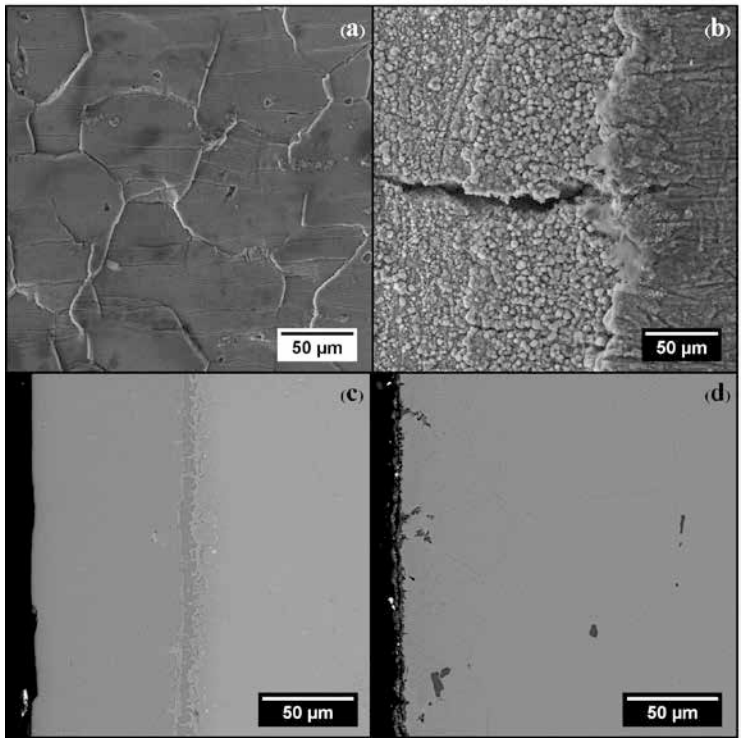

Figure 4.20 - SEM images of FeCrAlY/617 specimens showing damage on the (a) wider surface that is clad, and (b), the narrower surface that is bare 617(b), as well as cross sectional views (c) parallel to the narrower surface (c), and (d) parallel to the wider surface. The wider surface shows grain uplifts in the cladding whereas the narrower surface shows environmental attack in the exposed 617. The stress/strain conditions were 15-75 MPa/14% in a carburizing environment (He-CO/CO_2=1320).

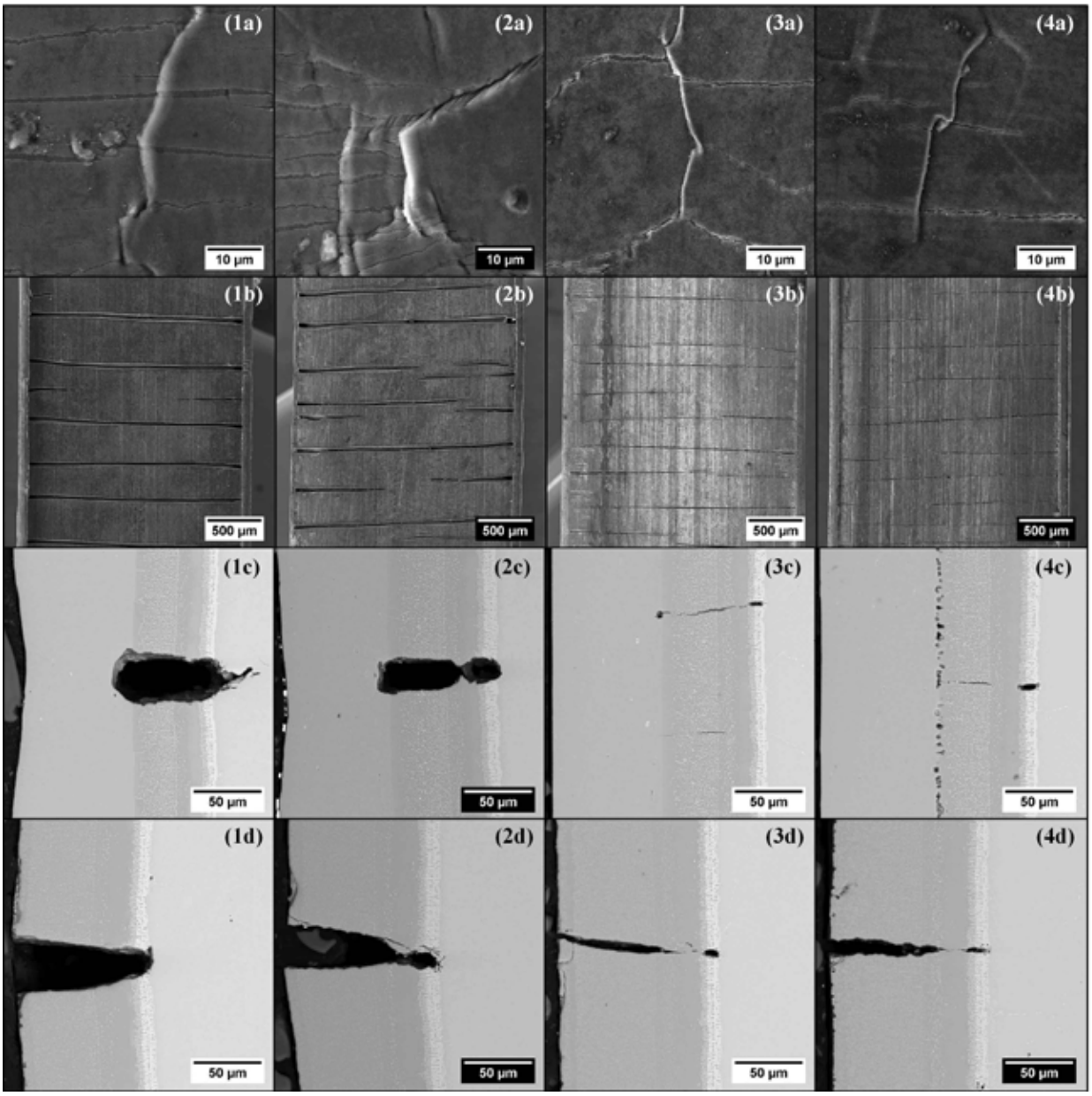

Figure 4.21 - SEM images of crept FeCrAlY/NiAl/617 specimens showing damage on (a) the wider surface that is aluminized and clad, (b) narrower surface that is aluminized only, with accompanying cross-sectional views (c) parallel to the narrower surface, (d) parallel to the wider surface. The wider surface shows grain uplifts in the cladding whereas the narrower surface shows cracks in the aluminized-only layer. The stress/strain conditions were (1) static creep at 75 MPa/ε=16%, (2) cyclic creep at 15-75 MPa/ε=16%, (3) static creep at 50 MPa/ε=4%, and (4) cyclic creep at 10-50 MPa/4%. (a) is in He-<0.1ppmO_2 and (b-d) He+CO/CO_2=1320. Note difference in void opening between the high (1,2) and low (3,4) applied strains. In most cases the damage is limited to the NiAl layer and does not bridge the cladding or propagate significantly into the substrate, except for the image in 1(c).

Examination of the CTE values in Figure 4.22 suggests that if the system were stress-free after removing the pressure at the 1000°C cladding temperature, the FeCrAlY should be in compression on cooling and some residual compression should remain when reheated to the creep temperature of 800°C. The implication is that if the CTE mismatch between NiAl and 617 were to

produce sufficiently high tensile stresses that can add to the imposed mechanical stress to induce cracking in the clad condition, it should also result in cracking in the absence of cladding. Further work, including relevant modeling, would be necessary to improve the analysis of the difference in stresses between the aluminized 617 with and without cladding.

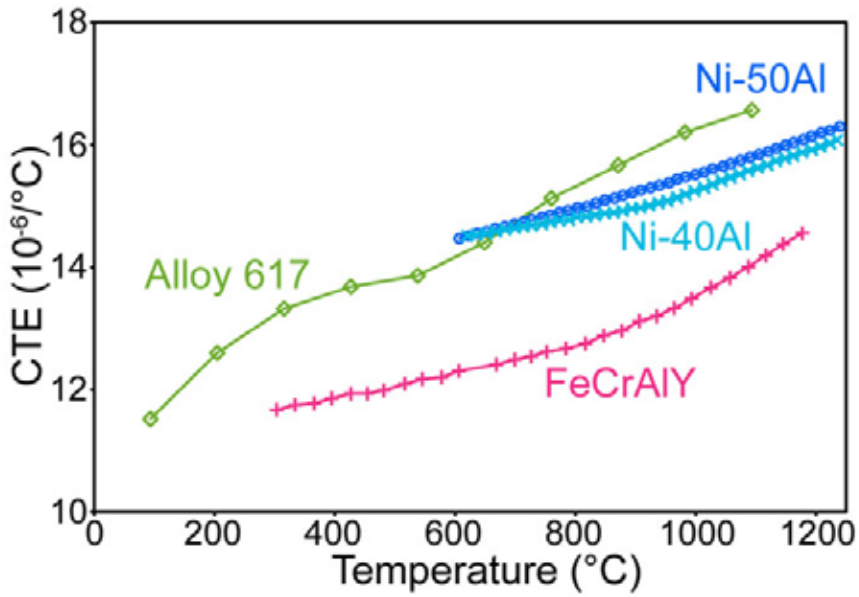

Figure 4.22 - Coefficients of thermal expansion (CTE) for alloy 617, NiAl, and FeCrAlY. [13]

One may also consider that cracks in the NiAl layer initiate from the pores that form at the FeCrAlY/NiAl interface during the cladding process or during post cladding heat treatment. Low and high stress/strain creep deformation studies of the FeCrAlY/NiAl/617 coating system suggest this is not a likely scenario. At high strains, e.g. Figure 4.21(1c), some of the large cracks within the NiAl extend past the diffusion barrier layers into the 617 substrate, but do not bridge the ductile FeCrAlY layer, even if they may have been initiated at the interfacial pores. At low strains, more representative of the service conditions, the cracks were not connected to the interfacial pores and were localized in the precipitate-rich region of NiAl, e.g. Figure 4.21(4c).

This raises the possibility that the crack initiation may be associated with the precipitate-rich region of the NiAl layer. Figure 4.23 shows an EBSD scan of the region close to the void formed in the NiAl under high stress/strain. It is noteworthy that the grains in the ductile 617 and FeCrAlY are larger than the grains in the NiAl layer and, thus, a combination of shift in mechanical behavior of the NiAl layer, especially in the precipitate-rich region, and heterogeneous deformation in the coarse-grained FeCrAlY layer may play a role in the formation of cracks (Figure 4.24). Microstructure and mechanics analyses are continuing in an attempt to identify the likely mechanisms responsible for this behavior.

4.4. Cyclic creep of notched NiAl-617

As described in section 4.3, the NiAl layer in the NiAl/617 system was resistant to crack formation during creep in impure He environments. To further examine the mechanical behavior of the NiAl layer, FIB notches were introduced in the NiAl layer of an aluminized-only 617 (NiAl/617), to examine if damage would progress during creep from pre-existing defects.

[13] C. G. Levi, J. W. Jones, E. A. Clark, and A. O. Okello, "NEUP 10-963 Quarterly Progress Report Y4Q2," 2014

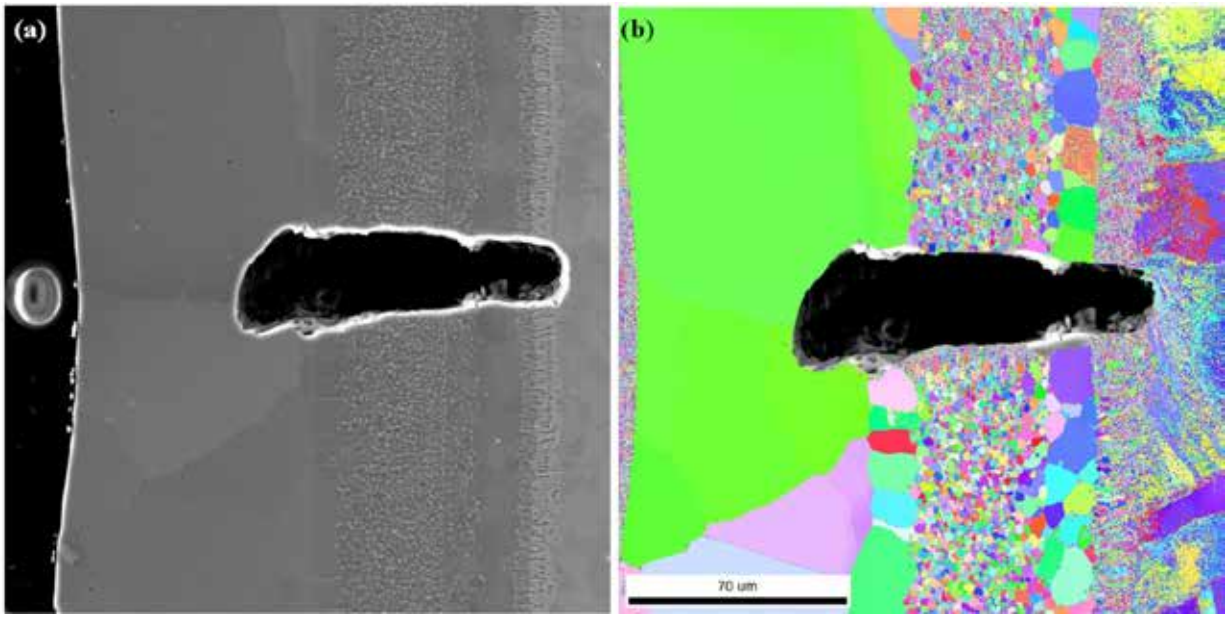

Figure 4.23 - (a) Microstructure close to a void formed after high stress/strain cyclic creep tests of the clad-aluminized 617 and (b) corresponding EBSD map. The grain size and thickness of the FeCrAlY cladding are comparable and the precipitate-rich region in NiAl has smaller grains than the surrounding areas.

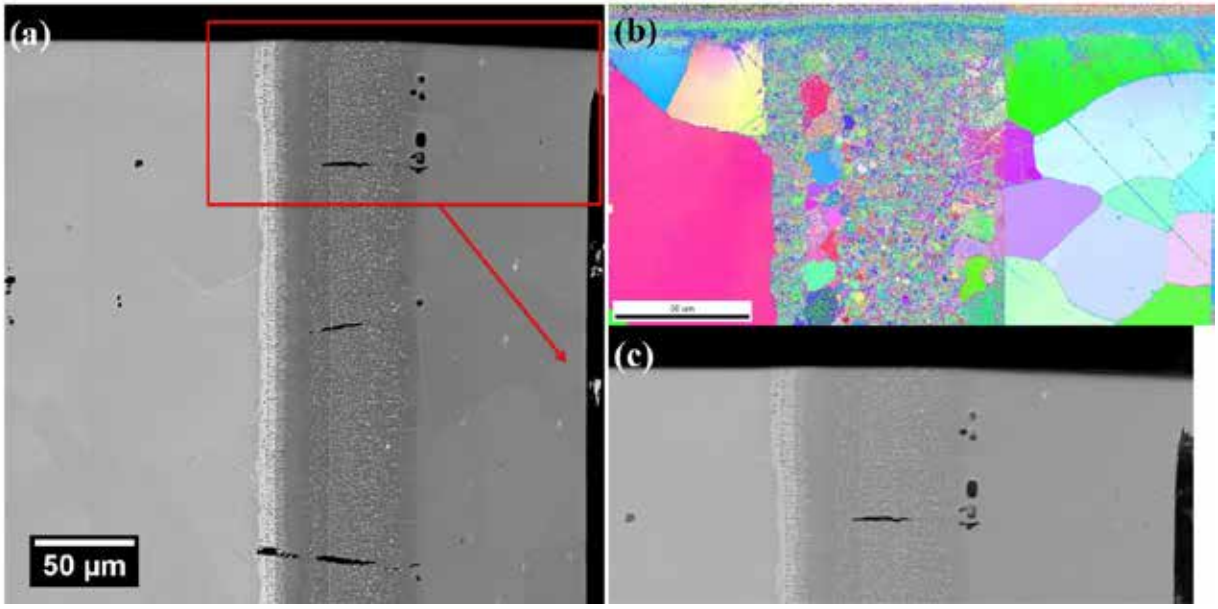

Figure 4.24 - EBSD characterization of region close to a crack that formed after low stress/strain cyclic creep tests of the clad-aluminized 617. The grain size and thickness of the FeCrAlY cladding are comparable and the precipitate-rich region in NiAl has smaller grains than the surrounding areas. The crack seems to initiate farther away from pores and in the precipitate-rich region in NiAl.

Cyclic creep experiments (10-50 MPa) at short and long durations (~200h and ~600h, respectively) at 800°C were conducted to investigate the behavior of FIB-notched aluminized specimen during creep in a carburizing/oxidizing environment as shown in Figure 4.25. The creep behavior of NiAl specimens with and without notches are shown in Figure 4.26, and the small notches do not affect the global creep behavior, as expected.

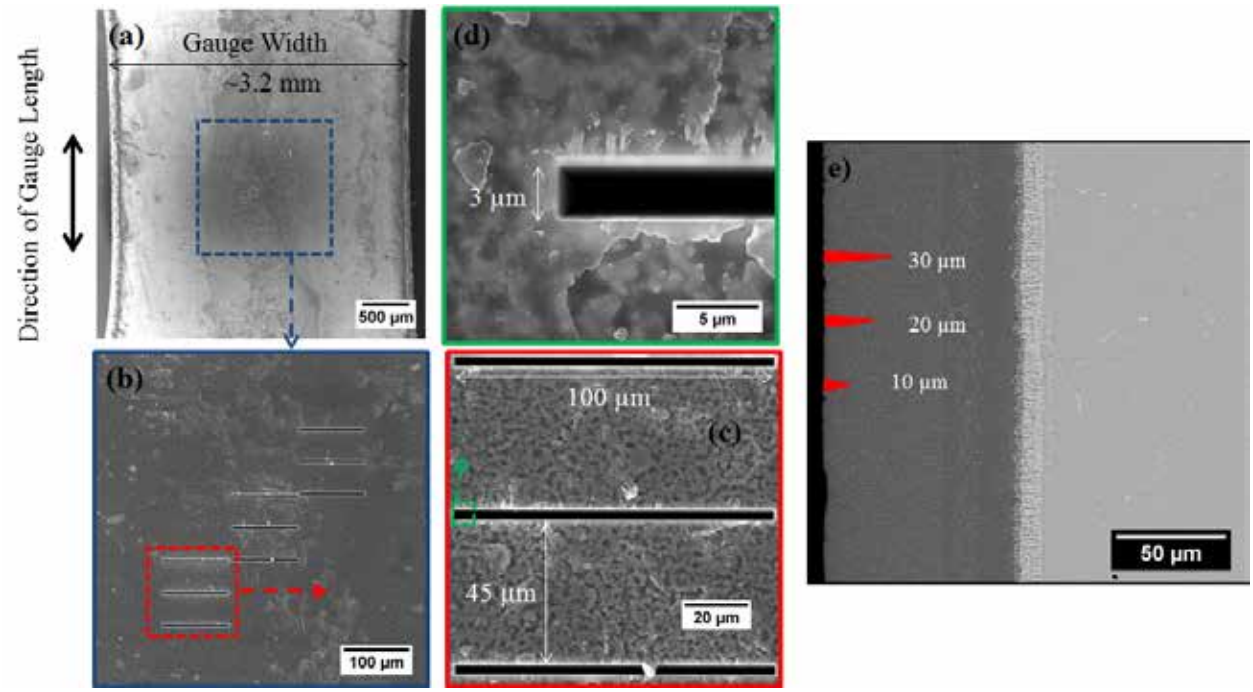

Figure 4.25 - SEM images showing FIB notches used to investigate crack propagation in the aluminized layer of Gen II NiAl/617. Three sets of implanted notches with each set having 3 different depths as schematized in (e) to provide a larger specimen area for post-experiment analysis.

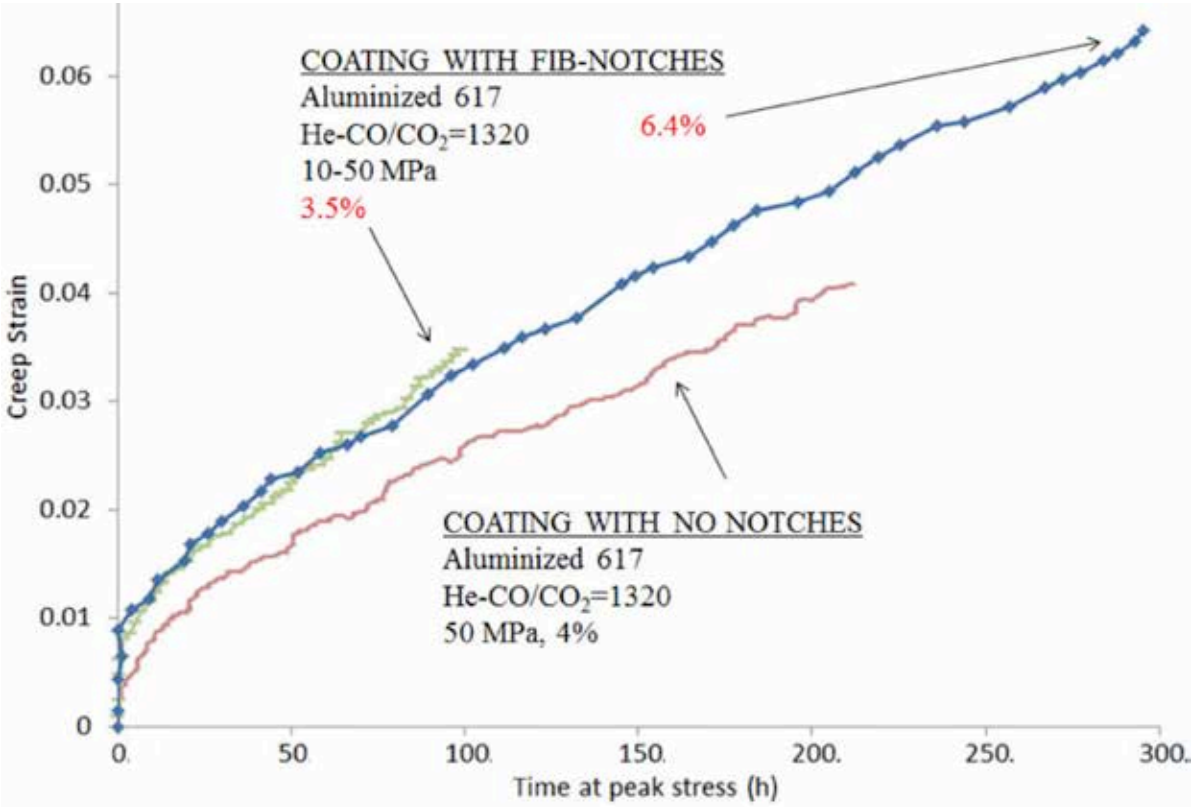

Figure 4.26 - Curves of interrupted cyclic creep of NiAl/617 with and without notches indicating that the presence of the localized notches does not affect the creep rates (slope of linear part of curve).

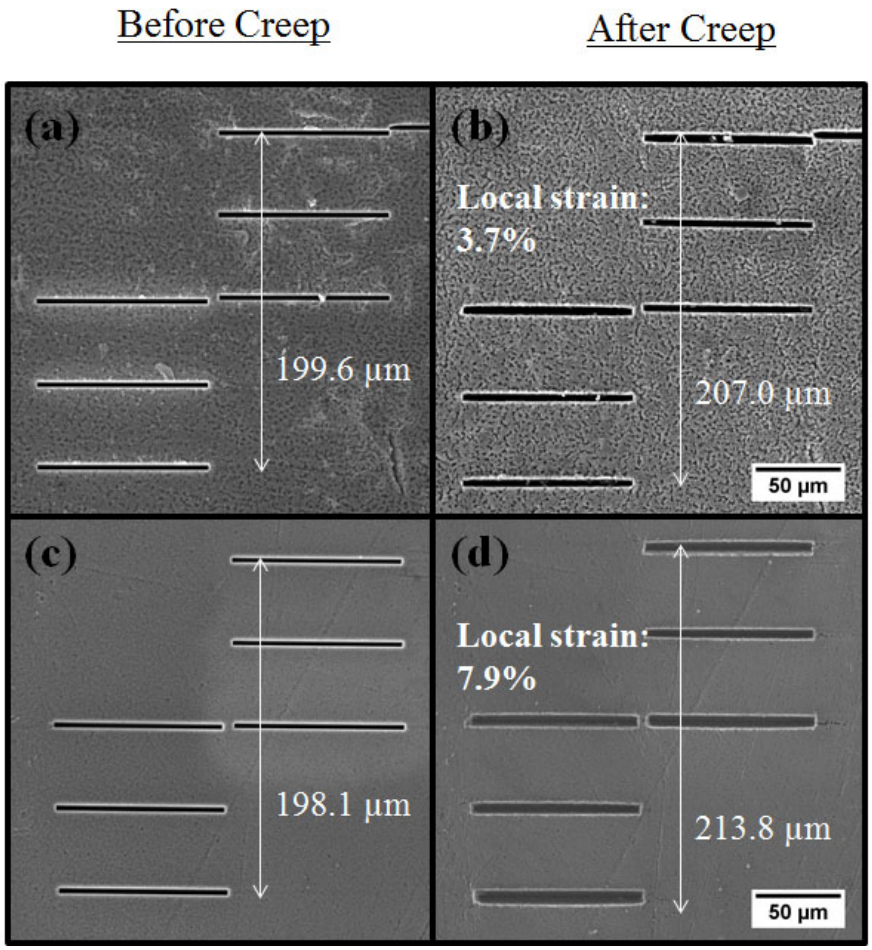

Figure 4.27 - SEM images (low magnification) showing the determination of local strain after cyclic creep (10-50 MPa) at 800°C in a carburizing environment (He-CO/CO_2=1320) and subjected to 198h/3.5% strain (a,b) and 594h/6.4% strain (c,d).

The strains local to the notched areas on the specimen are higher compared to the global strains during creep as shown in **Error! Reference source not found.** and 4.28**Error! Reference source not found.** and the shape of the notch root appears to be blunting with increasing strains Figure 4.29, while a very narrow oxide region extends from the original notches. Figure 4.30 shows the evolution of the notch tip profile during cyclic creep. At higher magnification (Figure 4.31), it is evident that the profile of the tip changes faster than the tip oxidation is propagated. At 3.5% strain and after ~200h, the oxide at the tip has already started penetrating into the coating, but does not propagate significantly further at a higher strain and longer test duration (6.4%, 600h). It could be argued that the formation of alumina at the tip/root and sides of the notch takes place upon exposure of the specimen to the carburizing environment at 800°C. The global creep deformation, however, does not seem to facilitate any further propagation of cracking at the oxidized tip. Also, further straining of the notched NiAl layer in NiAl/617 does not produces kinks in the regions immediately close to the notch root but does not translate to the extension of the oxide penetration or cracking at the notch root, although a contribution from crack healing by oxide bridging cannot be ruled out at this time. This behavior of the NiAl layer, in the presence of notches, helps to affirm the mechanical robustness of the aluminide coating as has been observed before.

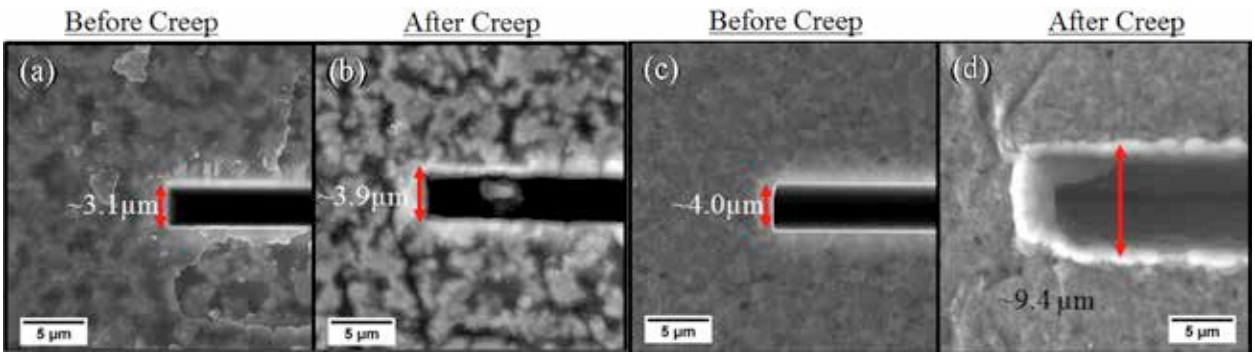

Figure 4.28 - SEM images (high magnification) showing the dimensional changes on the individual notches after cyclic creep (10-50 MPa) at 800°C in a carburizing environment (He-CO/CO_2=1320) and subjected to (a,b) 198h/3.5% strain and (c,d) 594h/6.4% strain. Note the significant dimensional change in the notch opening after higher strains (c→d compared to a→b).

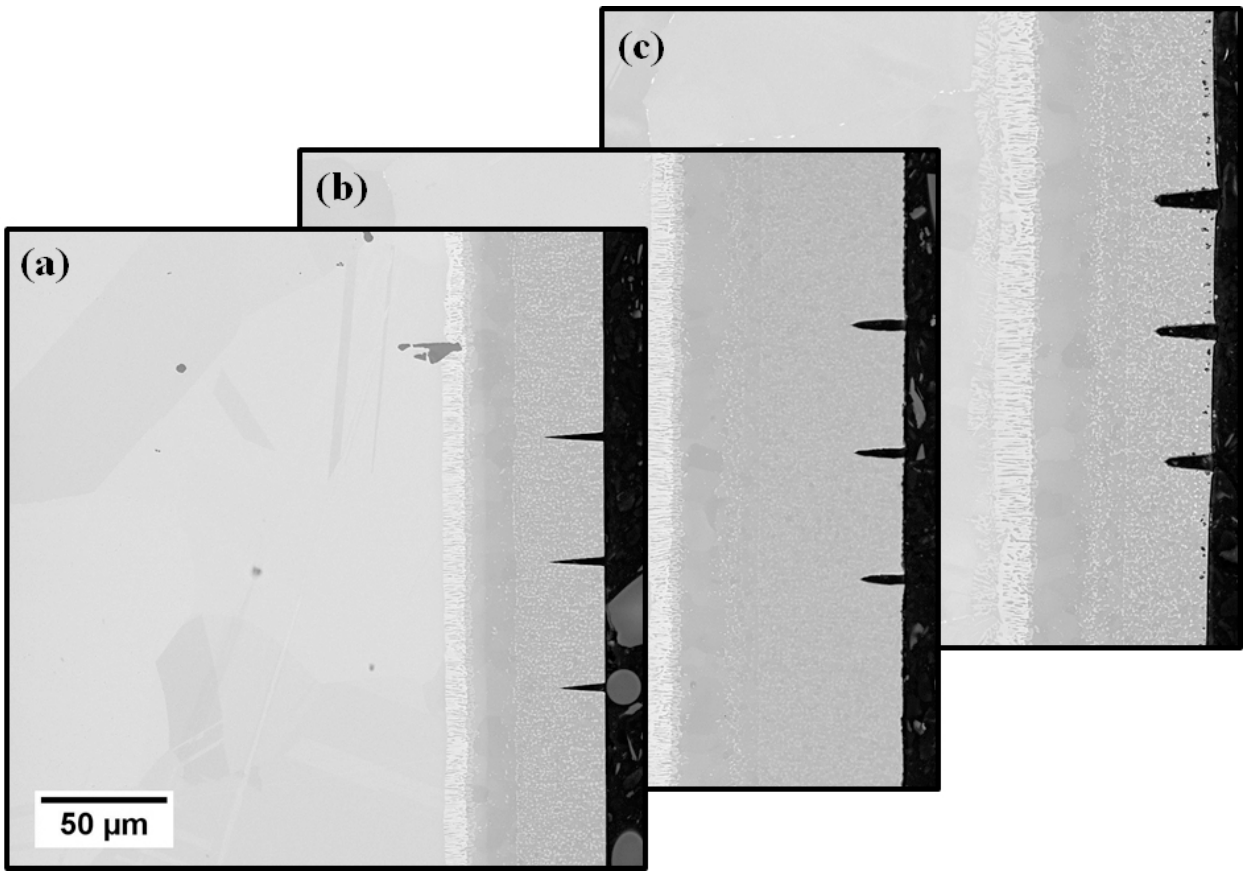

Figure 4.29 - SEM images (high magnification) showing the three notches on the untested coupon (a), and those having undergone cyclic creep (10-50 MPa) at 800°C in a carburizing environment (He-CO/CO_2=1320) and subjected to 198h/3.5% strain (b) and 594h/6.4% strain (c).

It is important to point out the difference in the appearance of the oxidation at the notch root as a function of the immediate microstructure of the NiAl layer close to the tip. It appears that the nature or progress of the oxidation front could be affected whenever the tip encounters α-Cr precipitates. A recent EDS mapping to help identify the composition of the different phases close to the oxidation tip was not conclusive and further such analyses have been planned.

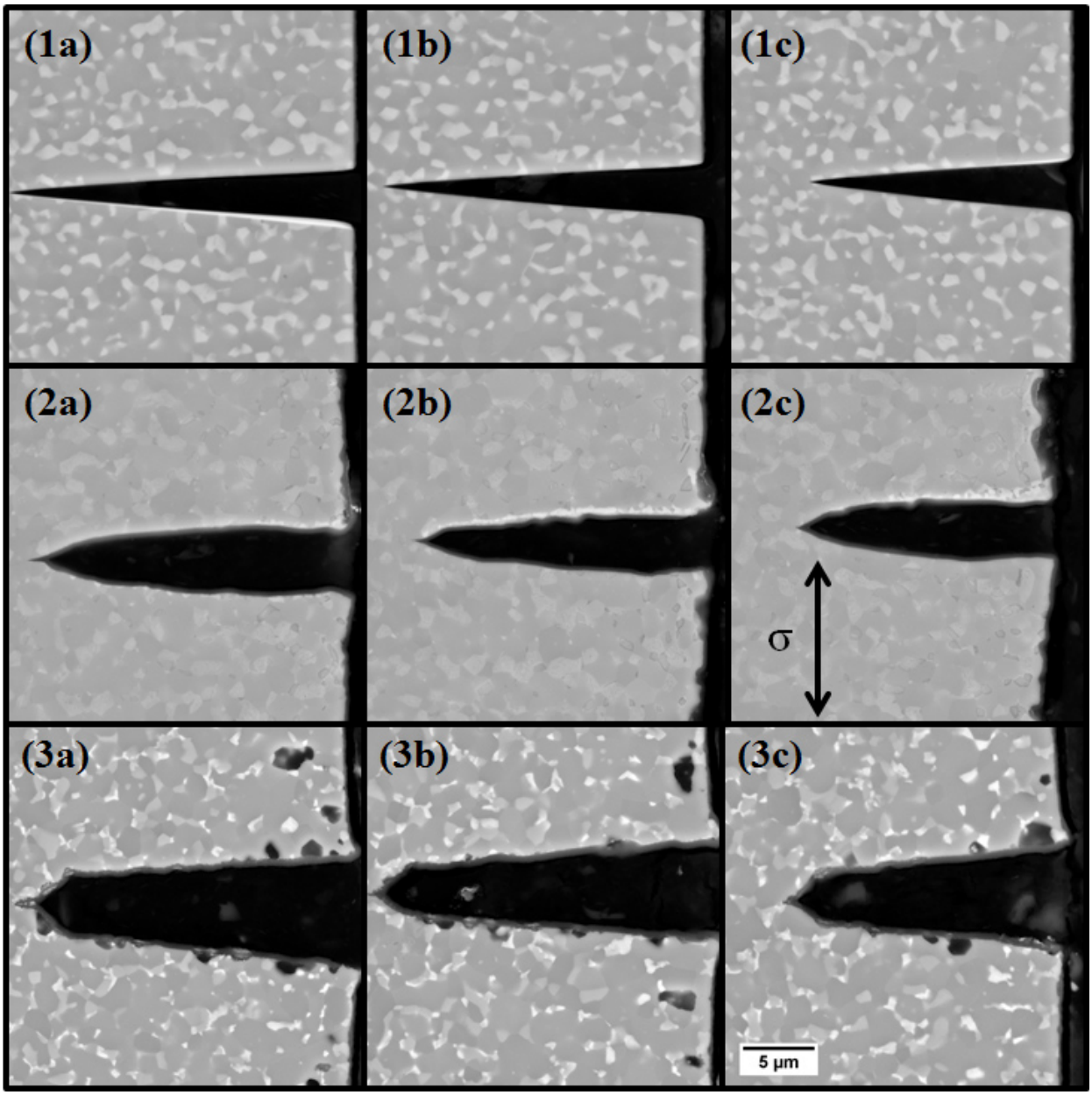

Figure 4.30 - SEM images (low magnification) showing the three notches on the untested coupon (1), and those having undergone cyclic creep (10-50 MPa) at 800°C in a carburizing environment (He-CO/CO_2=1320) and subjected to 198h/3.5% strain (2) and 594h/6.4% strain (3). Note the penetration of the oxide at the notch root in (2) and the effect of microstructure in the neighborhood of the tip oxidation as seen in (3).

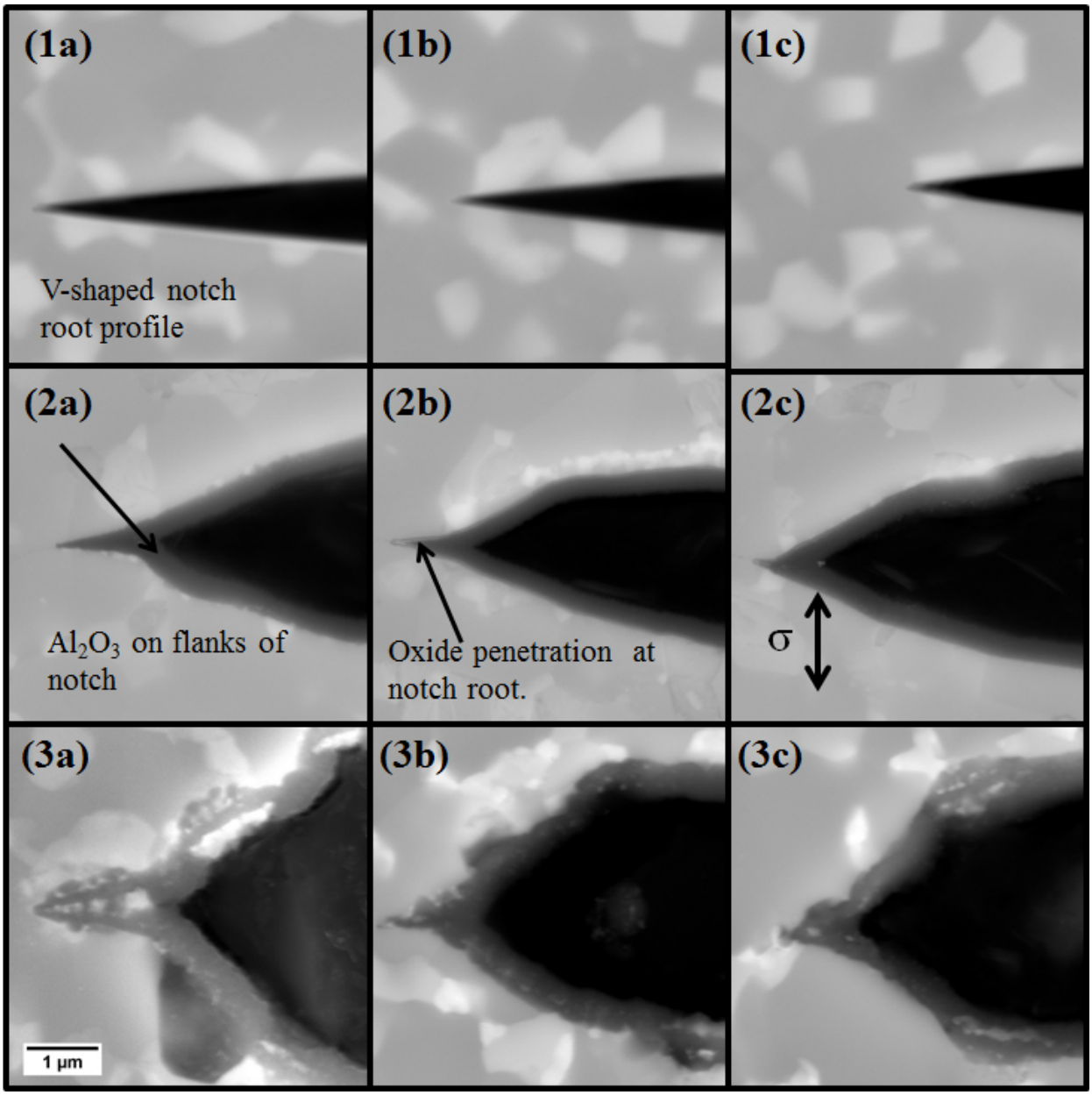

Figure 4.31 - SEM images (high magnification) showing the three notches on the untested coupon (1), and those having undergone cyclic creep (10-50 MPa) at 800°C in a carburizing environment (He-CO/CO_2=1320) and subjected to 198h/3.5% strain (2) and 594h/6.4% strain (3). Note the penetration of the oxide at the notch root in (2) and the effect of microstructure in the neighborhood of the tip oxidation as seen in (3).

4.5. Effect of α-Cr precipitates in the mechanical integrity of clad-aluminized 617.

In section 4.4 above, it was observed that during cyclic creep at low stress/strain of FeCrAlY/NiAl/617, small cracks were formed at the precipitate-rich region of the NiAl layer. One of the reasons advanced to explain the development of these cracks was the presence of precipitates in the NiAl layer. As shown earlier in the project[14], further heat treatment of the

[14] C. G. Levi, J. W. Jones, E. A. Clark, and A. O. Okello, "NEUP 10-963 Quarterly Progress Report Y4Q2," 2014.

FeCrAlY/NiAl/617 system at 1000°C/24h (as-clad systems in this project had been subjected to 1000°C/4h during the coating process) revealed significant dissolution of the NiAl precipitates Figure 4.32. An investigation is currently underway to study the effect of this extended heat treatment on the mechanical behavior of the FeCrAlY/NiAl/617 during cyclic creep in a carburizing/oxidizing environment. This study is expected to help develop an understanding on whether the presence or absence of precipitates in the NiAl layer could explain the observed cracks during creep.

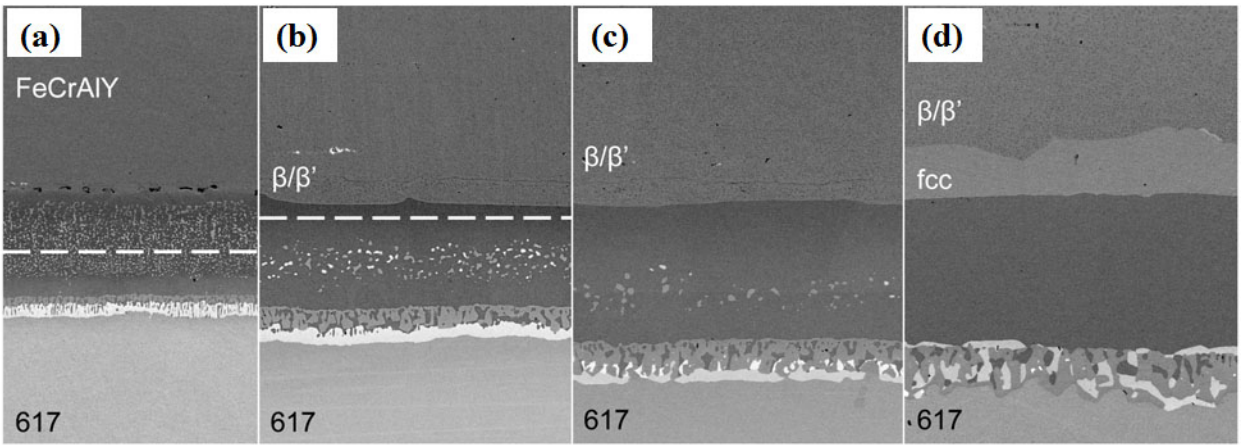

Figure 4.32 - SEM images of Gen II clad + aluminized 617 (a) as clad and after 1000°C heat treatment for (b) 24h, (c) 100h and (d) 500h. The dashed lines in (a,b,c,d) indicate the approximate boundary between Al-rich NiAl and Ni-rich NiAl. The heat treatment of interest for dissolving the precipitates is ~24h.[13]

Task 5. Overall Assessment of Research Findings and Feedback

This project has achieved all its initial objectives, namely the demonstration that robust barrier layer solutions can be applied to alloy 617 to minimize the deleterious effects of impure He exposure, with and without applied load. The salient findings were described at the start of this report. The research highlighted some interesting fundamental issues that merit further investigation under future programs. A critical one is the absence of cracks in the NiAl layer during creep of aluminized-only specimens, but the evolution of periodic cracks when cladding is applied, even though the cracks do not seem to initiate in the cladding or propagate through it.

A second issue that opens opportunities for further development is the successful performance of the carbide+sigma interdiffusion barrier between the NiAl layer and the 617 substrate, albeit with limited durability. Gen III specimens with various sigma stabilizers were prepared and creep specimens were fabricated with one formulation based on added Mo. Preliminary results supported the potential of this concept to stabilize the diffusion barrier, but the optimal conditions were not identified during this project.

Because of the extremely long durability requirements for a system that is thermochemically driven to interdiffusion it is important to elucidate the conditions needed to implement a stable diffusion barrier. This provides motivation for future work in this area.

Publications

Since this project just ended, several manuscripts are still in preparation. These include at least two more manuscripts from E.A. Clark's dissertation, and two from A. Okello's dissertation, also in progress. To date a manuscript and a thesis have been published. These are listed below:

1. E. A. Clark, J. Y. Yang, D. Kumar, G. S. Was, and C. G. Levi, "Engineered Coatings for Ni Alloys in High Temperature Reactors," *Metallurgical and Materials Transactions,* **43** [2] 835-847 (2013).
2. E. A. Clark, "Surface Engineering of Nickel Alloys to Form a Stable Alpha Alumina Barrier Layer at Temperatures Less Than or Equal to 1000 Degrees Celsius," Doctoral Dissertation in Materials, University of California, Santa Barbara, CA (2013).
3. A. Okello, G.S. Was, and J.W. Jones, "Effect of impure helium environments on the extent and mechanism of surface damage of Alloy 617 during creep at 800°C." (In preparation).
4. A. Okello, E.A. Clark, C.G. Levi, and J.W. Jones, "Investigation of efficacy of α-Al_2O_3-forming barrier layers (β-NiAl and FeCrAlY) during creep of Alloy 617 at 800°C." (In preparation).
5. E.A. Clark, J.Y. Yang, T.M. Pollock, C.G. Levi, "Tailoring the Aluminizing Process to Enhance the Stability of Diffusion Coatings on Alloy 617." (In preparation).
6. E.A. Clark, J.Y. Yang, T.M. Pollock, C.G. Levi, "Diffusional stability and environmental resistance of Alloy 617 with different coating architectures." (In preparation).

Oral Presentations[15]

1. "Formation of a Stable α-Al_2O_3 Barrier Layer on Surface-Modified 617 at Low pO_2," Clark, E.A., J. J. Yang, C. G. Levi, Materials Science and Technology 2010 Conference, Houston TX, 18 October 2010.
2. "A Multi-Layer Approach to a Stable Alpha Alumina Barrier Layer on Alloy 617," Clark, E.A., J. J. Yang, G. Gulsoy, D. Kumar, G. S. Was, C. G. Levi, TMS Annual Meeting, San Diego, CA, 1 March 2011.
3. "High Temperature Coatings Research at UCSB: An Overview," Joint UCSB/CMMS-Grenoble/CEMAM Workshop on Architectured Multifunctional Materials and Structures, Autrans, France, June 18, 2012.
4. "A Multi-Layer Approach to a Stable Alpha Alumina Barrier Layer on Alloy 617," Clark, E.A., J. J. Yang, G. Gulsoy, D. Kumar, G. S. Was, C. G. Levi, Idaho National Laboratory, Idaho Falls, ID, 28 November 2012.
5. "Thermal and Environmental Protection of Structural Components for Aerospace and Power Generation," an invited short course organized by the Surface Engineering Group, Department of Mechanical Engineering, Federal University of Paraná, Curitiba, Brazil, November 7, 2013.

[15] In addition, there were several poster presentations at different venues.